An Investigation of the Conditions Leading to Strip Adhesion in Industrial Steel Coils

By

Lulama Velile Wakaba

This thesis is submitted in accordance with the requirements for the degree

Magister Scientiae

In the Faculty of Natural and Agricultural Sciences

Department of Physics

at the

University of the Free State

Bloemfontein

Study leader: Dr M.F. Maritz

Co-study leader: Prof. H. C. Swart

Co-study leader: Dr C.J. Greyling

Submitted: 2 August 2001

Summary

During the production of steel strip, a significant amount of work hardening takes place when the steel is rolled into thin strips, which are stored in a coiled form. These steel coils are batch annealed in order to reduce the hardness and restore formability, before further processing takes place. The development of diffusion welds between spirals of steel coils, during batch annealing, is of particular interest because it prevents the coils from being unwound for further use. This problem is often referred to as strip adhesion or stickering.

In order for strip adhesion to develop, it is essential for some coil spirals to be in contact, while the inter-diffusion between spirals takes place. Furthermore, high temperatures also aid in the diffusion process. It is therefore useful to study the temperature and resulting thermal stress distributions in the coil, during batch annealing. The temperature distribution allows for the calculation of thermal stress, which is the driving force for establishing contact between spirals, and in addition to this, the temperature distribution also provides some clues regarding the likelihood of inter-diffusion.

In this study, models of temperature and stress are presented. A two-dimensional finite difference model for temperature is presented and confirmed by an analytical solution of the same problem. Analysis of a three-dimensional temperature model in the third chapter shows that, as far as heat transfer is concerned, a cylindrical coil can be well approximated by a solid cylinder with a concentric hole. All the temperature modeling was done for the interior of a coil. Further discussion in later chapters shows that a cylindrical coil can also be treated as a solid cylinder for thermal stress modeling.

A long cylinder stress model in the fifth chapter provides some useful insight, as far as strip adhesion is concerned, even though it is a one-dimensional model that does not consider the effect of axial heat transfer. The radial compressive stress during the cooling stage of the batch annealing process was identified as a paramount ingredient to strip adhesion.

The thermal stress calculations are later extended to include a linear cooling temperature ramp and these results are arguably the most important findings of this study. According to these results, when the a cylinder is cooled in such a way that the outer edge lags behind the cooling of the inner edge, by a few hours, the compressive radial stress is greatly reduced. Consequently, the contact pressure between spirals at the most critical stage of batch annealing (where strip adhesion occurs) is decreased and the chance of strip adhesion developing is reduced.

Acknowledgements

I would hereby like to extend my appreciation to the following:

- Dr M.F. Maritz for his invaluable expertise and assistance.
- Prof. H.C. Swart for his insight and guidance.
- Dr C.J. Greyling for his wealth of information and support.
- The University of the Free State and its staff for providing an academically nurturing environment.

TABLE OF CONTENTS

Chapter 1

Introduction

1.1 Background

During the production of steel strip, a significant amount of work hardening takes place when the steel is rolled into thin strips, which are stored in a coiled form. These steel coils are batch annealed in order to reduce the hardness and restore formability, before further processing takes place. The development of diffusion welds between spirals of steel coils, during batch annealing, is of particular interest because it prevents the coils from being unwound for further use. This problem is often referred to as strip adhesion or stickering.

Most of the work done in this field deals with aspects related to heat transfer. Perrin and Johnson [1] discuss how the overall design of annealing systems impacts some aspects of aerodynamics and heat transfer of the circulating gases during, batch annealing. The thermal and physical properties of stacks of cold-rolled steel are investigated by Lisogor and Mitkalinnyi [2]. Some computer modeling and experimental results regarding the prediction of heating, soaking and cooling times in batch annealing, are presented by Rao, Barth and Miller [3]. Rovito [4] also provides a computer-based model for predicting the annealing time.

Leroy and Bouquegneau [5] discuss the possibilities and limits of batch annealing with 100% hydrogen. This reference also contains sections dealing with the gas-metal reactions and the development of radial thermal stress that take place throughout the annealing process. A more in-depth study of the gas-metal reactions can be obtained from a United States Patent by Zylla [6], which introduces a process for preventing the formation of adhesives when annealing steel coils (this is also known as the Defox Plus process).

1.2 Batch Annealing Process

In a typical batch annealing process, several coils are annealed in a bell-shaped furnace (as shown in figure 1.1) and a reducing gas, i.e. hydrogen or a nitrogen/hydrogen mixture, is passed through the coils, in a circular fashion, to prevent oxidation [6]. The heat is supplied from outside the inner cover by means of a heater that fits over the system. The reducing gas circulates in the manner shown by the arrows in figure 1.1 (the dotted lines on each coil represent the inner ring). When the gas leaves the circulating fan, it moves along the heated walls of the inner cover and thereby receives heat. In the ensuing period, the gas then moves down through the coil center and interior, thus heating the coil from interior as well. The convector plates enhance gas circulation though the coils.

During the batch annealing process, heating occurs in the form of a temperature ramp, which increases to a maximum temperature of about 670°C before decreasing to room temperature. According to experimental findings, strip-adhesion usually takes place at the critical time interval shown on the temperature ramp in figure 1.2 [5]. The critical time interval is characterized by a steep decreasing thermal gradient and high thermal stresses.

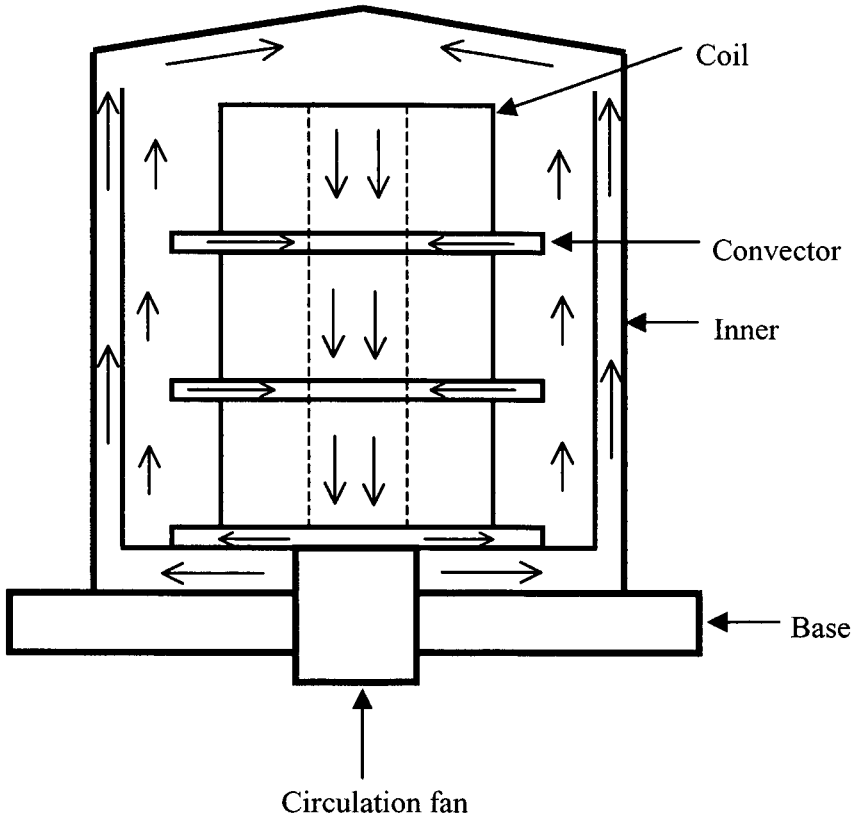

Figure 1.1: An illustration of the batch annealing process.

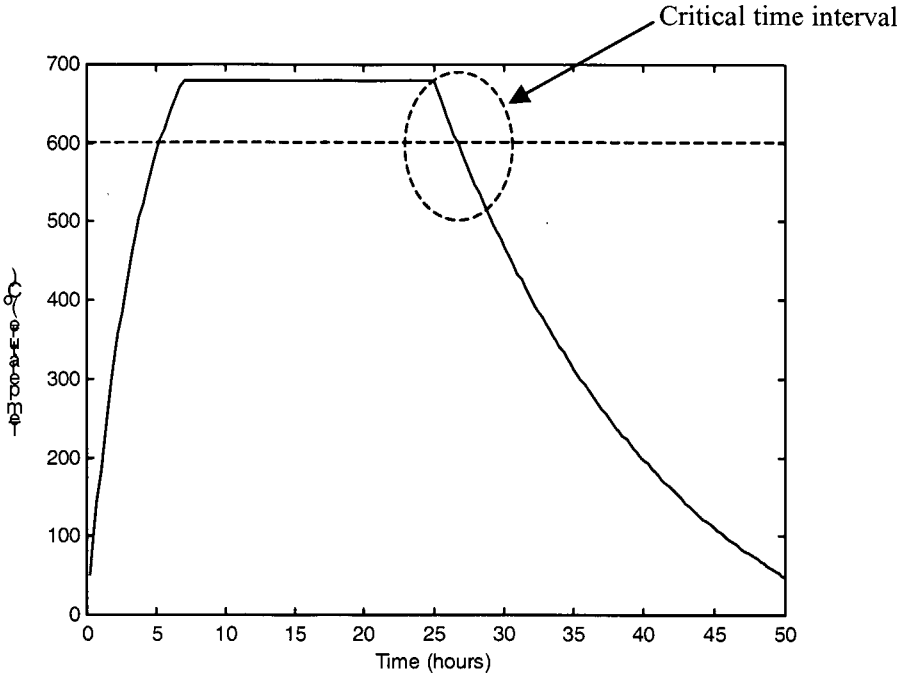

Figure 1.2: A typical temperature ramp with an indicated critical time interval. The dotted line at 600°C has relevance to the Defox Plus process that is discussed in section 1.3.

1.3 Defox Plus Process

The Defox Plus process, which was developed by Peter Zylla [6], claims to prevent strip adhesion by circulating a gas mixture, during batch annealing, that oxidizes the coil spirals at temperatures above 600°C in the heating phase and reduces them below 600°C, in the cooling phase. This process was designed in such a way that an oxide layer is present on the spirals during the critical time interval, in order to discourage adhesion. After undergoing reduction, the coils emerge as desired. This process can be understood largely by studying the gas-metal reactions that take place during the oxidation and reduction stages.

In order for the Defox Plus process to be effective, it is necessary for the desired gases to circulate between the spirals, thus allowing oxidation and reduction occur at the desired

times in the temperature cycle. Compressive radial thermal stresses, resulting temperature gradients within the coils, can cause successive spirals to establish contact, thereby constricting the flow of gas and hindering particularly the reduction processes, in the critical time interval. If the coils were annealed in an oxidation-preventative gas atmosphere (i.e. an inert gas), radial compressive stresses would increase the chance of adhesion between spirals. It is therefore necessary to know the relevant thermal stress distributions for the annealing process. Furthermore, the thermal stress distributions can only be calculated once the temperature distribution is known.

1.4 Objectives of this study

This study was undertaken with three goals in mind. The *first* objective was to provide models of temperature and thermal stress that would shed more light on the conditions experienced by industrial steel coils during batch annealing. The *second* aim was to use the knowledge gained from the temperature and thermal stress models to formulate a suggestion that would reduce the likelihood of strip adhesion developing. The *third*, final and most important objective has been to expose the author to numerical and analytical techniques in a research environment. For this reason, no automatic software packages were used to solve equations.

With regards to the modeling of temperature, it should be noted that various models of batch annealing already exist. Some provide predictions of annealing times [4], whilst others consider such factors as: the gas flow rate, the thermal conductivity of the circulating gas, the effect of radiation (from the inner cover) and convection on the eventual temperature distributions in each coil [3]. The entire temperature topic, in this study, will focus on heat transfer modeling within a coil, based on supplied external boundary conditions.

1.5 Scope of thesis

A numerical solution to a solid cylinder (a solid cylinder with a concentric hole) model for heat transfer is developed in *Chapter 2*, as a first approximation to a cylindrical coil. This is subsequently followed by an analytical solution and comparison that confirms the numerical result. In *Chapter 3*, a numerical model for a three-dimensional coil is formulated and a theta-dependence test is performed, for the purpose of establishing the difference between heat transfer in a cylindrical coil and a solid cylinder. This has bearing on the computational speed at which temperature can be modeled in a cylindrical coil. Stability conditions for the numerical solutions are also derived.

Certain aspects of the general theory of elasticity are introduced in *Chapter 4*. Some fundamental concepts are treated in this chapter, and it forms a basis for the one-dimensional thermal stress model for a solid cylinder in *Chapter 5*. This is followed by a short discussion regarding temperature and stress environments that encourage and discourage the adhesion of spirals. Appearing in this chapter, as well, is a proposed reason for strip adhesion occuring during cooling and a suggestion that reduces the compressive radial stresses in the critical time interval. A final conclusion is made in *Chapter 6*.

Chapter 2

Temperature Model for a Solid Cylinder

2.1 Introduction

In this chapter, the heat equation for axial symmetry is solved both analytically and numerically, with the intention of using the analytical solution to verify the numerical solution. The first section of this chapter begins with a description of how heat transfer in a solid cylinder (with a concentric hole) is treated. This is followed by a segment that deals with the relevant initial and boundary conditions.

Section 2.4 shows how the finite difference method can be applied to the heat equation. A derivation of the numerical stability conditions follows thereafter, just before the results are displayed. Included in the results, is a short discussion of the cold region that develops during heating. The analytical solution is derived in section 2.8 and the corresponding results are displayed in section 2.9. A comparison between numerical and analytical solutions is subsequently performed.

2.2 Solid Cylinder Model

The study of heat transfer in a solid cylinder can be considered as an approximation to heat transfer in a cylindrical coil. It is important to note that such an approximation depends on the assumption that there is no heat flow along the spirals of the coil (see figure 2.1). This assumption can also be re-stated by saying that the heat flow in the coil has no θ-dependence.

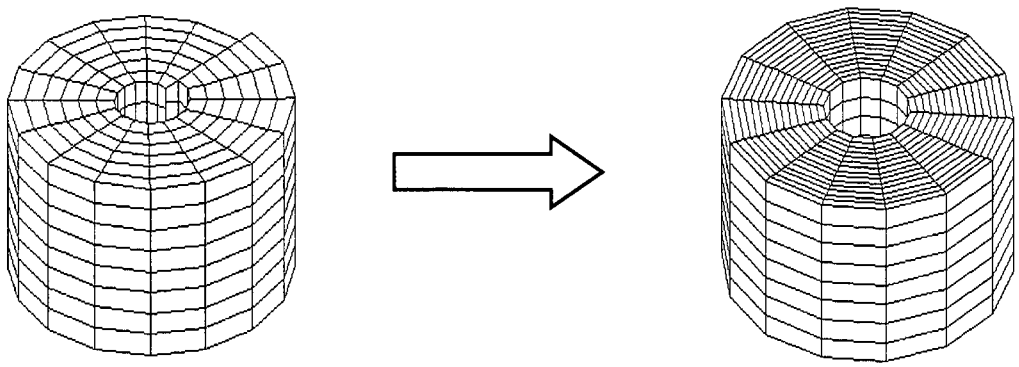

(a) (b)

Figure 2.1: (a) Cylindrical coil. (b) Solid cylinder with a concentric hole and different thermal diffusivity values in the radial and axial directions.

A solid cylinder model has to account for the different thermal coefficients k_z (in the z-direction of the material) and k_r (in the radial direction). Since a steel coil, that undergoes batch annealing, has a film of gas and oil between each spiral, it can be expected that k_r and k_z will be different [3].

In order to model the evolution of temperature in the steel coil during the batch annealing process, use will be made of the well-known heat equation [7]. In cartesian coordinates, the heat equation is,

$$\kappa_x \frac{\partial^2 T}{\partial x^2} + \kappa_y \frac{\partial^2 T}{\partial y^2} + \kappa_z \frac{\partial^2 T}{\partial z^2} = \frac{\partial T}{\partial t}, \qquad (2.1)$$

where T is the temperature, t is time and

$$\kappa_x = \frac{k_x}{\rho C_p},$$

$$\kappa_y = \frac{k_y}{\rho C_p},$$

and

$$\kappa_z = \frac{k_z}{\rho C_p}.$$

Note that κ_x, κ_y and κ_z are referred to as the thermal diffusivity values for the x, y and z directions. The density of the material is represented by ρ, C_p is the specific heat under constant pressure and k is the thermal conductivity.

For the purpose of the solid cylinder problem, it is more useful to transform (2.1) into cylindrical coordinates. In cylindrical coordinates, the following is obtained:

$$\kappa_r \frac{1}{r}\frac{\partial T}{\partial r} + \kappa_r \frac{\partial^2 T}{\partial r^2} + \kappa_\theta \frac{1}{r^2}\frac{\partial^2 T}{\partial \theta^2} + \kappa_z \frac{\partial^2 T}{\partial z^2} = \frac{\partial T}{\partial t} \tag{2.2}$$

where

$$\kappa_r = \frac{k_r}{\rho C_p},$$

$$\kappa_\theta = \frac{k_\theta}{\rho C_p}, \tag{2.3}$$

and

$$\kappa_z = \frac{k_z}{\rho C_p}.$$

But since axial-symmetry about the z-axis is assumed, θ-dependence may be eliminated from (2.2) such that:

$$\kappa_r \frac{1}{r}\frac{\partial T}{\partial r} + \kappa_r \frac{\partial^2 T}{\partial r^2} + \kappa_z \frac{\partial^2 T}{\partial z^2} = \frac{\partial T}{\partial t}. \tag{2.4}$$

Since the solid cylinder is axially-symmetric, the temperature distribution of the whole cylinder will be known if the temperature distribution over cross section A is known (see figure 2.2). This reduces the 3-D problem to a 2-D problem

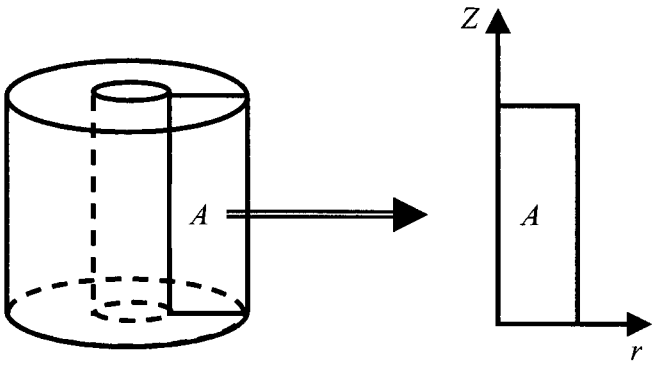

Figure 2.2: A diagram of an axially symmetric solid cylinder that has a temperature distribution which is fully described by cross section A.

2.3 Initial and Boundary Conditions

As a first approximation, assume that the batch annealing process occurs at a constant temperature of 670°C. Now, in order to test whether this model can predict the existance of a cold spot, the temperature 670°C will be applied on all external surfaces of the cylinder and the time evolution of the temperature will be calculated. Note that the initial temperature of the interior is at room temperature, which will be taken here as 23°C. The boundary condition will be taken as constant and equal to 670°C for any time greater than zero.

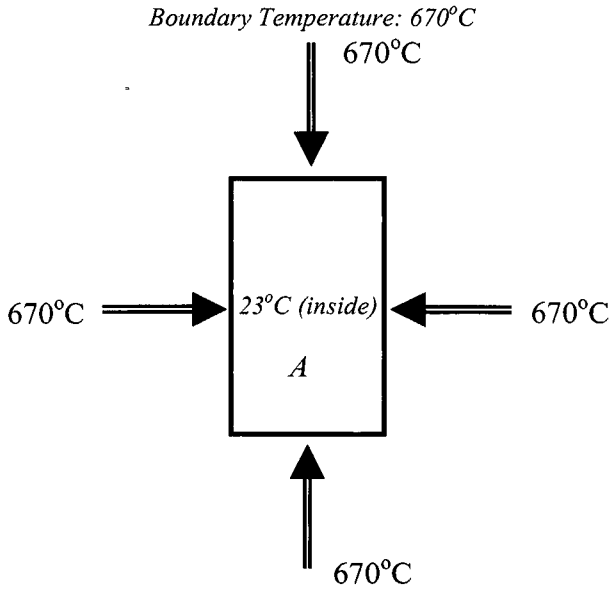

Figure 2.3: Initial and boundary conditions of solid cylinder.

The finite difference method will be used to solve equation (2.4) for the above mentioned initial conditions. An introduction of the finite difference method can be seen in appendix A.

2.4 Finite Differences Applied to the Solid Cylinder

The heat equation (2.4) needs to be solved for surface A (see figure 2.3). In order to use the finite difference technique, surface A needs to be discretized into a matrix of points. The step-length and index for the r-direction is h_r and i, respectively. For the z-direction, h_z is the step-length and j is the index. The index for time is n, while τ represents the corresponding step-length. A temperature $T^n_{i,j}$ is therefore associated with each point (i,j) at some time τn. Since $ih_r = r, jh_z = z$ and $n\tau = t$, it follows that $T^n_{i,j}$ is an approximation of $T(ih,jk,n\tau)$.

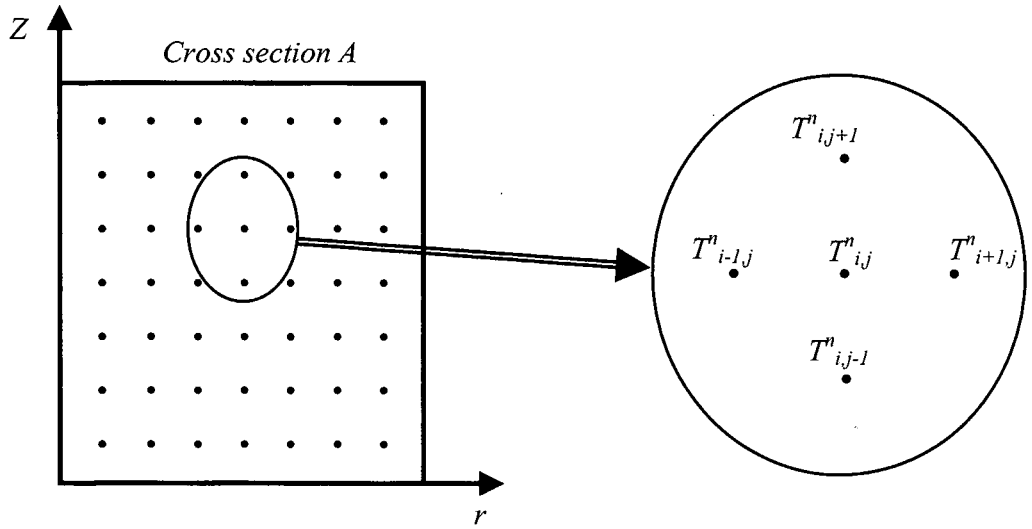

Figure 2.4: A diagram of cross section A, after discretization.

When dealing with a function of two or more independent variables, the partial derivatives are approximated by partial differences. Therefore, by using partial differences, the following approximations can be made:

$$\frac{\partial^2 T}{\partial r^2} \approx \left(\frac{T^n{}_{i+1,j} - 2T^n{}_{i,j} + T^n{}_{i-1,j}}{h_r{}^2} \right), \tag{2.5}$$

$$\frac{\partial^2 T}{\partial z^2} \approx \left(\frac{T^n{}_{i,j+1} - 2T^n{}_{i,j} + T^n{}_{i,j-1}}{h_z{}^2} \right), \tag{2.6}$$

$$\frac{\partial T}{\partial r} \approx \left(\frac{T^n{}_{i+1,j} - T^n{}_{i-1,j}}{2h_r} \right), \tag{2.7}$$

$$\frac{\partial T}{\partial t} \approx \left(\frac{T^{n+1}{}_{i,j} - T^n{}_{i,j}}{\tau} \right). \tag{2.8}$$

By substituting (2.5), (2.6), (2.7) and (2.8) into the heat equation (2.4), the following is obtained:

$$T^{n+1}{}_{i,j} = T^{n}{}_{i,j} + \tau\left[\kappa_r \frac{1}{r_i}\left(\frac{T^{n}{}_{i+1,j} - T^{n}{}_{i-1,j}}{2h_r}\right) + \kappa_r\left(\frac{T^{n}{}_{i+1,j} - 2T^{n}{}_{i,j} + T^{n}{}_{i-1,j}}{h_r{}^2}\right)\right.$$

$$\left. + \kappa_z\left(\frac{T^{n}{}_{i,j+1} - 2T^{n}{}_{i,j} + T^{n}{}_{i,j-1}}{h_z{}^2}\right)\right] \tag{2.9}$$

According to the initial conditions, all the points on the boundary are at 670°C, while all the interior points are at room temperature (23°C). As discussed previously, the initial temperature distribution over surface A has a matrix of the form:

$$T = \begin{bmatrix} 670 & 670 & 670 & 670 & 670 \\ 670 & 23 & 23 & 23 & 670 \\ 670 & 23 & 23 & 23 & 670 \\ 670 & 23 & 23 & 23 & 670 \\ 670 & 670 & 670 & 670 & 670 \end{bmatrix}.$$

Equation (2.9) is applied to the interior matrix elements, while the boundaries remain at 670°C. The calculation begins at $n = 1$, $i = 2$ and $j = 2$. All the interior matrix elements are updated with each iteration. In other words, $T^{n}{}_{i,j}$ is updated for each value of n, as time progresses. The stability conditions for this numerical scheme is investigated below.

2.5 Stability Conditions

The numerical scheme (2.9) is consistent with (2.4) meaning that as h_r, h_z and τ tend to zero, each of the difference replacements tend to the corresponding derivatives. However, this is not enough to ensure that a solution of (2.9) is a good approximation to a solution of (2.4), for the same initial and boundary conditions. An extra condition, the so-called "von Neumann stability condition" needs to be satisfied [8]. This is a condition that imposes a relationship between the magnitude of the time and space step sizes.

In order to derive the stability condition of (2.9), it will be assumed that r_i is kept constant on r_{min}. This will necessarily mean that the coefficient

$$\frac{\kappa_r}{r_i},$$

which is positioned in front of the term

$$\left(\frac{T^n{}_{i+1,j} - T^n{}_{i-1,j}}{2h_r}\right)$$

maintains its largest value. With this assumption, (2.9) is a linear difference equation and will admit solutions of the type:

$$T^n{}_{i,j} = \xi^n e^{\bar{i}(i\omega_r + j\omega_z)}. \qquad (2.10)$$

A solution of the type (2.10) is called a mode. Von Neumann stability implies that τ, h_r, and h_z have such a relationship that no single mode will grow exponentially. Otherwise stated,

$$|\xi| \leq 1$$

or

$$|\xi|^2 \leq 1. \qquad (2.11)$$

Substitution of (2.10) into (2.9) gives:

$$\xi^{n+1}e^{\bar{i}(i\omega_r+j\omega_z)} = \xi^n e^{\bar{i}(i\omega_r+j\omega_z)} + \tau\left[\frac{\kappa_r}{2h_r r_{\min}}e^{\bar{i}(i\omega_r+j\omega_z)}(e^{\bar{i}\omega_r} - e^{-\bar{i}\omega_z}) + \right.$$

$$+\frac{\kappa_r\xi^n e^{\bar{i}(i\omega_r+j\omega_z)}}{h_r^{\,2}}(e^{\bar{i}\omega_r} - 2 + e^{-\bar{i}\omega_z}) \qquad (2.12)$$

$$\left.+\frac{\kappa_z\xi^n e^{\bar{i}(i\omega_r+j\omega_z)}}{h_z^{\,2}}(e^{\bar{i}\omega_z} - 2 + e^{-\bar{i}\omega_z})\right]$$

After some simplification, (2.12) can be written as,

$$\xi = 1 + \tau\left[\frac{\kappa_r}{2hr_{\min}}\left(e^{\bar{i}\omega_r} - e^{-\bar{i}\omega_z}\right) + \frac{\kappa_r}{h^2}\left(e^{\bar{i}\omega_r} - 2 + e^{-\bar{i}\omega_z}\right) + \frac{\kappa_z}{k^2}\left(e^{\bar{i}\omega_z} - 2 + e^{-\bar{i}\omega_z}\right)\right] \qquad (2.13)$$

If identities

$$\sin(\omega) = \frac{e^{\bar{i}\omega} - e^{-\bar{i}\omega}}{2\bar{i}} \qquad (2.14)$$

and

$$\cos(\omega) = \frac{e^{\bar{i}\omega} + e^{-\bar{i}\omega}}{2} \qquad (2.15)$$

are used, equation (2.13) can be expressed as:

$$\xi = 1 + \tau\left[\frac{\kappa_r\bar{i}}{hr_{\min}}\sin(\omega_r) + \frac{2\kappa_r}{h^2}\left(\cos(\omega_r) - 1\right) + \frac{2\kappa_z}{k^2}\left(\cos(\omega_z) - 1\right)\right]. \qquad (2.16)$$

It thus follows from the stability condition and equation (2.16) that

$$|\xi|^2 \le \left[1 + 2\tau\left(-\frac{2\kappa_r}{h^2} - \frac{2\kappa_z}{k^2}\right)\right]^2 + \left[\frac{\tau\kappa_r}{hr_{\min}}\right]^2 = \left[1 + 4\tau A\right]^2 + \left[\tau B\right]^2 \le 1 \qquad (2.17)$$

where

$$A = \left(-\frac{\kappa_r}{h^2} - \frac{\kappa_z}{k^2} \right) \tag{2.18}$$

and

$$B = \frac{\kappa_r}{h r_{\min}} \tag{2.19}$$

According to (2.17),

$$1 + 8\tau A + 16A^2\tau^2 + \tau^2 B^2 \le 1,$$

and

$$\tau\left(B^2 + 16A^2\right) + 8A \le 0.$$

This implies that scheme (2.9) is stable if

$$\tau \le \frac{-8A}{\left(B^2 + 16A^2\right)}. \tag{2.20}$$

Equation (2.20) shows that the stability condition also depends on κ_r and κ_z. These values, in general, depend on temperature. Some temperature dependence curves follow hereafter.

2.6 Temperature Dependence of the Radial and Axial Thermal Diffusivity

A publication by Rao, Barth and Miller [3] shows some tabulated values of the thermal coefficients k_r, k_z and the specific heat C_p as a function of temperature. Graphical plots of these values can be seen in figures 2.5*a*, 2.5*b* and 2.5*c*. The calculated values for κ_r and κ_z are plotted in figures 2.5*d* and 2.5*e*. These values were calculated using equation (2.3) in conjunction with the above-mentioned data. A constant density of $\rho = 7860$ kg.m^{-3} was used.

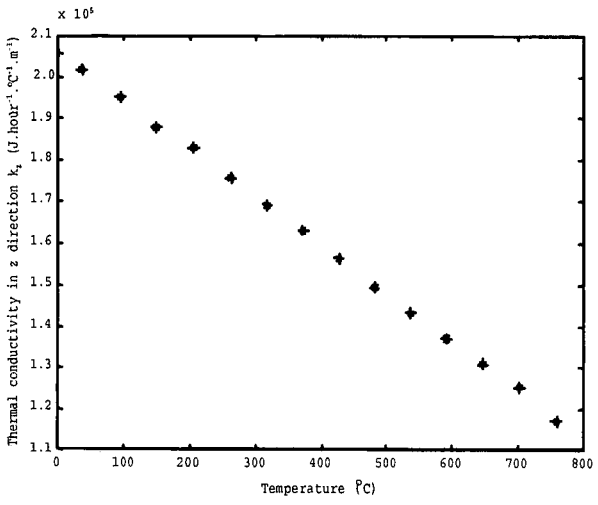

(a)

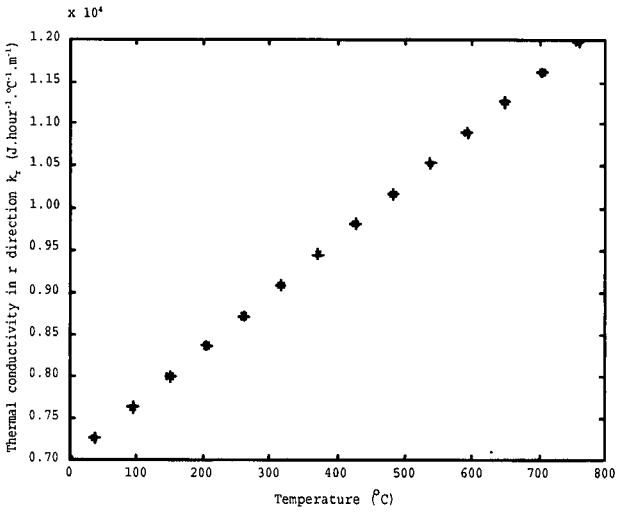

(b)

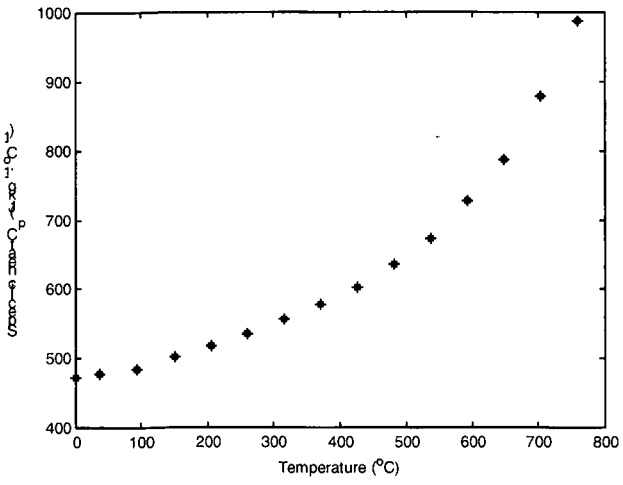

(c)

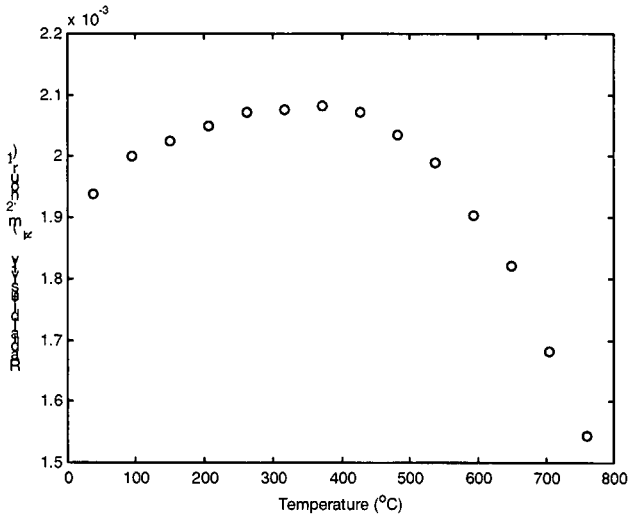

(d)

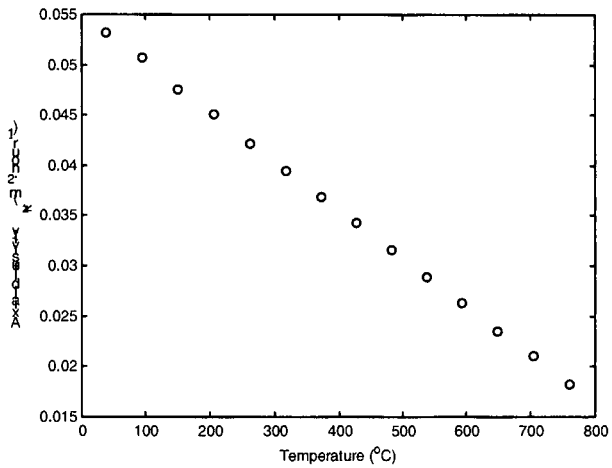

(e)

Figure 2.5: (a) Axial thermal conductivity as a function of temperature. (b) Radial thermal conductivity versus temperature. (c) Specific heat against temperature. (d) Radial thermal diffusivity as a function of temperature. (e) Axial thermal diffusivity versus temperature.

2.7 Numerical Results for a Solid Cylinder

A program called *fine2d.m*, that implements equation (2.9) for the initial and boundary conditions of section 2.3, was written in MATLAB (version 4.2c.1). This program is listed in appendix B.5. Mesh diagrams of the results are shown in figure 2.6.

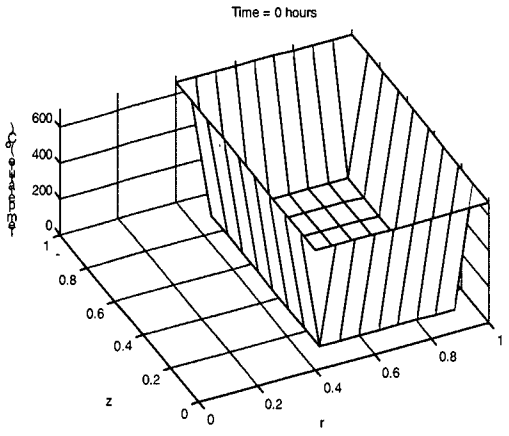

(a)

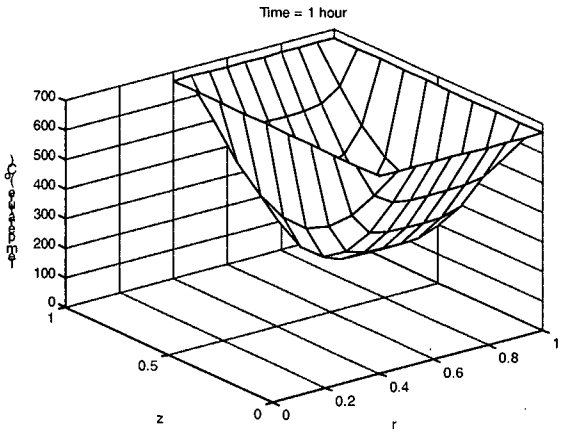

(b)

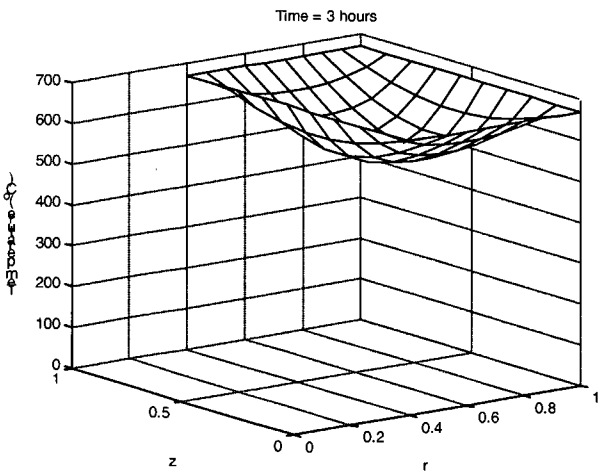

(c)

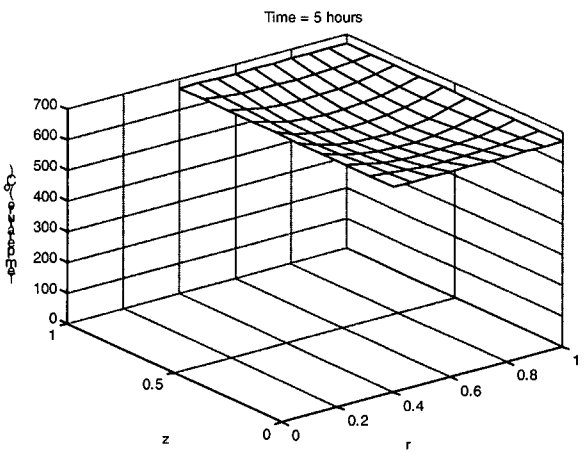

(d)

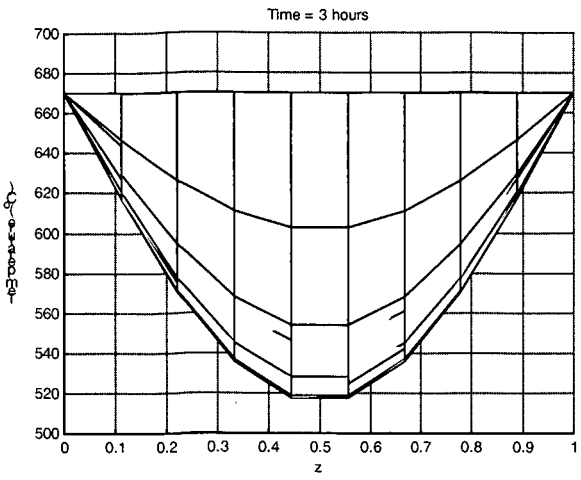

(e)

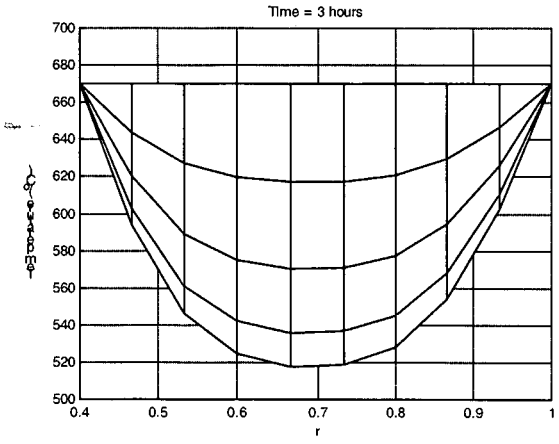

(f)

Figure 2.6: (a) to (d) Temperature profiles for various time intervals. (e) A cross section in the z-direction after 3 hours. (f) A cross section in the r-direction after 3 hours.

It can be seen from figure 2.6 that the temperature distribution in the z-direction is symmetrical, while the r-direction exhibits a slightly anti-symmetrical temperature distribution. The symmetry in the z-direction can be expected, since the cylinder experiences the exact same conditions at the top and bottom. The reason for the lack of symmetry in the r-direction can be explained by the following physical arguments.

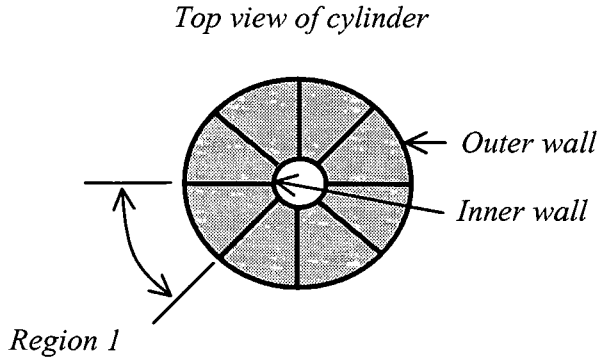

Figure 2.7: Top view of a solid cylinder with imaginary sectors.

If one considers, say 8, equidistant regions on the outside wall of the cylinder and 8 equidistant regions on the inner wall (see figure 2.7): *The amount of heat entering from the inner regions is not the same as the heat entering from the outer regions.*

The heat entering per unit area is the same on both inner and outer regions (both are at 670°C). But, the area of material comprising the inner region is less than that of the outer region, therefore, more heat enters from the outer region. This implies that a cold region, which is closer to the inner wall than the outer wall, will develop. So a temperature curve like the one in figure 2.6f will develop in the radial direction and the cold region will be closer to the inner ring (see figure 2.8).

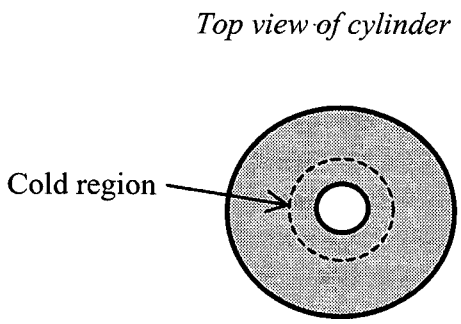

Figure 2.8: Top view of a solid cylinder.

The extent of anti-symmetry is influenced by the dimensions of the coil and the magnitudes of κ_r and κ_z. If κ_z is much larger than κ_r, heat flow in the z-direction dominates and the anti-symmetry of the r-direction becomes less significant. On the other hand, if κ_r is comparable or even larger than κ_z, the effect of anti-symmetry becomes more pronounced. **Note** also that the cold region is closer to the inner ring for a thick coil than for a thin one.

Since the temperature distribution is symmetrical in the z-direction, with the minimum value at the mid-point of the cylinder, it is safe to say that the cold region develops as a ring that is situated in the center of the coil (see figures 2.8 and 2.9).

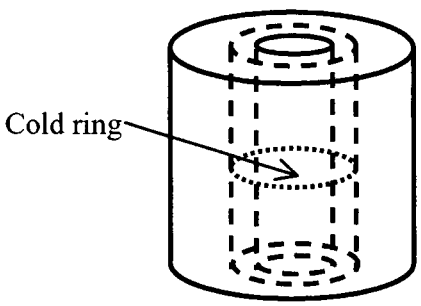

Figure 2.9: An illustration of the position of the cold ring.

The cold ring is at a position of less than a half of the distance from the inner to the outer wall, as shown in figure 2.8. The position of the cold ring also depends on how the cylinder is heated. In a typical batch annealing furnace, the outer wall of a cylindrical coil tends to be hotter than the inner wall during heating and the converse is true during cooling. This would affect the position of the cold ring, particularly in the radial direction.

2.7.1 Temperature ramp

During an annealing cycle, the edges of the coil are directly exposed to a temperature ramp. Therefore, the edges remain at the same temperature as the ramp throughout the heating process. A temperature ramp was applied to the edges of a solid cylinder (this was implemented by the MATLAB program *finramp.m*, in appendix B.7). Figure 2.9 shows the time evolution of the hottest region (the edges) together with the cold region. Note, once again, that the temperature profile of the hottest region is identical to that of the applied temperature ramp.

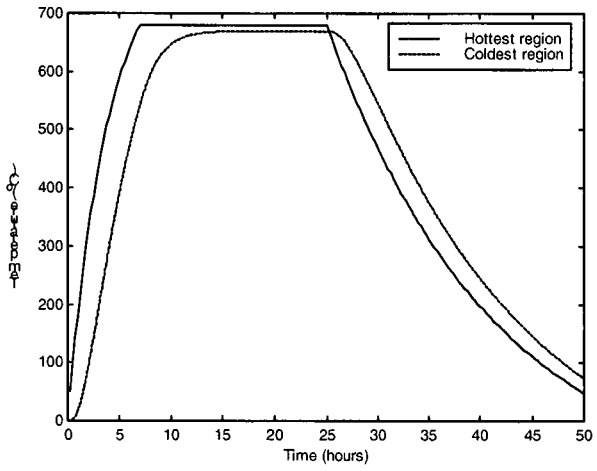

Figure: 2.9: A comparison of the outer region and coldest region during a temperature cycle.

In the next section, an analytical solution will be obtained for a solid cylinder.

2.8 Analytical Solution for Solid Cylinder

This section seeks to obtain an analytical solution to the heat equation for axial symmetry by means of separation of variables. The heat equation for axial symmetry is given by (2.4),

$$\kappa_r \frac{1}{r}\frac{\partial T}{\partial r} + \kappa_r \frac{\partial^2 T}{\partial r^2} + \kappa_z \frac{\partial^2 T}{\partial z^2} = \frac{\partial T}{\partial t}.$$

This equation will be solved on the rectangular domain $B=\{(r,z)|r \in [r_{in},r_{out}],\ z \in [0,H]\}$. Let ∂B be the boundary of this domain, with r_{in} and r_{out} being the inner and outer radii of the coil, respectively. The coil height H is in the z-direction.

Equation (2.4) will be solved subject to the boundary conditions

$$T(t,r,z) = 0, \quad t \geq 0, \quad (r,z) \in \partial B \tag{2.22}$$

and the initial conditions

$$T(0,r,z) = \begin{cases} 0, (r,z) \in \partial B \\ -T_0, (r,z) \in B - \partial B \end{cases} \tag{2.23}$$

This condition assumes a shifting in the temperature so that room temperature is at $-T_0$ and the externally applied temperature (670°C in this case) is 0.

In order to find a solution by means of separation of variables, T will be expressed as the following product:

$$T(0,r,z) = T_0 R(r) Z(z)$$

where

$$R(r) = \begin{cases} 0, & r = r_{in} \\ -1, & r \in (r_{in}, r_{out}), \\ 0, & r = r_{out} \end{cases} \tag{2.24}$$

and

$$Z(z) = \begin{cases} 0, & z = 0 \\ -1, & z \in (0, H) \\ 0, & z = H \end{cases}. \tag{2.25}$$

See figure 2.10, for a graphical illustration of the functions *R(r)* and *Z(z)*.

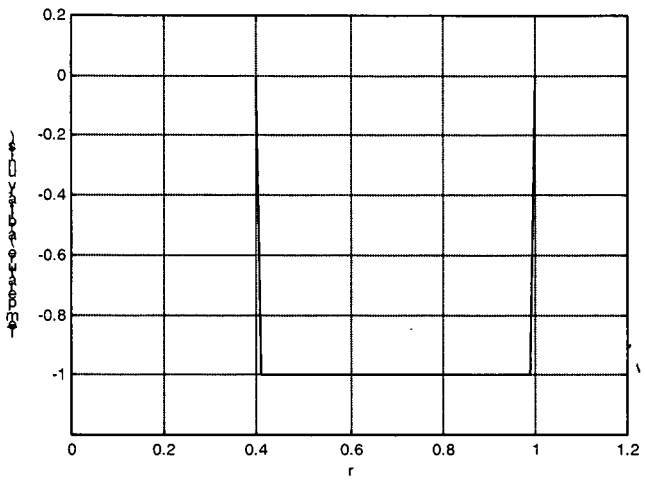

(a)

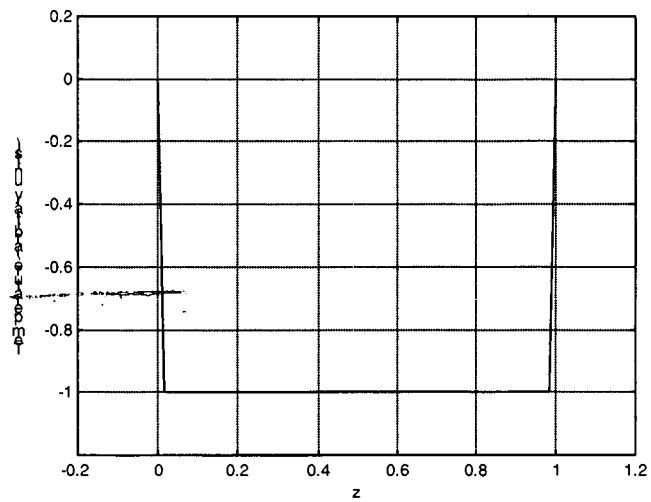

(b)

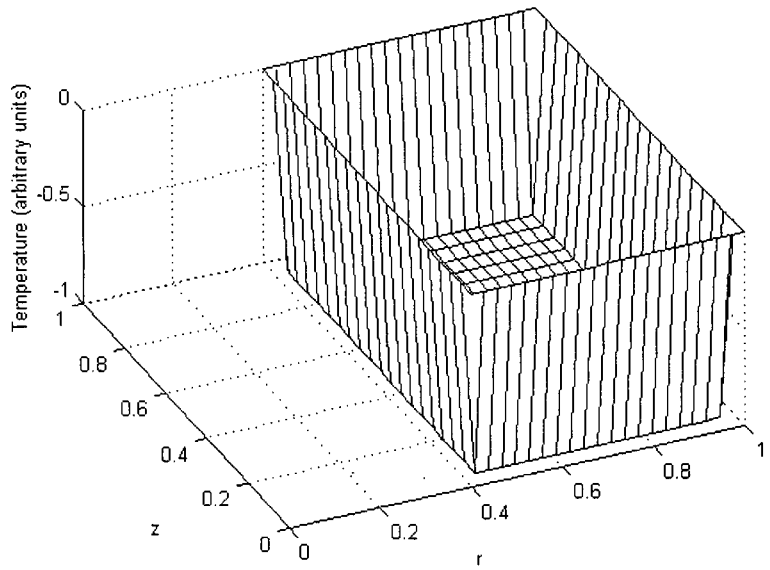

(c)

Figure 2.10: (a) Initial condition (2.24). (b) Initial condition (2.25). (c) Initial condition for T(r,z,t).

Since a solution by separation of variables is desired, the solution can expressed as a product of three functions of single variables,

$$T(t,r,z)=U(t)R(r)Z(z)\ . \tag{2.26}$$

Now, by substituting (2.26) into (2.4), the following expression is obtained:

$$\kappa_r \frac{1}{r}U(t)R'(r)Z(z)+\kappa_r U(t)R''(r)Z(z)+\kappa_z U(t)R(r)Z''(z)=U'(t)R(r)Z(z)\,.$$

When the above expression is divided by $U(t)R(r)Z(z)$, the following is obtained:

$$\kappa_r \frac{1}{r}\frac{R'(r)}{R(r)}+\kappa_r \frac{R''(r)}{R(r)}+\kappa_z \frac{Z''(z)}{Z(z)}=\frac{U'(t)}{U(t)}. \tag{2.27}$$

Let $-\mu$ be the separation constant. It thus follows that

$$\frac{U'(t)}{U(t)} = -\mu \tag{2.28}$$

and

$$\kappa_r \frac{1}{r}\frac{R'(r)}{R(r)} + \kappa_r \frac{R''(r)}{R(r)} = -\mu - \kappa_z \frac{Z''(z)}{Z(z)} = -\lambda^2, \tag{2.29}$$

The left hand side is function of r, while the right hand depends on z. This implies that both sides equal a constant value, say $-\lambda^2$, which is known as the separation constant. Consequently, equation (2.29) yields the following ordinary differential equations,

$$Z''(z) + \omega^2 Z(z) = 0, \tag{2.30}$$

where

$$\omega^2 = \frac{\mu - \lambda^2}{\kappa_z} \tag{2.31}$$

and

$$\kappa_r R'(r) + \kappa_r r^2 R''(r) = -r^2 R(r)\lambda^2 . \tag{2.32}$$

Multiplication by $r^2R(r)$ reduces (2.29) to

$$r^2 R''(r) + rR'(r) + \frac{r^2\lambda^2}{\kappa_r} R(r) = 0 .$$

Let $\alpha^2 = \lambda^2/\kappa r$, and $\varepsilon = \alpha r$. By substituting $r = \varepsilon/\alpha$ into the above equation and simplifying the expression, the result is,

$$\varepsilon^2 \frac{d^2R}{d\varepsilon^2} + \varepsilon \frac{dR}{d\varepsilon} + \varepsilon^2 R = 0, \tag{2.33}$$

which is known as Bessel's equation with $n = 0$ [9]. It should be noted from (2.31), that

$$\mu = \omega^2 \kappa_z + \alpha^2 \kappa_r. \tag{2.24}$$

Time Solution

The solution of (2.28) is

$$U(t) = U_0 e^{-\mu t} = U_0 e^{-(\kappa_r \alpha^2 + \kappa_z \omega^2)t}. \tag{2.34}$$

Z-Solution

The general solution of (2.30) is

$$Z(z) = A\cos(\omega z) + B\sin(\omega z), \tag{2.35}$$

where A and B are constants. The boundary condition $Z(0) = 0$ requires that A=0, therefore,

$$Z(z) = B\sin(\omega z). \tag{2.36}$$

The boundary condition $Z(H) = 0$ requires that $\sin(\omega z) = 0$. This implies that $\omega H = j\pi$, where j is an integer. Therefore,

$$\omega_j = \frac{j\pi}{H}, \qquad \text{j} = 1, 2, 3, \ldots$$

is a set of valid values for ω, and any linear combination of these modes will still be a solution of (2.30). As a result, the most general solution is:

$$Z(z) = \sum_{j=1}^{\infty} B_j \sin(\omega_j z). \tag{2.37}$$

At this point, the coefficient *Bj* needs to be determined from the initial conditions (2.25). The initial conditions are enforced by expressing the initial condition in *Z(z)* in the form of a Fourier Series expansion [10], yielding

$$B_j = -\frac{4}{\pi j}, \text{ for j = 1, 3, 5 , ...}$$

and

$$B_j = 0, \text{ for j=2, 4, 6, ...}$$

A superposition of the initial conditions and the approximating Fourier series, for *j*=1,2,3,...,33, is shown in figure 2.11.

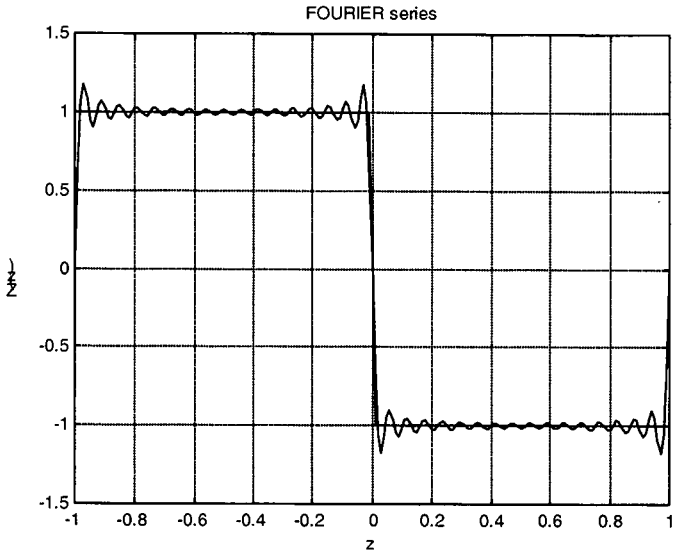

Figure 2.12: A Fourier series approximation of initial condition (2.25).

R-Solution

The most general solution of (2.33) is

$$R(r) = A\left[J_0(\alpha r) + bY_0(\alpha r)\right] \tag{2.38}$$

where A and b are constants. According to boundary condition (2.24),

$$R(r_{in}) = R(r_{out}) = 0 \tag{2.39}$$

for all time. For convenience sake, the range of $R(r)$ will be transformed from $[r_{in}, r_{out}]$ to $[\sigma, 1]$, where $\sigma = rin/rout$. At this point, a set of α's and b's that satisfy (2.39) needs to be found. The MATLAB routine *bessolro.m* performs this function (see appendix B.2).

Since it is desirable to have the quantity $R(r)Z(z)$ equal to -1 in the interior, the initial condition (2.25) will be modified as follows:

$$R(r) = \begin{cases} 0, & r = r_{in} \\ 1, & r \in (r_{in}, r_{out}) \\ 0, & r = r_{out} \end{cases}. \tag{2.40}$$

The functions that satisfy (2.39) are called eigenfuctions. The eigenfunctions of (2.39) are

$$p_j(\alpha_j r) = J_0(\alpha_j r) + b_j Y_0(\alpha_j r). \tag{2.41}$$

From Sturm-Liouville theory [11], the eigenfunctions must be orthogonal with respect to a weight function *w(r)*,

$$\int_\sigma^1 w(r) p_j(\alpha_j r) p_k(\alpha_k r) dr = 0,$$

where $j \neq k$.

In a similar way as before (with *Z(z)*), the function *R(r)* can be expressed in the form of a Bessel series. The Bessel series is composed of a linear combination of the eigenfunctions of (2.39). As a first step in building a Bessel series, the orthogonality of these eigenfunctions need to be tested.

Test for Orthogonality

Assume that for α_j and α_k, $j \neq k$. In addition to this, let $w(r)=r$. Therefore, using an integration property of bessel functions [9],

$$\begin{aligned} \int_\sigma^1 r p_j(\alpha_j r) p_k(\alpha_k r) dr &= \frac{r}{\alpha_k^{\,2} - \alpha_j^{\,2}} \left[\alpha_j p_k(\alpha_k r) p'_j(\alpha_j r) - \alpha_k p_j(\alpha_j r) p'_k(\alpha_k r) \right]_\sigma^1 \\ &= \frac{r}{\alpha_k^{\,2} - \alpha_j^{\,2}} \left[\alpha_j p_k(\alpha_k r) p'_j(\alpha_j r) - \alpha_k p_j(\alpha_j r) p'_k(\alpha_k r) \right. \\ &\qquad \left. - \alpha_j p_k(\alpha_k \sigma) p'_j(\alpha_j \sigma) + \alpha_k p_j(\alpha_j \sigma) p'_k(\alpha_k \sigma) \right]_\sigma^1 \\ &= 0, \quad \text{if } \alpha_j \neq \alpha_k. \end{aligned}$$

Bessel Series

A function $R(r)$ defined on an interval $[\sigma,1]$ can be approximated by the bessel series

$$R(r) = \sum_{k=1}^{\infty} A_k p_k(\alpha_k r) \tag{2.42}$$

where

$$A_k = \frac{1}{N_k} \int r R(r) p_k(\alpha_k r) dr \tag{2.43}$$

and

$$p_k(\alpha_k r) = J_0(\alpha_k r) + b_k Y_0(\alpha_k r)$$

such that $p_k(\alpha_k r) = p_k(\alpha_k) = 0$, for $k=1, 2, 3, \ldots$

In this particular case, $R(r)$ is given by [9], therefore,

$$A_k = \int_{\sigma}^{1} r p_k(\alpha_k r) dr = \frac{1}{N_k \alpha_k^{\,2}} \left[(J_1(\alpha_k) + b_k Y_1(\alpha_k)) - \sigma (J_1(\alpha_k \sigma) + b_k Y_1(\alpha_k \sigma)) \right]$$

is an expression for the bessel series coefficients. Figure 2.12 shows the initial condition for $R(r)$ with a bessel series approximation superimposed.

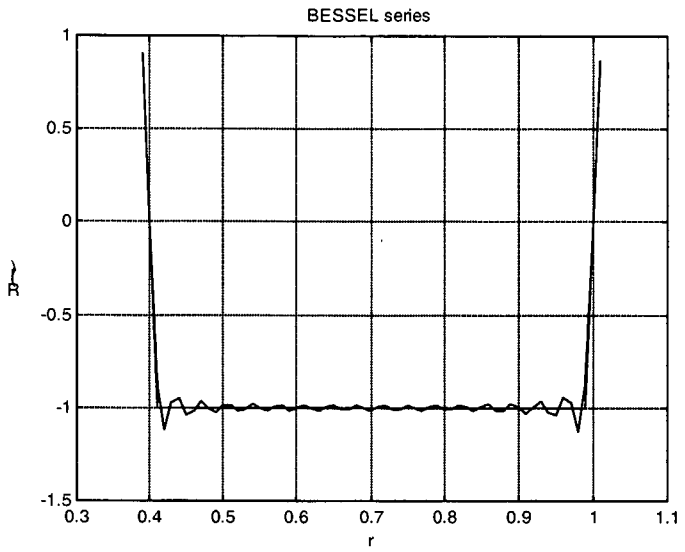

Figure 2.13: A Bessel series approximation for condition (2.24).

Specific Solution

The final solution satisfying the initial and boundary conditions is therefore

$$T(t,r,z) = \left(\sum_{j=1}^{\infty} B_j \sin(\omega_j z) \exp(-{\omega_j}^2 \kappa_z t) \right) \times \left(\sum_{k=1}^{\infty} A_k \left[J_0(\alpha_k r) + b_k Y_0(\alpha_k r) \right] \right) \times \exp(-{\alpha_k}^2 \kappa_r t). \tag{2.44}$$

2.9 Analytical Results

The program *bessol321.m*, in appendix B.9, implements equation (2.44). The analytical results for a 21 × 21 grid are shown below.

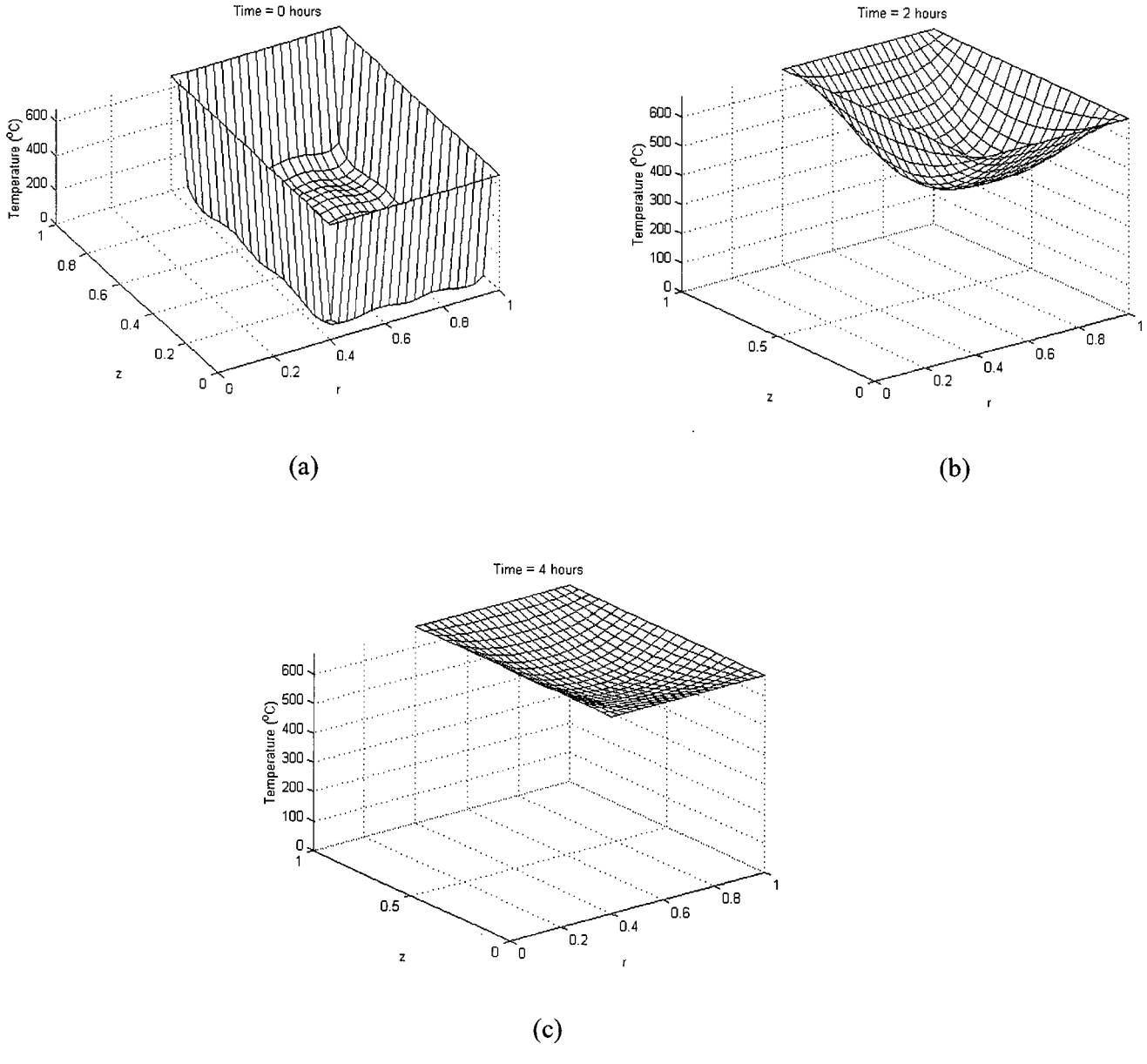

Figure 2.13: (a) to (c) Analytical temperature profiles for various times.

Note that at time = 0 hours, there are some oscillations in the base of the diagram. This is due to the fact that only a finite number of terms in both Fourier and Bessel series were used. As time increased, the temperature profile behaved in a similar manner to the numerical solution obtained in the previous section.

2.10 Comparison of Analytical and Numerical Solutions

In section 2.4, the finite difference method was used to solve the heat equation (2.4), for the case of axial symmetry, over a discretized solid cylinder with a concentric hole. The same equation was also solved analytically in the previous section. If the numerical solution is correct, it must compare favorably with the analytical solution.

As the number of finite difference grid points for the cylinder increase (for a fixed dimension) and the time step dt decreases, equation (2.9) approximates equation (2.4) more accurately. Therefore, if the solution obtained in section 2.7 (for constant heating on the boundaries) is correct then it should approach the analytical solution, for a given time, as the number of grid points increase and as the time-step dt tends to zero. An increase in the number of grid points can also be viewed as a decrease in the step lengths h_r and h_z (as the number of grid points increase h_r and h_z must tend to zero).

Tables 1, 2 and 3 show the temperature and percentage difference between the analytical and numerical solutions at the following times: 0.4 hours, 1.2 hours and 2 hours respectively. All three tables show the change between the two methods as the grid size increases and as the time-step decreases. The stability condition causes the time-step to decrease as the number of grid points increase.

The percentage difference was obtained by comparing the temperature difference to the temperature of the hottest region in the cylinder (in this case the boundaries experienced the highest temperature at 670°C).

Table 2.1: time = 0.4 hours

Grid Size	*dt* (m)	Maximum Temperature Difference (°C)	Maximum Percentage Difference (%)
5×5	0.4	188.26	28.10
10×10	0.08	82.048	12.25
15×15	0.0363636	35.68	5.33
20×20	0.02	22.87	3.414
25×25	0.0125	13.75	2.052
30×30	0.0088888	9.669	1.443
40×40	0.005	5.0332	0.7512
50×50	0.0030769	2.907	0.4339

Table 2.2: time = 1.2 hours

Grid Size	*dt* (m)	Maximum Temperature Difference (°C)	Maximum Percentage Difference (%)
5×5	0.4	162.8	24.30
10×10	0.08	39.39	5.88
15×15	0.0363636	18.35	2.739
20×20	0.02	10.07	1.503
25×25	0.0125	6.270	0.9358
30×30	0.0088888	4.345	0.6485
40×40	0.005	2.332	0.3480
50×50	0.0030769	1.361	0.2031

Table 2.3: time = 2 hours

Grid Size	*dt* (m)	Maximum Temperature Difference (°C)	Maximum Percentage Difference (%)
5×5	0.4	105.1	15.69
10×10	0.08	24.12	3.6
15×15	0.0363636	11.23	1.675
20×20	0.02	6.212	0.9271
25×25	0.0125	3.868	0.5772
30×30	0.0088888	2.704	0.4035
40×40	0.005	1.479	0.2208
50×50	0.0030769	0.8833	0.1318

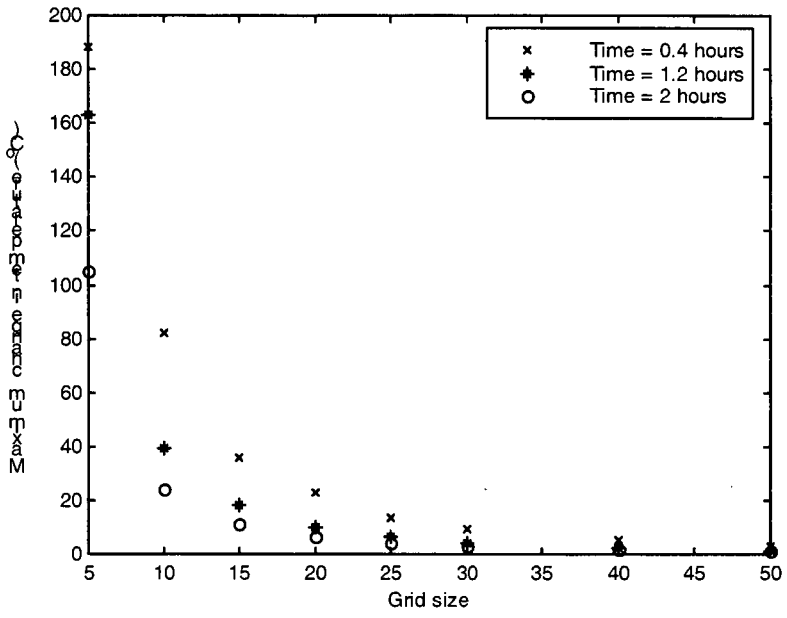

Figure 2.15: A graph of maximum change in temperature versus grid size.

A graph of the maximum change in temperature versus grid size, for tables 1,2 and 3 (for 0.4 hours, 1.2 hours and 2 hours), is shown in figure 2.15. At 0.4 hours, the maximum difference in temperature decreases rapidly until it becomes negligible at grid size of 50×50 and a time step of 0.003077 hours. Notice that the maximum difference decreases as time increases, as illustrated by the curves corresponding to 1.2 and 2 hours. This is as

a result of the fact that the temperature distribution moves closer to steady state as the time increases. At steady-state, the temperature of the entire cylinder reaches 670°C.

Chapter 3

Temperature model for a Cylindrical Coil

3.1 Introduction

In the previous chapter, heat transfer in a solid cylinder was treated as an approximation to a cylindrical coil. This was based on the assumption that the temperature dependence had no θ-dependence.

In this chapter, however, the effect of heat transfer along the coil spirals will be investigated. Once the model has been constructed, the first task will be to test whether the θ-dependence of temperature is appreciable or not. A comparison will also be made between the time evolution of the hottest and coldest regions in the coil. This will be done under temperature conditions similar to the batch annealing process.

3.2 Finite Difference Model

This section deals with the discretization of both the cylindrical coil and the heat equation for theta-dependence. The grid structure of the coils is introduced prior to the discussion regarding the heat equation.

3.2.1 Numerical Grid

The cylindrical coil was discretized into a series of coil slices stacked in the z-direction. These coil slices were divided into an equal number of sectors (see figure 3.1).

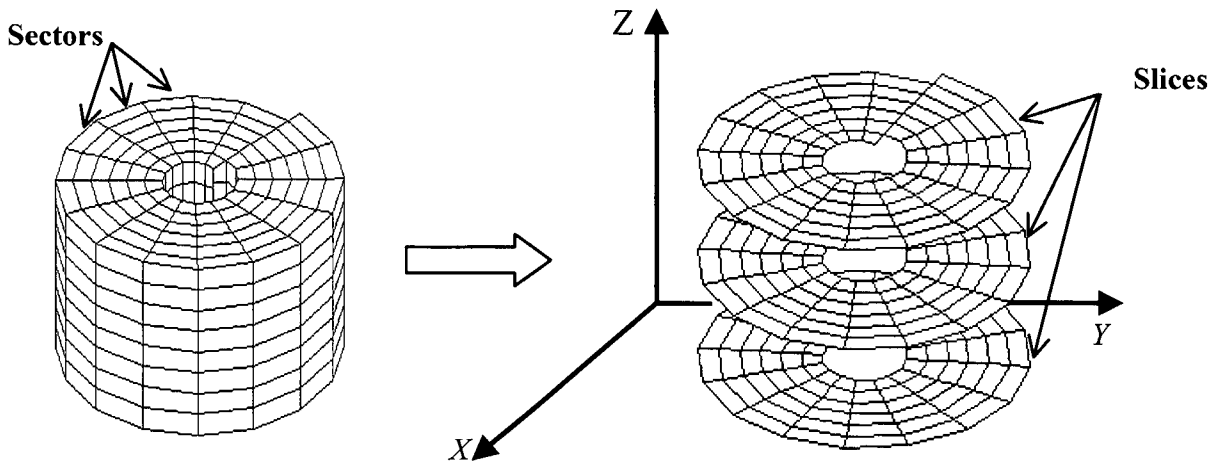

Figure 3.1: The cylindrical coil is discretized into sectors and slices.

Each individual slice is described by the following equation in polar coordinates:

$$r = m\theta + c, \tag{3.1}$$

where m and c are constants. The grid, in this case, was constructed using cartesian coordinates. This means that the x and y-values of each point on the coil grid are given by:

$$x = r\cos\theta \tag{3.2}$$

$$y = r\sin\theta \tag{3.3}$$

Note that the grid points of the coil are on the edges of each sector, such that if there are 16 sectors, then each coil spiral will have 16 elements. Thus, the entire grid can be viewed as a stack of matrices that specify each coil slice, as shown in figure 3.2.

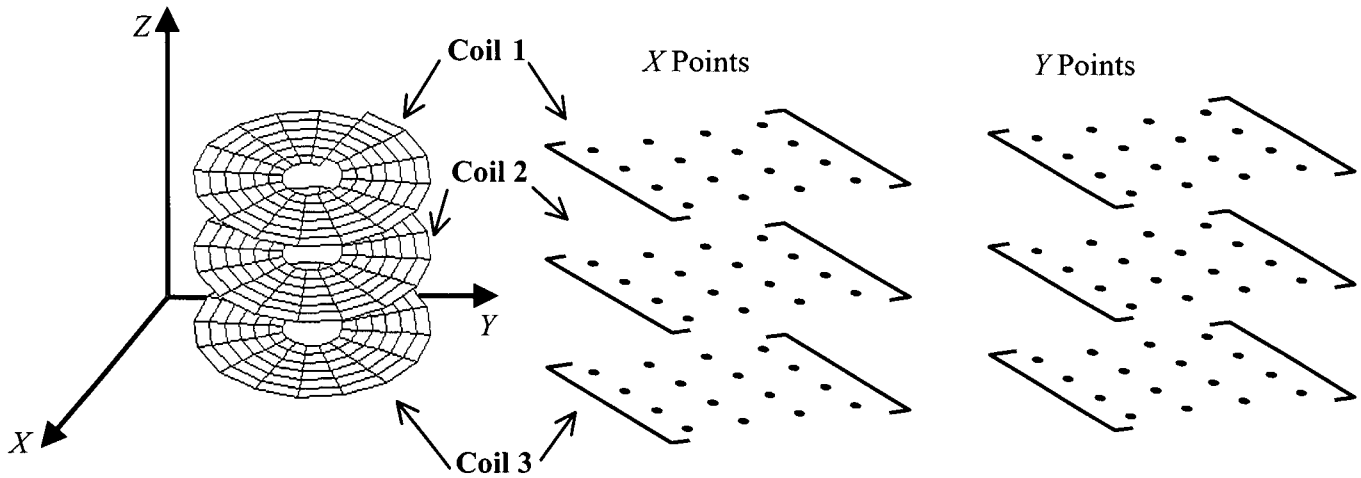

Figure 3.2: The X and Y matrix stacks specify the stack of coils.

Note that the matrices are arranged in the manner shown in figure 3.3. Each row of the X and Y matrices constitutes a spiral. In addition to that, each column of the X and Y matrices constitutes a sector.

Both X and Y matrices are structured in the following way:

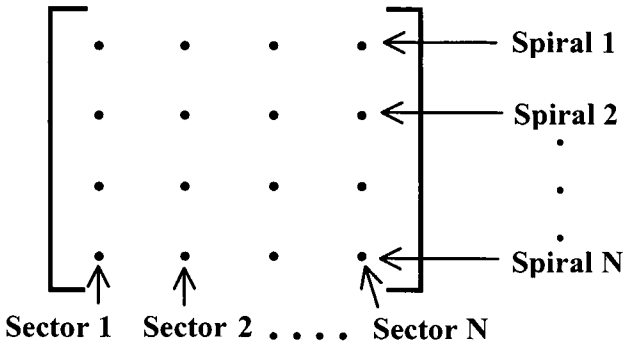

Figure 3.3: The X and Y matrix structure.

Therefore each spiral, with all its sections, is packed into a separate row in the matrix structure and each matrix in a stack describes a coil.

3.2.2 Discretized Heat Equation

From (2.2), the heat equation in cylindrical coordinates is:

$$\kappa_r \frac{1}{r}\frac{\partial T}{\partial r} + \kappa_r \frac{\partial^2 T}{\partial r^2} + \kappa_z \frac{1}{r^2}\frac{\partial^2 T}{\partial \theta^2} + \kappa_z \frac{\partial^2 T}{\partial z^2} = \frac{\partial T}{\partial t}.$$

Since the thermal conductivity is the same along the spirals as it is in the axial direction, it follows that:

$$\kappa_\theta = \kappa_z \qquad (3.4)$$

This expression can be discretized into the following finite difference equation:

$$\kappa_r \frac{1}{r_i}\left(\frac{T^n{}_{i+1,j,k} - T^n{}_{i-1,j,k}}{2h_r}\right) + \kappa_r\left(\frac{T^n{}_{i+1,j,k} - 2T^n{}_{i,j,k} + T^n{}_{i-1,j,k}}{h_r{}^2}\right) + \kappa_z \frac{1}{r_i{}^2}\left(\frac{T^n{}_{i,j+1,k} - 2T^n{}_{i,j,k} + T^n{}_{i,j-1,k}}{h_\theta{}^2}\right)$$

$$+\kappa_z\left(\frac{T^n{}_{i,j,k+1} - 2T^n{}_{i,j,k} + T^n{}_{i,j,k-1}}{k^2}\right) = \left(\frac{T^{n+1}{}_{i,j,k} - T^n{}_{i,j,k}}{\tau}\right)$$

After some re-arranging, the result is:

$$\begin{aligned} T^{n+1}{}_{i,j,k} &= T^n{}_{i,j,k} + \tau\kappa_r \frac{1}{r_i}\left(\frac{T^n{}_{i+1,j,k} - T^n{}_{i-1,j,k}}{2h_r}\right) \\ &+\tau\kappa_r\left(\frac{T^n{}_{i+1,j,k} - 2T^n{}_{i,j,k} + T^n{}_{i-1,j,k}}{h_r{}^2}\right) \\ &+\tau\frac{\kappa_z}{r_i{}^2}\left(\frac{T^n{}_{i,j+1,k} - 2T^n{}_{i,j,k} + T^n{}_{i,j-1,k}}{h_\theta{}^2}\right) \\ &+\tau\kappa_z\left(\frac{T^n{}_{i,j,k+1} - 2T^n{}_{i,j,k} + T^n{}_{i,j,k-1}}{h_z{}^2}\right) \end{aligned} \tag{3.5}$$

Since each row in the temperature matrix represents a spiral (figure 3.3), a central difference (appendix A) at a point with an index $i = 1$ will use a point at $i = N$ (or $i = -1$ is equivalent to $i = N$), where N is the number of points in a row. In a similar manner, $i = N+1$ is equivalent to $i = 1$. This is true for all values of indices j and k.

The stability conditions were obtained by substituting

$$T^n{}_{i,j} = \xi^n e^{\tilde{i}(i\omega_r + j\omega_\theta + k\omega_z)} \tag{3.6}$$

into equation (3.5) and following the procedure in section 2.5 of chapter 2. The result is

$$\tau \leq \frac{-8A}{\left(B^2 + 16A^2\right)}, \tag{3.7}$$

where

$$A = \left(-\frac{\kappa_r}{h_r^{\,2}} - \frac{\kappa_\theta}{h_\theta^{\,2}} - \frac{\kappa_z}{h_z^{\,2}} \right) \tag{3.8}$$

and

$$B = \frac{\kappa_r}{h_r r_{\min}}. \tag{3.9}$$

3.3 Initial Conditions

Initially, the coil is at room temperature. Then, a heating cycle (figure 1.2) is applied to all the boundary surfaces of the coil. In terms of the grid arrangement, it means that the first and last spiral of each coil in the stack must also be heated directly (figure 3.4).

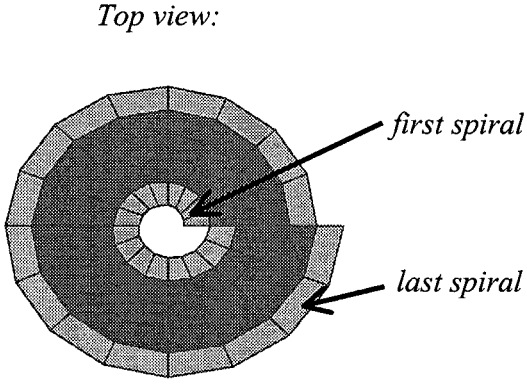

Figure 3.4: Top view of a cylindrical coil, with the first and last spirals highlighted.

In addition to this, the first and last coil slices in the stack must also be heated directly (these coils form the top and bottom of the cylindrical coil). In terms of the matrix arrangement of the grid, one can use a stack of temperature matrices and correlate each grid point to its corresponding temperature (as shown in figure 3.5).

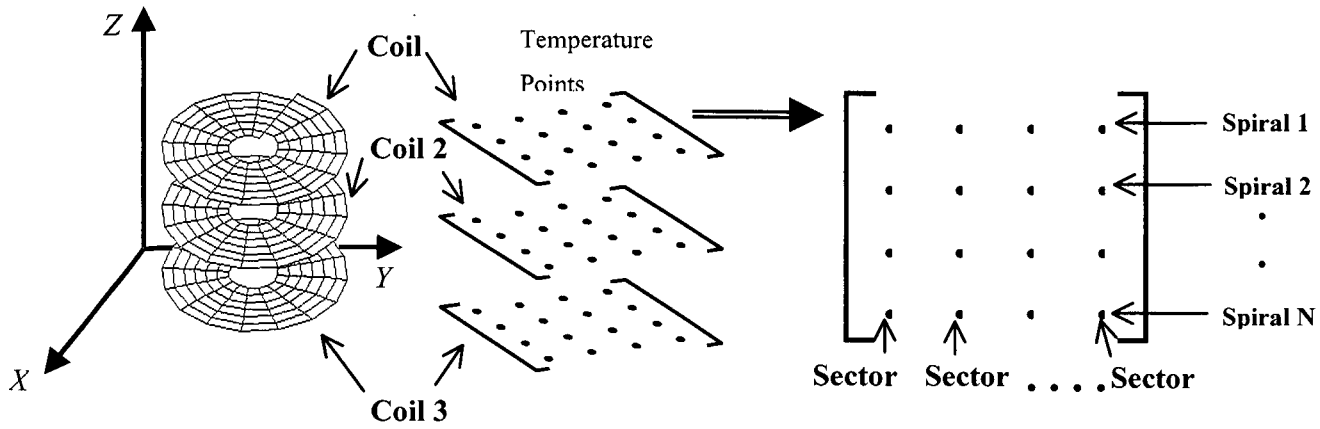

Figure 3.5: Structure of temperature matrix.

The initial conditions can now be implemented by allowing both the first and last rows of each temperature matrix to have the same value as the heating cycle at every instant. Once again, in addition to this, the first and last matrices in the stack must also have the same value as the heating cycle at every instant. The remaining matrix elements, corresponding to the interior of the cylindrical coil, are all at room temperature initially.

The heat equation was solved subject to the previously mentioned initial conditions. A computer program (called *thermd.m*) that solves equation (3.5) subject to the initial conditions (in the form of temperature matrices) was written in MATLAB (appendix C). This program also displays the calculated temperatures on the corresponding grid points. Note that the room temperature values for κ_r, κ_z and ρ were used throughout the calculation.

3.4 Numerical Results

The temperature distribution of the first sector of a coil with 16 sectors is shown in figure 3.6. In this particular case, the edges of the coil were heated at a constant temperature of 670°C. The inner and outer radii were chosen as $0.4m$ and $1.5m$, respectively, with each

spiral having a width of $0.1m$, which is 100 times the typical thickness (this was done for display purposes). The coil height is $1m$.

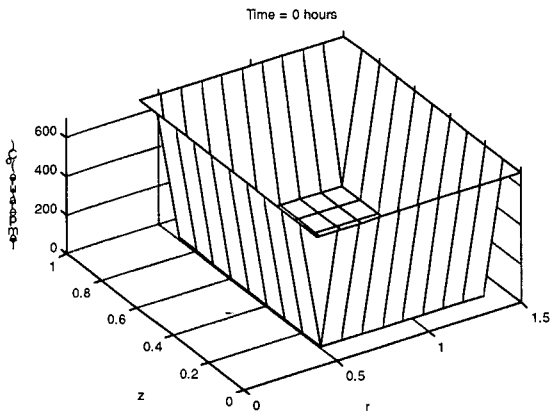

(a)

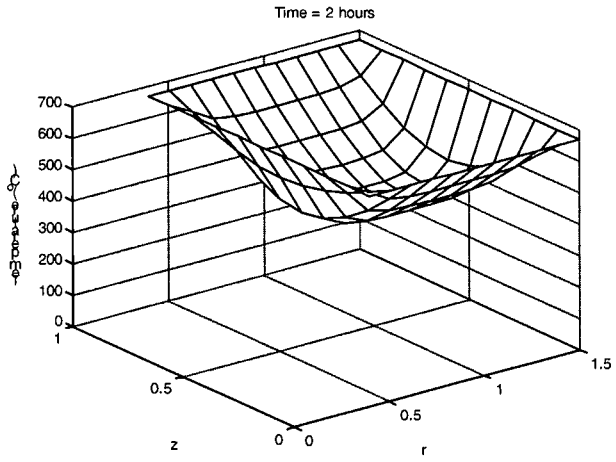

(b)

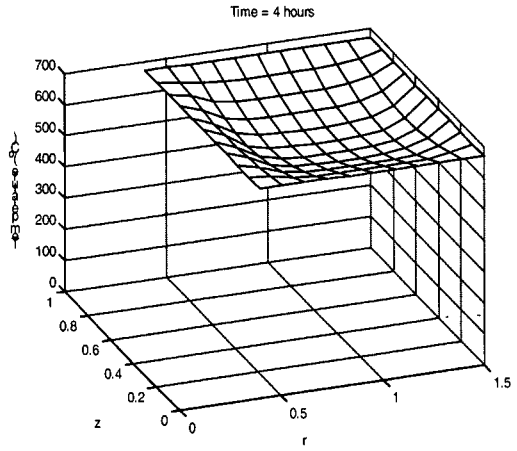

(c)

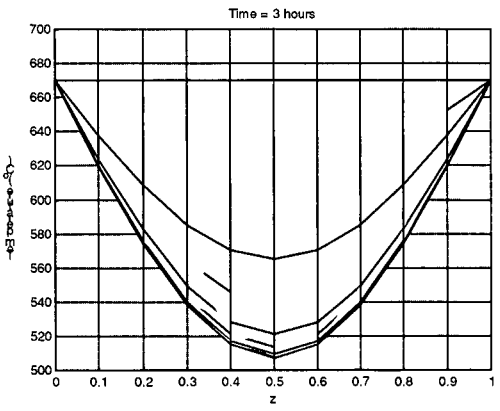

(d)

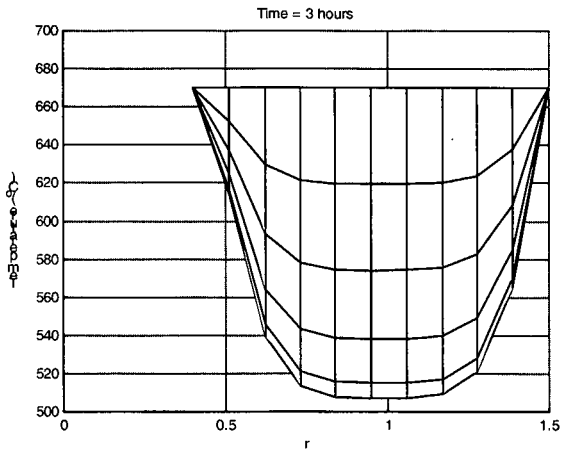

(e)

Figure 3.6: (a) to (c) Temperature profiles for the first sector a cylindrical coil with dimensions as stated in the beginning of section 3.4. (d) A cross sectional profile of the first sector, in the z-direction. (e) A cross sectional profile of the first sector, in the r-direction.

It can be seen, from figure 3.6, that the temperature profile follows a similar pattern as the solution of a solid cylinder with a concentric hole. There is symmetry in the *z*-direction and anti-symmetry in the *r*-direction. The shape of the curve in the r-direction is not completely identical to the two-dimensional case, this difference can be attributed to heat flow along the spirals (remember that the spirals in this case are 100 times thicker than usual).

Another display of the coil during the heating process is shown in figure 3.7. A coil slice from the center is shown together with a side view of the first sector, at a time of 2 hours.

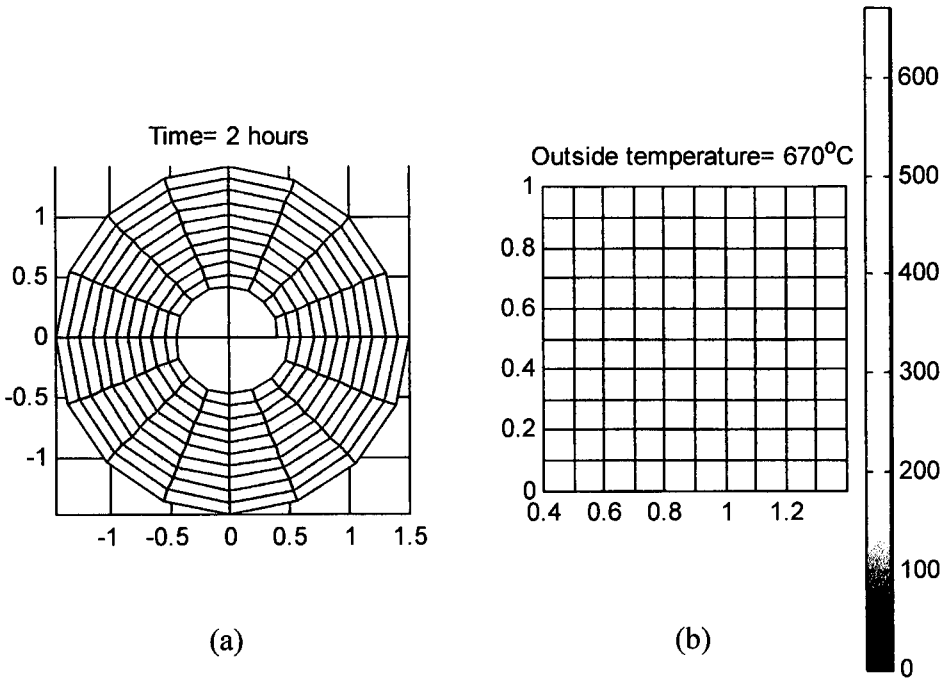

Figure 3.7: (a) A diagram of the temperature distribution in the center slice of a coil, with dimensions as stated at the beginning of section 3.4. (b) The temperature distribution of the first sector, in the z-direction. These distributions were taken after 2 hours.

Note that a cold region also develops in this case. From figure 3.6, one can see where it is situated. It appears to be a ring situated in the center of the cylindrical coil. When the coil is viewed from the top, the radius of the cold region is positioned at around half the distance between the inner and outer radius.

The time evolution of the coil edge and cold region, when the coil is subjected to a temperature ramp (see figure 1.2), is shown below (figure 3.8). These results were also generated from the program *thermd.m* in appendix C.

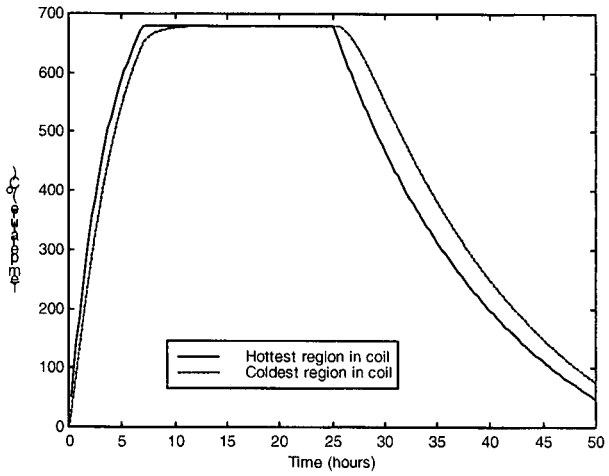

Figure 3.8: The time evolution of the hottest region and coldest region during batch annealing.

3.5 Theta dependence

A possible way to examine whether the heat flow along the θ-direction is appreciable or not is to compare the temperature distributions of the sectors. Note that the top and bottom slices have equal temperatures (all the sectors are at the same temperature) because of the effect of direct heating. The coil slices just below these two surfaces also experience this effect, but to a lesser degree. As a result, the middle coil slice should have the largest temperature differences between sectors, as a result of heat flow along the spirals. For this reason, the center coil slice will be used to test for θ-dependence of temperature.

The extent of θ-dependence can be measured by monitoring the maximum difference between sectors that are situated opposite to each other. For axial symmetry, the maximum difference would be zero.

Testing for θ-dependence in a coil with typical dimensions, using the MATLAB program *thermd.m* (appendix C) that solves a cylindrical coil three-dimensionally (using equation (3.5) with the initial conditions of section 3.3) proved to be impractical, due to the

amount of computation time necessary to complete the calculation. This problem was surmounted by performing a θ-dependence test for three simpler cases and using the resulting trend to make a projection for a realistic coil.

The dimensions for all three cases are as follows:

Coil height:	$1m$
Inner radius:	$0.6m$
Outer radius:	$1.4m$
Number of sectors:	8
Number of slices:	10

The width w and number of spirals N were varied as follows:

Case 1:

$w = 0.1m$

$N = 8$

Case 2:

$w = 0.05m$

$N = 16$

Case 3:

$w = 0.025m$

$N = 32$

The number of spirals double as the spiral width is halved. The maximum temperature difference between sectors 1 and 4 are shown in tables 3.1, 3.2 and 3.3 for the three cases. This difference is shown with the corresponding number of iterations. The number of elapsed iterations are proportional to the elapsed time, with $1/dt$ being the proportionality constant.

Table 3.1: Case 1, $dt = 0.1993m$, $w = 0.1m$ with 8 coils turns.

Number of Iterations	Maximum Difference (^{o}C)
1	0
2	6.917
3	12.97
4	18.27
5	22.91
10	33.03
20	29.37
30	20.82
40	13.99
50	9.233
60	6.051
70	3.949
80	2.570
90	1.669
100	1.081

Table 3.2: Case 2, $dt = 0.1614m$, $w = 0.05m$ with 16 coil turns.

Number of Iterations	Maximum Difference (°C)
1	0
2	6.388
3	10.48
4	13.17
5	14.98
10	16.51
20	13.06
30	10.53
40	7.910
50	5.776
60	4.167
70	2.985
80	2.147
90	1.546
100	1.110

Table 3.3: Case 3, $dt = 0.0917$ hours, $w = 0.025m$ with 32 coil turns.

Number of Iterations	Maximum Difference (°C)
1	0
2	3.889
3	4.715
4	5.127
5	5.369
10	6.368
20	6.764
30	6.294
40	5.598
50	4.809
60	4.123
70	3.517
80	2.971
90	2.493
100	2.083

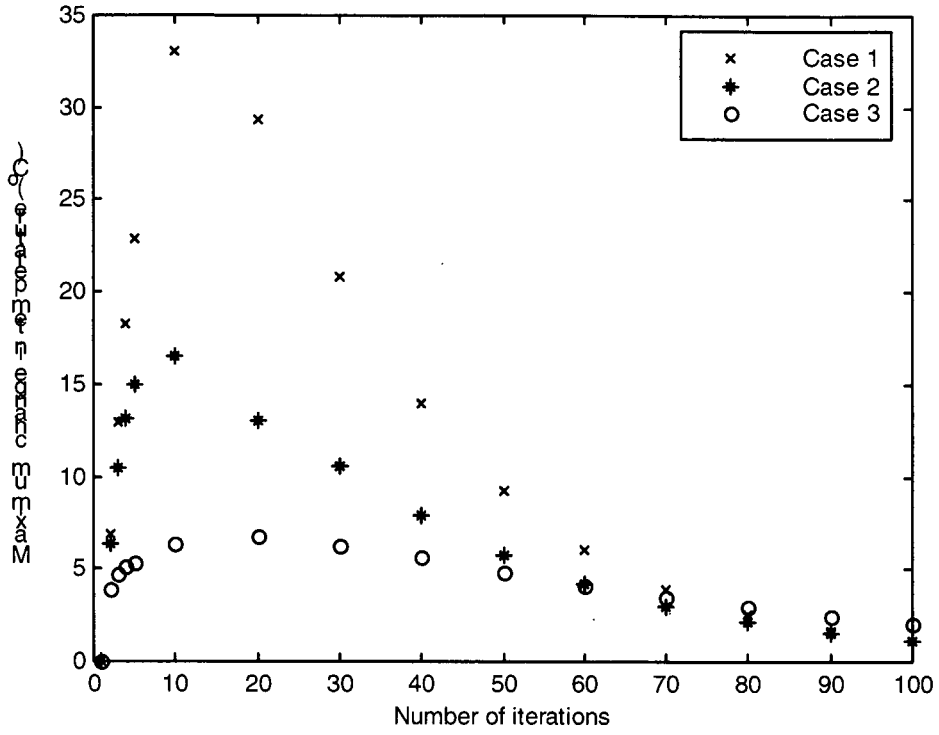

Figure 3.9: A graph of maximum change in temperature versus number of iterations, for cases 1, 2 and 3.

According to figure 3.9, at the instant when the coil is heated initially, the maximum difference between sectors 1 and 4 is zero. This is because heat flow along the spirals has not occurred yet. But, as the number of iterations increase, the heat flow along the spirals increases the maximum difference between sectors 1 and 4 until the maximum difference curve reaches its highest value (at about 10 iterations). Beyond this point, the effect of heat transfer in the radial and z-direction increases, as the temperature moves closer to steady state. This causes the difference between sectors to decrease gradually until it eventually reaches zero, when the thermal gradients have leveled out.

Figure 3.9 also shows that the highest point in the maximum difference curve decreases as number of spirals increase and as the spiral width decreases. This observation can be used to determine a trend. It is useful to determine how the highest point in the maximum difference curve changes as the division number increases. The division number is defined as the number of times that the spiral width w is halved plus 1. For case 1, the

division number is 1, for case 2, the division number is 2 and for case 3, the division number is 3.

The maximum values for the three cases were plotted against division number, and a curve was fitted through the relevant points, see figure 3.10.

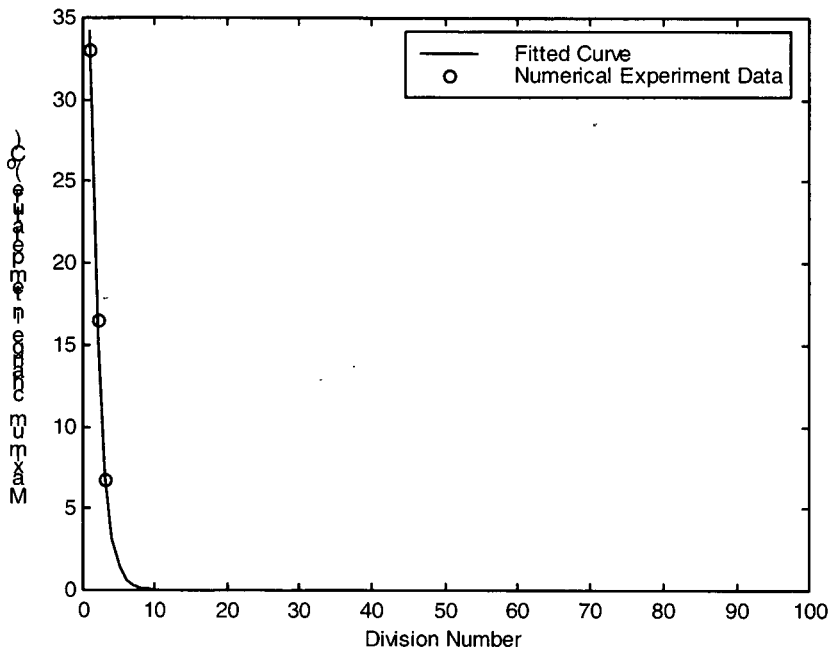

Figure 3.10: A graph of maximum change in temperature versus division number.

The equation of the fitted curve is,

$$Y = A\exp(-\lambda x), \tag{3.10}$$

where A = 75.45°C and $\lambda = 0.7929m^{-1}$. It is expected that A and λ will depend on κ_r, κ_z and the dimensions of the coil.

The θ-dependence of a realistic coil would correspond to a division number of 100, where the spiral width $w = 0.001m$ and the number of turns N = 800. The absolute

maximal temperature difference at a division number of 100 is 2.77×10^{-33} °C. This shows that for a realistic coil, the θ-dependence is negligible and that the coil can be treated as a solid cylinder when modeling heat transfer.

Chapter 4

ELASTICITY THEORY

4.1 Introduction

The theory of elasticity basically deals with the study of stress, strain and deformation of materials in the elastic limit. In this field, the behaviour of the material as a whole is of importance (individual molecules are not considered). This is the continuum concept of matter. Stress is defined as the force experienced by a plane of a body per unit area (*stress=force/area*). Strain, on the other hand, is the resulting distortion of the body divided by the original dimension (*strain=distortion/original dimension*).

The main objective of the following sections is to derive some equations that will be instrumental in determining the thermal stress in a material that has a given temperature distribution. Pertinent concepts of elasticity will first be introduced in cartesian coordinates and thereafter in polar coordinates.

Brief discussions regarding stress, strain and the notion of a tensor have been included as precursors to the derivations. The equilibrium conditions for boundary traction, in cartesian coordinates, are derived in section 4.4. These equations are used, in the ensuing section, to arrive at the equilibrium conditions (in cartesian coordinates) for the interior of material. Some equations of strain, which relate strain components to displacements, are

developed from section 4.6 to 4.7. These equations of strain are later used to arrive at the compatibility equations (section 4.8).

Hooke's law for isotropic media is introduced in section 4.9, and it provides the necessary background for the discussion on thermal stress that follows afterwards. The equilibrium conditions and the equations of strain are derived for polar coordinates in the subsequent sections.

4.2 Stress and Strain

Figure 4.1, which shows a bar of initial length L_0 and cross-sectional area A, illustrates basic one-dimensional stress and strain. When an axial force F acts on area A, as shown in figure 4.1b, the resulting stress and strain is given by the equations in figure 4.1b.

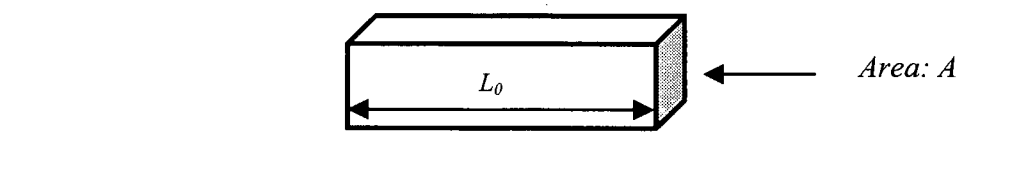

(a)

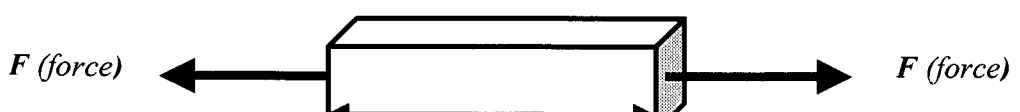

$Stress = F/A$

$Strain = \Delta L/L_0$

(b)

Figure 4.1: (a) Initial bar. (b) Bar during the application of a force, with a force-induced lengthening of ΔL.

This diagram shows an example of a normal stress and a normal strain. A normal stress is an application of a force on some surface of a body in a direction that is perpendicular to that surface. Normal strain, on the other hand, is caused by a normal stress. The resulting

displacement occurs in a direction that is perpendicular to the surface on which the stress is applied.

A shearing stress occurs when a force is applied in a parallel direction to a particular surface on a body. In a similar way to normal strain, shearing strain is also caused by a shearing stress. But in this case, the resulting displacement occurs in a direction that is parallel to the face upon which the stress has been applied (see figure 4.2).

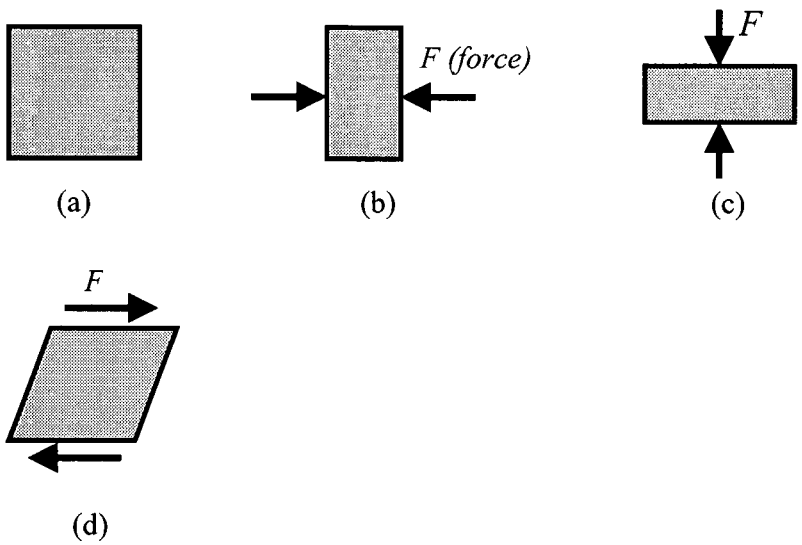

Figure 4.2: (a) Initial block element. (b) Deformation resulting from a horizontal normal stress. (c) Deformation resulting from a vertical normal stress. (c) Deformation resulting from a shearing stress.

It should be noted, however, that in realistic situations, materials are subjected to a mixture of normal and shearing stresses.

4.3 The Stress Tensor

The notion of a tensor will be used extensively throughout the treatment of elasticity in this text. A basic understanding of tensors can be gained by examining some of the stress tensor properties.

When dealing with a two or three-dimensional body, it is useful to express stresses and strains in tensor notation. The stress tensor σ_{ij} gives all the stresses that act on each point throughout the material. It is therefore a function of position. The stress tensor for a three-dimensional material, with axes pointing in the x_1, x_2 and x_3 directions is,

$$\sigma_{ij} = \begin{bmatrix} \sigma_{11} & \sigma_{12} & \sigma_{13} \\ \sigma_{21} & \sigma_{22} & \sigma_{23} \\ \sigma_{31} & \sigma_{32} & \sigma_{33} \end{bmatrix}. \tag{4.1}$$

Figure 4.3 shows the stress tensor components on a material element. In figure 4.3, the x_1 face is the face that is perpendicular to the x_1 axis. This convention also holds for the x_2 and x_3 faces.

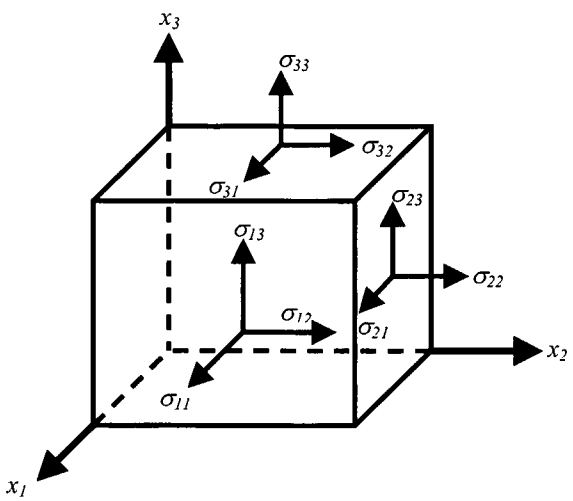

Figure 4.3: The nine stress tensor components.

The stress σ_{11} represents the stress on the x_1 face in the x_1 direction. The stresses σ_{22} and σ_{33} can be explained in a similar manner. These are all normal stresses. Note, however, that σ_{12} is the shearing stress on the x_1 face in the x_2 direction. Similarly, σ_{23} and σ_{13} represent the stress on the x_2 face in the x_3 direction and the stress on the x_1 face in the x_3 direction, respectively. Since each element in a continuum should be in equilibrium, it follows that:

$$\sigma_{12} = \sigma_{21},$$

$$\sigma_{23} = \sigma_{32},$$

and (4.2)

$$\sigma_{13} = \sigma_{31}.$$

If (4.2) does not hold, the element will rotate.

4.4 Equilibrium Conditions for Boundary Traction

This section will seek to obtain some equilibrium conditions for a material element that experiences boundary traction [12]. The relationship between an external applied stress $\mathbf{t_n}$ and the internal stress tensor σ_{ij} is investigated here.

Consider a tetrahedron element of some continuum with one face on the surface, as shown in figure 4.4. Let ABC be the face on the surface of the continuum.

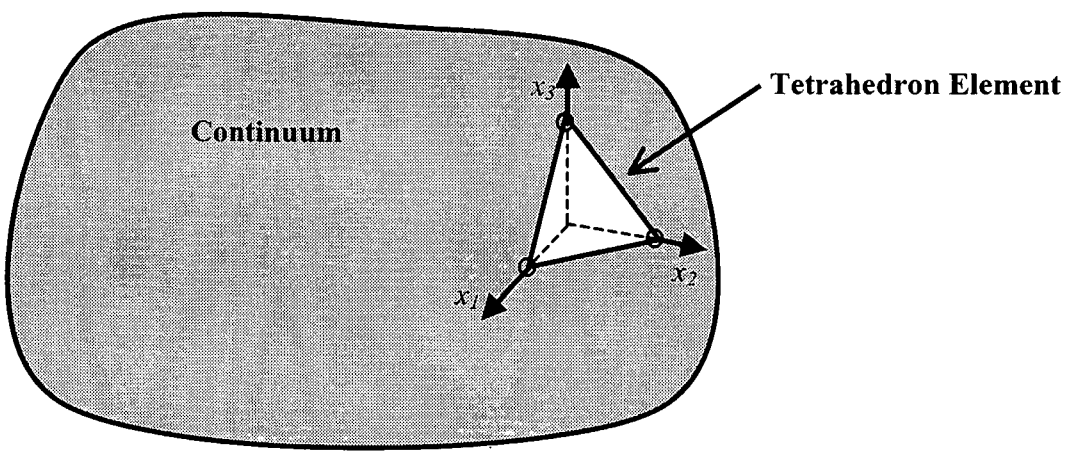

(a)

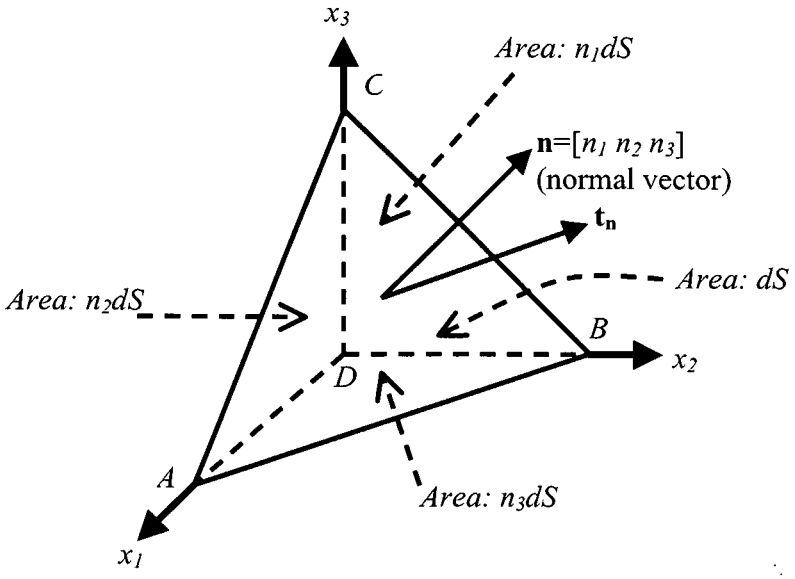

(b)

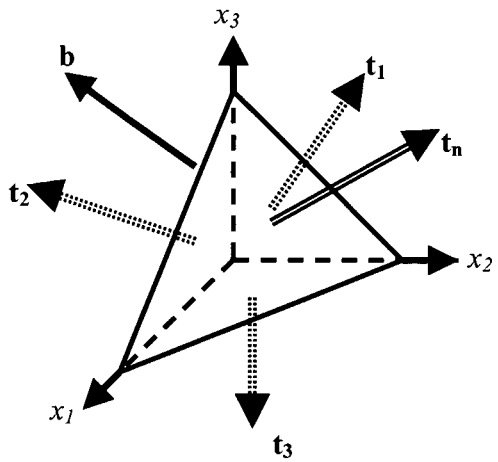

(c)

Figure 4.4: (a) Continuum with a tetrahedron element. (b) An enlargement of the element with axes drawn along the perpendicular edges of the tetrahedron. (c) An illustration of the external forces on the element.

Suppose that there are body forces acting on this element and **b** is the resultant body force per unit volume. Suppose also, that some external stress $\mathbf{t_i}$ (also referred to as the traction)

is applied on the various faces of the element ($\mathbf{t_n}$ on *ABC*, $\mathbf{t_1}$ on *BDC*, $\mathbf{t_2}$ on *ADC* and $\mathbf{t_3}$ on *ADB*), as shown in Fig 4.4c.

The traction on face *BDC* (which can also be considered as the x_1 face because it is perpendicular to the x_1 axis) of the element (t_1) is given by:

$$\mathbf{t_1} = \sigma_{11}\mathbf{i} + \sigma_{12}\mathbf{j} + \sigma_{13}\mathbf{k}, \quad (4.3a)$$

or alternatively: $\mathbf{t_1}$ is equal to the stress on face x_1 in the x_1 direction plus the stress on the x_1 face in the x_2 direction plus the stress on the x_1 face in the x_3 direction. By using similar reasoning, the following relations can be written:

$$\mathbf{t_2} = \sigma_{21}\mathbf{i} + \sigma_{22}\mathbf{j} + \sigma_{23}\mathbf{k} \quad (4.3b)$$

and

$$\mathbf{t_3} = \sigma_{31}\mathbf{i} + \sigma_{32}\mathbf{j} + \sigma_{33}\mathbf{k}. \quad (4.3c)$$

As shown in figure 4.4b, *dS* is the area of face *ABC*. It thus follows that the area of face x_1 is the projected area $n_1 dS$. Similar results also hold for faces x_2 and x_3 which have areas $n_2 dS$ and $n_3 dS$ respectively. In order for the element to be in equilibrium, the forces due to $\mathbf{t_1}$, $\mathbf{t_2}$, $\mathbf{t_3}$, $\mathbf{t_n}$ and **b** must add up to zero, that is:

$$\mathbf{t_n} dS - \mathbf{t_1} n_1 dS - \mathbf{t_2} n_2 dS - \mathbf{t_3} n_3 dS + \rho \mathbf{b} dV = 0. \quad (4.4)$$

In the limit as *dS* tends to 0, *dV* tends to 0 much faster, since *dS* is a square of a side while *dV* is a cube of a side. Therefore, equation (4.4) can be approximated by

$$\mathbf{t_n} - \mathbf{t_1} n_1 - \mathbf{t_2} n_2 - \mathbf{t_3} n_3 = 0. \quad (4.5)$$

Note that the dS cancels out. If the values of $\mathbf{t_1}$, $\mathbf{t_2}$, $\mathbf{t_3}$ (equations 4.3a to 4.3c) are substituted into (4.5), the following expression is obtained:

$$\mathbf{t_n}=(\sigma_{11}\mathbf{i} + \sigma_{12}\mathbf{j} + \sigma_{13}\mathbf{k})n_1 + (\sigma_{21}\mathbf{i} + \sigma_{22}\mathbf{j} + \sigma_{23}\mathbf{k})n_2 + (\sigma_{31}\mathbf{i} + \sigma_{32}\mathbf{j} + \sigma_{33}\mathbf{k})n_3$$

$$=(\sigma_{11}n_1 + \sigma_{21}n_2 + \sigma_{31}n_3)\mathbf{i} + (\sigma_{12}n_1 + \sigma_{22}n_2 + \sigma_{32}n_3)\mathbf{j} + (\sigma_{13}n_1 + \sigma_{23}n_2 + \sigma_{33}n_3)\mathbf{k}$$

$=\sum\mathbf{n}$, where

$$\Sigma = \begin{bmatrix} \sigma_{11} & \sigma_{12} & \sigma_{13} \\ \sigma_{21} & \sigma_{22} & \sigma_{23} \\ \sigma_{31} & \sigma_{32} & \sigma_{33} \end{bmatrix} \text{ and } \mathbf{n}= \begin{bmatrix} n_1 \\ n_2 \\ n_3 \end{bmatrix}. \tag{4.6}$$

Therefore:

$$\mathbf{t_n} = \sum\mathbf{n}. \tag{4.7}$$

This expression relates the external applied stress $\mathbf{t_n}$ to the internal stress tensor $\sum$ and it will be incorporated into the equilibrium conditions of the material as a whole in the following section.

4.5 Derivation of Equilibrium Conditions

In order for each element to remain in equilibrium, certain relationships between the various stress components and the body force must exist. These equations are known as the equilibrium conditions [12]. These conditions must be satisfied at all points throughout the interior of a body, regardless of the applied stress.

Consider an arbitrary volume V of a continuum that is subjected to both surface and body forces (see figure 4.5).

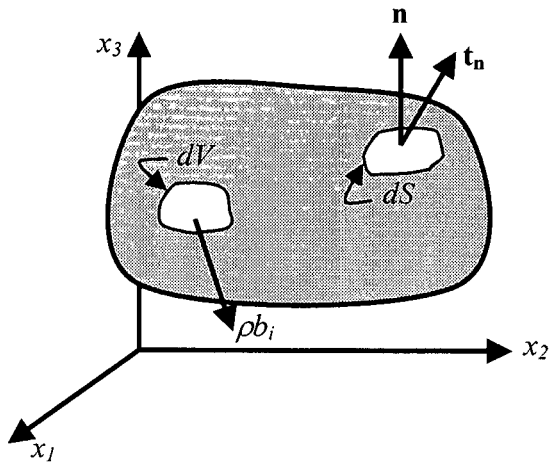

Figure 4.5: A continuum of volume V that is subjected to surface and body forces.

In order for this body to be in equilibrium, both the surface and body forces must add up to zero at each point of the continuum. It thus follows that,

$$F_{total} = \int_S \mathbf{t}_n \cdot \mathbf{n} dS + \int_V \rho b dV = 0,$$

where **n** is a unit vector normal to the surface. According to Gauss's theorem:

$$\int_S \mathbf{V} \cdot \mathbf{n} dS = \int_V \nabla \cdot \mathbf{V} dV,$$

therefore

$$\int_V \nabla \cdot \mathbf{t}_n dV + \int_V \rho \mathbf{b} dV = 0.$$

Since this expression is valid for any shape, it follows that:

$$\nabla \cdot \mathbf{t}_n + \rho \mathbf{b} = 0. \tag{4.8}$$

When (4.7) is substituted into the above equation, the result is:

$$\nabla \cdot (\Sigma) + \rho \mathbf{b} = 0.$$

In tensor notation (see appendix D), the above mentioned result can be expressed as:

$$\sigma_{ji,j} + \rho b_i = 0. \tag{4.9}$$

This is the set of equilibrium conditions for the interior points of a body. The expanded form is shown below:

$$\frac{\partial \sigma_{11}}{\partial x_1} + \frac{\partial \sigma_{12}}{\partial x_2} + \frac{\partial \sigma_{13}}{\partial x_3} + \rho b_1 = 0,$$

$$\frac{\partial \sigma_{21}}{\partial x_1} + \frac{\partial \sigma_{22}}{\partial x_2} + \frac{\partial \sigma_{23}}{\partial x_3} + \rho b_2 = 0,$$

$$\frac{\partial \sigma_{31}}{\partial x_1} + \frac{\partial \sigma_{32}}{\partial x_2} + \frac{\partial \sigma_{33}}{\partial x_3} + \rho b_3 = 0.$$

4.6 Lagrangian and Eulerian Descriptions of Deformation

When a continuous medium is deformed, the particles that comprise the medium move along particular paths. The motion of these particles can be expressed by equations of the form

$$x_i = x_i(X_1, X_2, X_3, t) = x_i(\mathbf{X},t) \text{ or } \mathbf{x} = \mathbf{x}(\mathbf{X},t) \tag{4.10}$$

where $X_1X_2X_3$ and $x_1x_2x_3$ are two sets of coordinate systems corresponding to the initial (undeformed) and final (deformed) states [12], see figure 4.6.

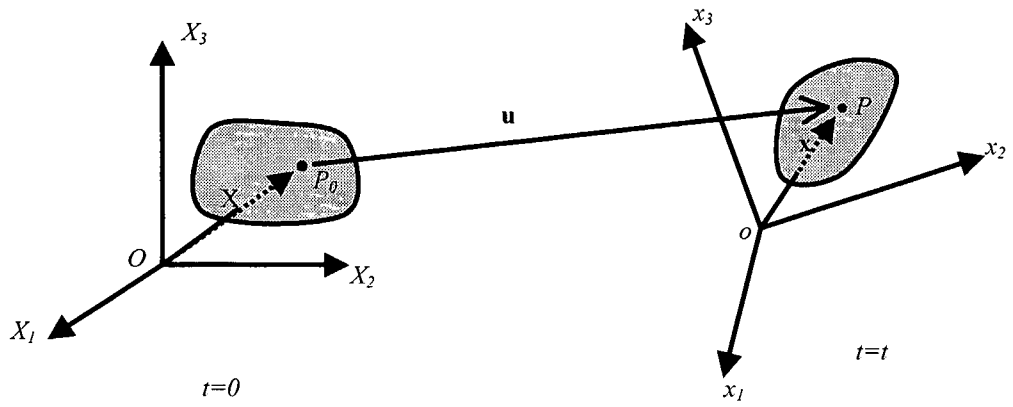

Figure 4.6: At t=0, the material is in an undeformed state. The material is deformed at t=t. There are two sets of coordinate systems corresponding to the initial and final states. Vector $\mathbf{X}$ *points from the origin of the* $X_1X_2X_3$ *axes to* P_0 *and vector* $\mathbf{x}$ *points from the origin of the* $x_1x_2x_3$ *axes to P.*

The particle that occupied the point (X_1, X_2, X_3) at $t = 0$ now occupies (x_1, x_2, x_3) at $t = t$ (after deformation has occurred). So (4.10) is a mapping of the initial coordinates at $t = 0$ onto the coordinate system at $t = t$. A one-to-one mapping with continuous partial derivatives is assumed. The deformation, as given by (4.10), is known as the Lagrangian description.

If the deformation is given by equations of the form

$$X_i = X_i(x_1, x_2, x_3, t) \text{ or } \mathbf{X} = \mathbf{X}(\mathbf{x},t), \qquad (4.11)$$

then it is known as the Eulerian description. Once again, a one-to-one mapping with continuous partial derivatives is assumed. As a result of this assumption, it follows that (4.10) and (4.11) are unique inverses of each other. This also implies that the Jacobian

$$J = \left|\frac{\partial x_i}{\partial Xj}\right| \neq 0 .$$

The Eulerian description will be used in the following section to derive a relation between deformation and strain.

4.7 Deformation and Strain Tensors

The relationship between the deformation and strain is embodied in the Eulerian strain tensor [12]. This relationship allows one to calculate the deformation that a body experiences, as a result of strain.

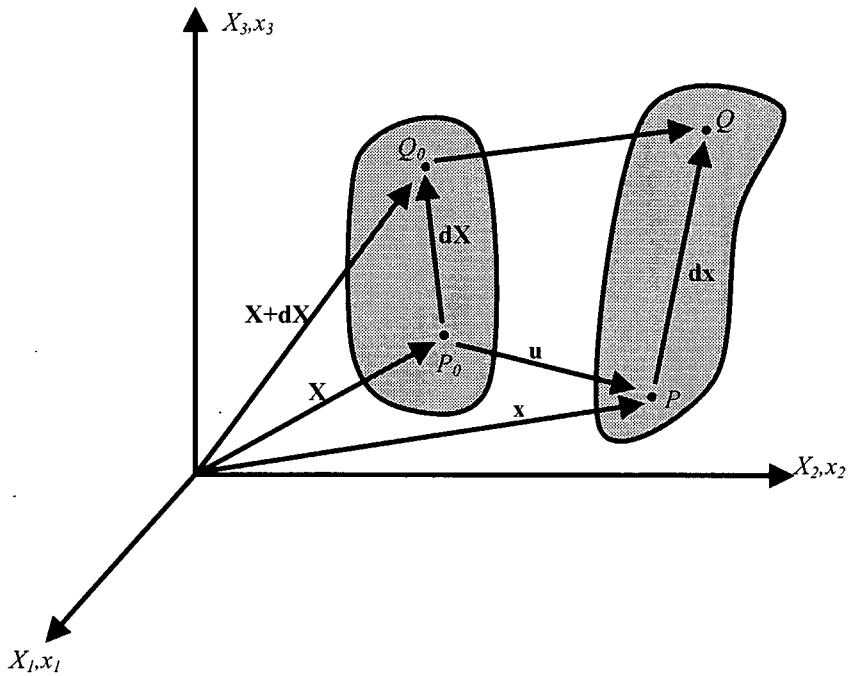

Figure 4.7: A diagram showing a continuum before and after deformation, with the corresponding coordinate axes superposed.

The previous diagram (figure 4.7) shows a continuum both before and after deformation with the corresponding coordinate axes superposed ($X_1X_2X_3$ is for the undeformed state and $x_1x_2x_3$ is for the deformed state). The particles that are situated at Q_0 and P_0 ,before deformation, move to points Q and P respectively, after deformation. Let **u** be the displacement between the deformed and undeformed states, so **du** = **dx**-**dX**.

The square of the length between P_0 and Q_0 is

$$(dX)^2 = \mathbf{dX}.\mathbf{dX} = dX_i dX_i \qquad \text{(summation is implied)} \qquad (4.12)$$

but from the chain rule,

$$dX_i = \frac{\partial X_i}{\partial x_j} dx_j. \qquad (4.13)$$

Therefore,

$$(dx)^2 - (dX)^2 = dx_i dx_i - dX_i dX_i$$

$$= dx_i dx_i - \frac{\partial X_i}{\partial x_j} dx_j \frac{\partial X_i}{\partial x_k} dx_k$$

$$= \delta_{ij}\delta_{ik} dx_j dx_k - \frac{\partial X_i}{\partial x_j} \frac{\partial X_i}{\partial x_k} dx_j dx_k$$

$$= \left(\delta_{ij}\delta_{ik} - \frac{\partial X_i}{\partial x_j} \frac{\partial X_i}{\partial x_k} \right) dx_i dx_k$$

$$= \left(\delta_{jk} - \frac{\partial X_i}{\partial x_j} \frac{\partial X_i}{\partial x_k} \right) dx_i dx_k \qquad (4.14)$$

Let the value in brackets equal $2E_{jk}$, where E_{jk} is the Eulerian strain tensor such that:

$$E_{jk} = \frac{1}{2} \left(\delta_{jk} - \frac{\partial X_i}{\partial x_j} \frac{\partial X_i}{\partial x_k} \right) dx_i dx_k. \qquad (4.15)$$

It thus follows that,

$$(dx)^2-(dX)^2=2E_{jk}dx_idx_k$$

But since $u_k = x_k-X_k$ (this is the displacement between the deformed and undeformed states)

The following can be written:

$$X_i = x_i-u_i \tag{4.16}$$

and

$$\frac{\partial X_i}{\partial x_j}=\frac{\partial}{\partial x_j}(x_i-u_i)=\frac{\partial x_i}{\partial x_j}-\frac{\partial u_i}{\partial x_j}=\delta_{ij}-\frac{\partial u_i}{\partial x_j}. \tag{4.17}$$

Therefore

$$E_{jk}=\frac{1}{2}\left[\delta_{jk}-\left(\delta_{ij}-\frac{\partial u_i}{\partial x_j}\right)\left(\delta_{ik}-\frac{\partial u_i}{\partial x_k}\right)\right]$$

$$=\frac{1}{2}\left[\delta_{jk}-\delta_{ij}\delta_{ik}+\delta_{ij}\frac{\partial u_i}{\partial x_k}+\delta_{ik}\frac{\partial u_i}{\partial x_j}-\frac{\partial u_i}{\partial x_j}\frac{\partial u_i}{\partial x_k}\right]$$

$$=\frac{1}{2}\left[\delta_{jk}-\delta_{jk}+\frac{\partial u_j}{\partial x_k}+\frac{\partial u_k}{\partial x_j}-\frac{\partial u_i}{\partial x_j}\frac{\partial u_i}{\partial x_k}\right]$$

$$=\frac{1}{2}\left[\frac{\partial u_j}{\partial x_k}+\frac{\partial u_k}{\partial x_j}-\frac{\partial u_i}{\partial x_j}\frac{\partial u_i}{\partial x_k}\right]. \tag{4.18}$$

In the case of small deformation, $\partial u_i/\partial x_j$ is small and the last term in the above expression for E_{jk} can be neglected, resulting in

$$\varepsilon_{jk} = \frac{1}{2}\left[\frac{\partial u_i}{\partial x_k} + \frac{\partial u_k}{\partial x_j}\right]. \tag{4.19}$$

This is the Eulerian strain tensor for small deformations. The various strain components are related by the compatibility equations. Strains that are physically possible must always satisfy these equations.

4.8 Compatibility Equation

The strain-displacement equation (4.19) can be written as

$$\varepsilon_{ij} = \frac{1}{2}(u_{i,j} + u_{j,i})$$

where

$$u_{i,j} = \frac{\partial u_i}{\partial x_j}.$$

Note (4.19) represents nine equations for ε_{ij}, of which six are independent. Since there are six independent equations with three unknowns (u_1, u_2, u_3), equations (4.19) form an overdetermined system. This implies that some relationship between the strain tensor components, ε_{ij}, must exist to be compatible with (4.19). This relationship is known as the compatibility equation and it can be found by eliminating u_i from the strain-displacement equations. To this end, the following terms are added:

$$\varepsilon_{ij,km} = \frac{1}{2}(u_{i,jkm} + u_{j,ikm}),$$

$$\varepsilon_{km,ij} = \frac{1}{2}(u_{k,mij} + u_{m,kij}),$$

$$-\varepsilon_{ik,jm} = \frac{1}{2}(u_{i,kjm} + u_{k,ijm}),$$

$$-\varepsilon_{jm,ik} = \frac{1}{2}(u_{j,mik} + u_{m,jik}).$$

The result is:

$$\varepsilon_{ij,km} + \varepsilon_{km,ij} - \varepsilon_{ik,jm} - \varepsilon_{jm,ik} = 0. \qquad (4.20)$$

This is the compatibility equation. It has 81 components (each index runs from 1 to 3), but only six of them are independent. To get the independent equations, let $m=k$ so that:

$$\varepsilon_{ij,kk} + \varepsilon_{kk,ij} - \varepsilon_{ik,jk} - \varepsilon_{jk,ik} = 0. \quad (4.21)$$

4.9 Hooke's Law for Isotropic Media

The compatibility equations provide the relations between the various strain components, while Hooke's Law supplies the relations between stress and strain components. For a material that is assumed to be one-dimensional, such as a thin rod, Hooke's law states that: *the applied stress is directly proportional to the resulting strain*. The proportionality constant is a material property. This law emerged as a result of experimental evidence [13]. A brief discussion for the case of isotropic materials is treated on the following page.

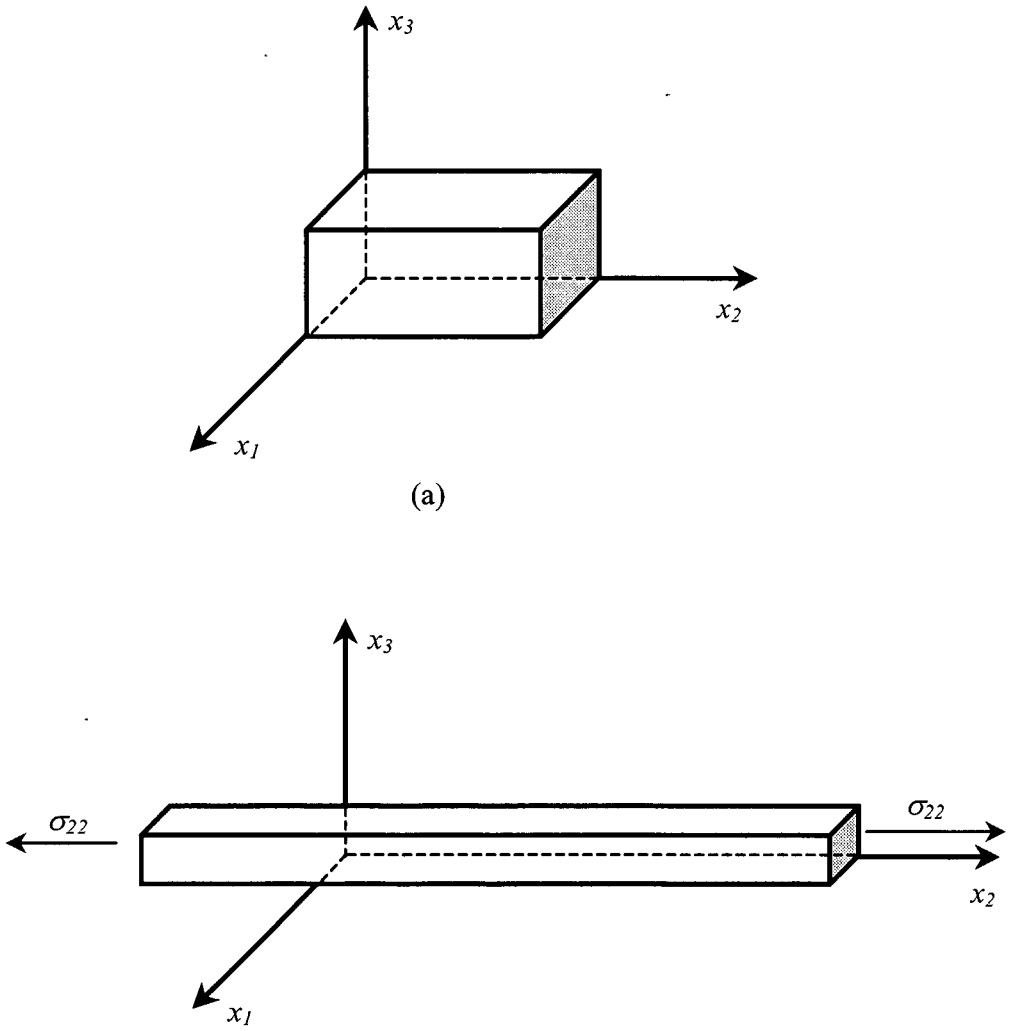

Figure 4.8: (a) Initial block. (b) Block after a stress σ_{11} is applied.

Figure 4.8 shows a rectangular material, with sides that are parallel to the various axes. Experiments show that if such a material is subjected to a normal stress in the x_1-direction (σ_{11}), that is uniformly distributed over two opposite sides, then in the case of an isotropic material, the element will experience no change in its angles but a change in length. Furthermore, the amount by which the length increases is given by,

$$\varepsilon_{11} = \frac{\sigma_{11}}{E}, \tag{4.22}$$

where E is the modulus of elasticity. The extension of the element in the x_1-direction is accampanied by the following lateral contractions:

$$\varepsilon_{22} = -\nu \frac{\sigma_{22}}{E}, \tag{4.23}$$

$$\varepsilon_{33} = -\nu \frac{\sigma_{33}}{E}, \tag{4.24}$$

where ν is a constant known as the poisson ratio (it is a material property). The modulus of elasticity and poisson's ratio are the same during compresion and tension, in the elastic limit.

According to experimental evidence, the total strain producing a stress σ_{11} when it is uniformly applied, is given by a superposition of equations (4.22), (4.23) and (4.24), in which the sum of all strain components is zero. This yields:

$$\varepsilon_{11} = \frac{1}{E}(\sigma_{11} - \nu\sigma_{22} - \nu\sigma_{33}). \tag{4.25}$$

If this rectangular element were subjected to normal stresses σ_{22} and σ_{33}, under similar conditions to those discussed above, the resulting strain components would be

$$\varepsilon_{22} = \frac{1}{E}(\sigma_{22} - \nu\sigma_{11} - \nu\sigma_{33}), \tag{4.26}$$

and

$$\varepsilon_{33} = \frac{1}{E}(\sigma_{33} - \nu\sigma_{22} - \nu\sigma_{11}). \tag{4.27}$$

The shearing stains resulting from shearing stresses are given by:

$$\varepsilon_{12} = \frac{1+\nu}{E}\sigma_{12}, \tag{4.28}$$

$$\varepsilon_{13} = \frac{1+\nu}{E}\sigma_{13}, \tag{4.29}$$

and

$$\varepsilon_{23} = \frac{1+\nu}{E}\sigma_{23}. \tag{4.30}$$

Equations (4.25) to (4.30) are known as Hooke's law for isotropic materials. The effect of temperature on the relationship between stress and strain is of particular interest in this study. This concern is dealt with in the forthcoming section, with reference to Hooke's law.

4.10 Thermal Stress

Thermal stresses result from an unequal heating of the various parts of an elastic continuous solid. These stresses would not be present if each element of the solid were allowed to expand freely. The continuity of the material prevents free expansion and this results in thermal stresses. If the temperature of an elastic isotropic body increases by ΔT, some temperature-induced strains will develop. Since the body is isotropic, all infinitesimal line elements undergo equal expansions. Therefore, if α is the coefficient of linear thermal expansion, the strain components due to the temperature change are:

$$\varepsilon_{11} = \varepsilon_{22} = \varepsilon_{33} = \alpha(\Delta T) \tag{4.31}$$

and

$$\varepsilon_{12} = \varepsilon_{13} = \varepsilon_{23} = 0 \tag{4.32}$$

The thermally induced strains can be added to the stress induced strains, as given by Hook's law for an isotropic medium (in the previous section), yielding:

$$\varepsilon_{11} = \frac{1}{E}(\sigma_{11} - \nu\sigma_{22} - \nu\sigma_{33}) + \alpha(\Delta T), \tag{4.33}$$

$$\varepsilon_{22} = \frac{1}{E}(\sigma_{22} - \nu\sigma_{11} - \nu\sigma_{33}) + \alpha(\Delta T), \tag{4.34}$$

$$\varepsilon_{33} = \frac{1}{E}(\sigma_{33} - \nu\sigma_{11} - \nu\sigma_{22}) + \alpha(\Delta T), \tag{4.35}$$

$$\varepsilon_{12} = \frac{1+\nu}{E}\sigma_{12} \tag{4.36},$$

$$\varepsilon_{13} = \frac{1+\nu}{E}\sigma_{13} \tag{4.37}$$

and

$$\varepsilon_{23} = \frac{1+\nu}{E}\sigma_{23} \tag{4.38}$$

This set of equations can also be written in index notation as follows:

$$\varepsilon_{ij} = \frac{1}{E}[(1+\nu)\sigma_{ij} - \nu\delta_{ij}\sigma_{kk}] + \alpha\delta_{ij}(\Delta T). \tag{4.39}$$

In a cylindrical system of coordinates, the subscripts r, θ, z are substituted for 1, 2, and 3, respectively [14].

4.11 Equilibrium Conditions in Polar Coordinates

In section 4.5, the equilibrium conditions for the interior of a continuum were derived in cartesian coordinates. These equations, however, are difficult to use when applied to a material whose shape is more conveniently specified in a different coordinate system (such as cylindrical or spherical coordinates). It is more advantageous to have the equilibrium conditions expressed in the same coordinate system as the material that is being investigated.

This section will treat the derivation of equilibrium conditions for a cylindrical material that is infinitely long, with a negligible z-dependence. Once again, this will be achieved by considering the equilibrium of a small element.

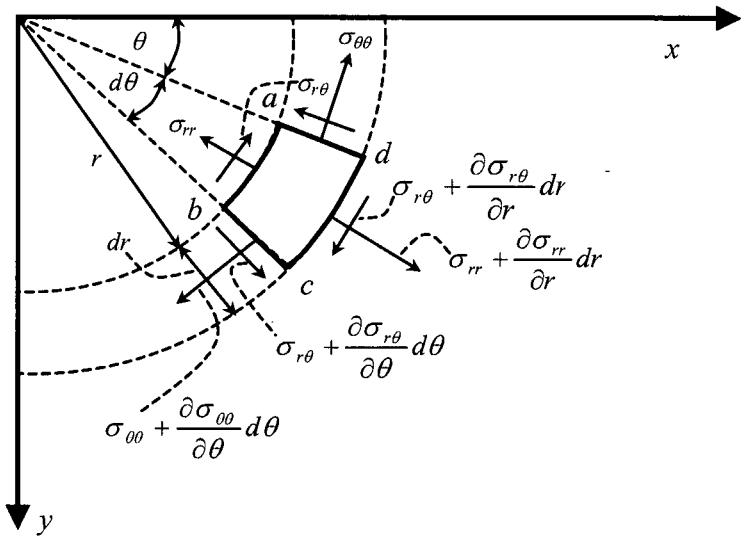

Figure 4.9: Top view of a circular cylindrical element that has an infinite length in the z-direction [13].

The above diagram (figure 4.9) shows an element of a horizontal slice through the infinitely long cylinder, with all the possible stresses. The sum of all the forces, due to each stress, in each direction (i.e. the r, and θ-directions) must add up to zero, in order for the element to be in equilibrium.

The imaginary line that intersects the origin and that is at an angle of $\theta + 1/2d\theta$ to the x-axis is taken to be in the radial direction. The θ-direction is taken to be perpendicular to the radial direction.

The element in figure 4.9 is considered to be infinitesimal. Its area will therefore be approximated by multiplying the length of side ab with the width dr. By virtue of the elements' infinitesimal nature, the following approximations will also be made:

$$\sin\left(\frac{1}{2}d\theta\right) \approx d\theta$$

and (4.40)

$$\cos\left(\frac{1}{2}d\theta\right) \approx 1.$$

The length of sides ab and cd (in figure 4.9) will be determined by using the following diagram and formula:

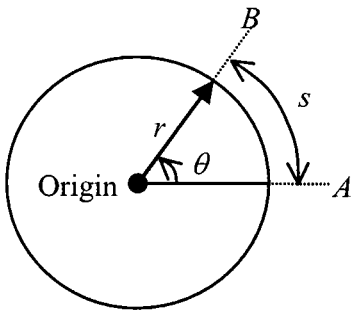

The arc length s = (radius of arc) × (angle in radians)
or
$s=r\theta$

Figure 4.10: The relationship between the radius, arc length and subtended angle of a circle.

Referring to figure 4.9, assume that the stresses on the sides of the element are uniformly distributed. All the forces on the element, for each direction, will now be added. As mentioned before, the force is given by the stress multiplied by the area of the face upon which it acts.

Radial Direction

By using figures 4.9 and 4.10, the addition of all the forces in the radial direction is:

$$\left(\sigma_{rr}+\frac{\partial\sigma_{rr}}{\partial r}dr\right)(r+dr)d\theta-\sigma_{rr}rd\theta+\left(\sigma_{r\theta}+\frac{\partial\sigma_{r\theta}}{\partial\theta}d\theta\right)dr\cos\left(\frac{1}{2}d\theta\right)$$

$$-\sigma_{r\theta}dr\cos\left(\frac{1}{2}d\theta\right)-\left(\sigma_{\theta\theta}+\frac{\partial\sigma_{\theta\theta}}{\partial\theta}d\theta\right)dr\sin\left(\frac{1}{2}d\theta\right)-\sigma_{\theta\theta}dr\sin\left(\frac{1}{2}d\theta\right)=0$$

According to the formula in figure 4.10, sides *ab* and *cd* have lengths $rd\theta$ and $(r+dr)d\theta$, respectively.

After using approximation (4.40) and adding all the terms, this expression reduces to:

$$\frac{\partial \sigma_{rr}}{\partial r} + \frac{1}{r}\frac{\partial \sigma_{r\theta}}{\partial \theta} + \frac{\sigma_{rr} - \sigma_{\theta\theta}}{r} = 0. \tag{4.41}$$

θ-Direction

The addition of all the forces in the θ-direction (see figure 3.7) is given by:

$$\left(\sigma_{r\theta} + \frac{\partial \sigma_{r\theta}}{\partial r} dr\right)(r + dr)d\theta - \sigma_{r\theta} r d\theta + \left(\sigma_{\theta\theta} + \frac{\partial \sigma_{\theta\theta}}{\partial \theta} d\theta\right) dr \cos\left(\frac{1}{2} d\theta\right)$$

$$- \sigma_{\theta\theta} dr \cos\left(\frac{1}{2} d\theta\right) + \left(\sigma_{r\theta} + \frac{\partial \sigma_{r\theta}}{\partial \theta} d\theta\right) dr \sin\left(\frac{1}{2} d\theta\right) + \sigma_{r\theta} dr \sin\left(\frac{1}{2} d\theta\right) = 0.$$

This expression can be reduced to:

$$\frac{1}{r}\frac{\partial \sigma_{\theta\theta}}{\partial \theta} + \frac{\partial \sigma_{r\theta}}{\partial r} + \frac{2\sigma_{r\theta}}{r} = 0. \tag{4.42}$$

Therefore, the equilibrium conditions for a circular-cylindrical material of infinite length are:

$$\frac{\partial \sigma_{rr}}{\partial r} + \frac{1}{r}\frac{\partial \sigma_{r\theta}}{\partial \theta} + \frac{\sigma_{rr} - \sigma_{\theta\theta}}{r} = 0, \tag{4.41}$$

$$\frac{1}{r}\frac{\partial \sigma_{\theta\theta}}{\partial \theta} + \frac{\partial \sigma_{r\theta}}{\partial r} + \frac{2\sigma_{r\theta}}{r} = 0. \tag{4.42}$$

4.12 Equations of Strain in Polar Coordinates

A derivation of equations relating strain components to displacements, in polar coordinates, is dealt with in this section. A different approach (from section 4.7, which treats this derivation in cartesian coordinates) will be used.

Let u_r and u_θ denote displacements in the r and θ directions, respectively. Surface *ABCD*, in figure 4.11, represents the top-view of a cylindrical element (like the element shown in figure 4.9). The sides *AD* and *BC* are circular arcs, but since the element is assumed to be infinitesimal, these sides can be considered as straight lines.

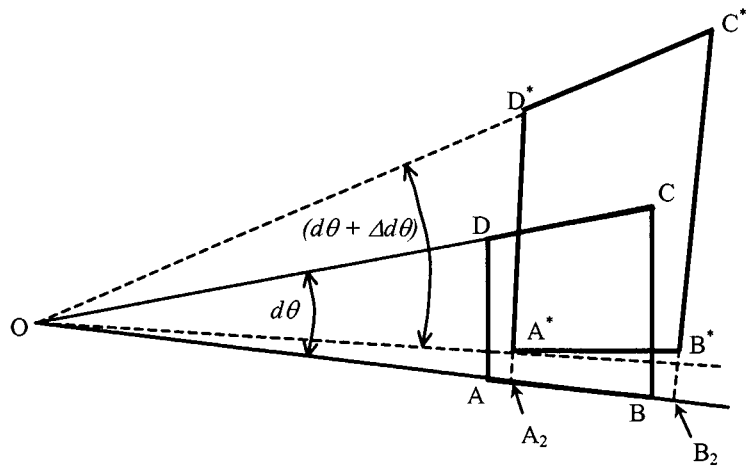

Figure 4.11: Top view of a circular cylindrical element that experiences deformation [15].

Suppose that element *ABCD* is deformed in such a way that points *A*, *B*, *C* and *D* move to new locations at: A^*, B^*, C^* and D^*. Assume that the deformation causes the sides and angles of the original element to change in size. The angle $d\theta$ becomes $d\theta+\Delta d\theta$ after straining.

Consider the strain experienced by the line *AB*. The distance A^*B^* can be transferred to the line *AB* by drawing arcs (with center *O*) through A^* and B^* to meet the line *OAB* at A_2 and B_2. Since

$$A_2B_2 = dr + \frac{\partial u_r}{\partial r} dr \tag{4.43}$$

and

$$AB = dr, \tag{4.44}$$

it follows that the radial strain is

$$\varepsilon_{rr} = \frac{A_2B_2 - AB}{AB} = \frac{1}{dr}\left(dr + \frac{\partial u_r}{\partial r} dr - dr \right) = \frac{\partial u_r}{\partial r}. \tag{4.45}$$

The tangential strain is defined as

$$\varepsilon_{\theta\theta} = \frac{A^*D^* - AD}{AD}. \tag{4.46}$$

Since $d\theta$ is very small,

$$\sin(d\theta) \approx d\theta = \frac{AD}{r}, \tag{4.47}$$

and

$$AD = rd\theta. \tag{4.48}$$

The angle subtended by A^*D^* is increased by (increased from the angle subtended by AD),

$$\Delta d\theta = \frac{du_\theta}{r+u_r} \approx \frac{1}{r}\frac{\partial u_\theta}{\partial \theta} d\theta . \tag{4.49}$$

Once again, the approximation,

$$\sin(\Delta d\theta) \approx \Delta d\theta ,$$

has been used. By using equations (4.46), (4.49), and the geometrical property shown in equation (4.47), the following can be written:

$$A^* B^* = (r+u_r)\left(d\theta + \frac{1}{r}\frac{\partial u_\theta}{\partial \theta} d\theta \right). \tag{4.50}$$

Therefore, according to equations (4.46), (4.48) and (4.50),

$$\varepsilon_{\theta\theta} = \frac{\left(rd\theta + \frac{\partial u_\theta}{\partial \theta} d\theta \right) + u_r d\theta + \frac{u_r}{r} d\theta \frac{\partial u_\theta}{\partial \theta} - rd\theta}{rd\theta},$$

and after neglecting second order terms,

$$\varepsilon_{\theta\theta} = \frac{u_r}{r} + \frac{1}{r}\frac{\partial u_\theta}{\partial \theta}. \tag{4.51}$$

The theory introduced in this chapter will be applied to a long cylinder in the following chapter.

Chapter 5

Long Cylinder Stress Model

5.1 Introduction

As mentioned in the latter part of section 1.3 of chapter 1, the development of thermal stress in a steel coil (during batch annealing) has an affect on the formation of diffusion welds between spirals. It is reasonable to assume that the inter-diffusion between spirals can only occur when contact is established. Since compressive radial stress will cause firmer contact between spirals, it is hypothesized here that diffusion welds occur in regions of high compressive radial stress. Also, since diffusion occurs at a faster rate at higher temperatures than at lower temperatures, it is also reasonable to assume that diffusion welds will rather occur in a region where high compressive radial stress is accompanied by high temperature in that region. An analytical study of thermal stress is presented in this chapter, with this assumption in mind.

This chapter begins with the formulation of a long cylinder model for thermal stress. An analytical temperature distribution is incorporated after that. Sections 5.4 and 5.5 show some thermal stress results for constant heating and cooling. The steady state solutions that appear in section 5.6 lead to a suggestion of reducing compressive radial stress during cooling. This suggestion is later applied to a linear cooling temperature ramp in section 5.7.

5.2 Formulation of Model

Consider a sufficiently long axially symmetric solid cylinder, with a concentric hole, such that the temperature and stress contributions from both the top and bottom are negligible. The thermal stress in such a system depends only on the radial distance r and time t. As a result, it can be considered as a problem of plane strain, with a single plane slice describing the stress of the entire cylinder (refer to figure 5.1). In other words, the stress distribution in each plain slice that does not "feel" the effect of the top and bottom edges is the same, regardless of its height.

The stress distribution in a plane slice will be obtained analytically by making use of a stress function ϕ that solves the equilibrium condition (4.41) at any time (this is for axial symmetry, therefore, the term containing $\sigma_{r\theta}$ vanishes). This function will be used to generate expressions for σ_{rr} and $\sigma_{\theta\theta}$ in terms of a temperature distribution [14].

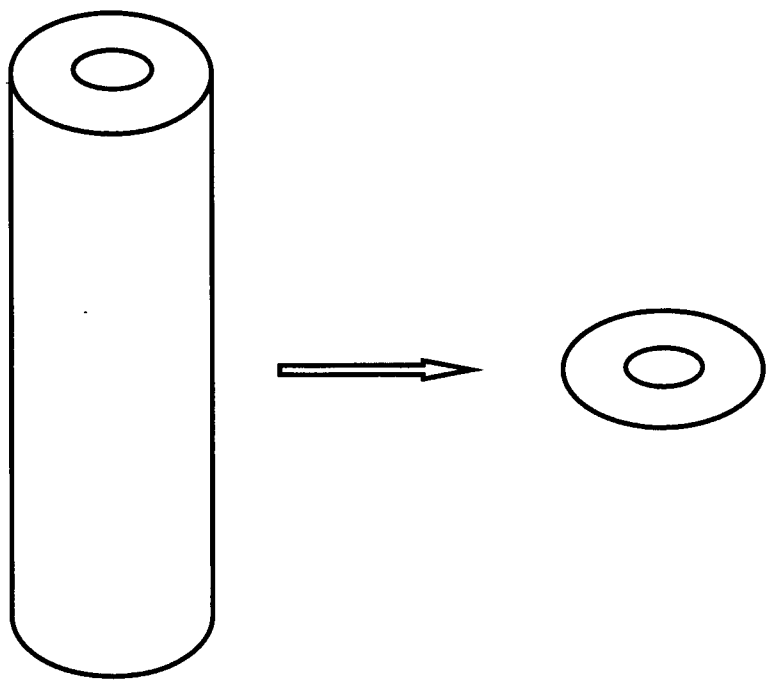

Figure 5.1: An illustration of a plane slice from a long cylinder.

Assume that no deformation occurs in the z-direction. This assumption requires that $\varepsilon_{zz}=0$. Consequently, equation (4.35) becomes:

$$\sigma_{zz} = \nu(\sigma_{rr} + \sigma_{\theta\theta}) - \alpha E \Delta T \,. \tag{5.1}$$

When the above result is substituted into equations (4.33) and (4.34), the following expressions emerge, respectively:

$$\varepsilon_{rr} = \frac{1+\nu}{E}\left[(1-\nu)\sigma_{rr} - \nu\sigma_{\theta\theta} + \alpha E \Delta T\right] \tag{5.2}$$

and

$$\varepsilon_{\theta\theta} = \frac{1+\nu}{E}\left[(1-\nu)\sigma_{\theta\theta} - \nu\sigma_{rr} + \alpha E \Delta T\right]. \tag{5.3}$$

According to equations (4.45) and (4.51),

$$\varepsilon_{rr} = \frac{\partial u}{\partial r}$$

and

$$\varepsilon_{\theta\theta} = \frac{u}{r}.$$

When u is eliminated from (4.45) and (4.51), the following compatability equation results,

$$\frac{d}{dr}(r\varepsilon_{\theta\theta}) - \varepsilon_{rr} = 0\,. \tag{5.4}$$

A stress function ϕ that satisfies the equilibrium condition (4.41) can be defined as follows:

$$\sigma_{rr} = \frac{\phi}{r} \tag{5.5}$$

and

$$\sigma_{\theta\theta} = \frac{d\phi}{dr}. \tag{5.6}$$

After substituting (5.2), (5.3), (5.5) and (5.6) into (5.4), the following differential equation is obtained:

$$\frac{d}{dr}\left(r\left[(1-\nu)\frac{d\phi}{dr} - \nu\frac{\phi}{r}\right]\right) - (1-\nu)\frac{\phi}{r} + \nu\frac{d\phi}{dr} + \alpha E r\frac{d(\Delta T)}{dr} = 0.$$

This expression can be simplified by writing out the derivative of the bracketed terms,

$$(1-\nu)\frac{d\phi}{dr} + r(1-\nu)\frac{d^2\phi}{dr^2} - \nu\frac{d\phi}{dr} - (1-\nu)\frac{\phi}{r} + \nu\frac{d\phi}{dr} = -\alpha E r\frac{d(\Delta T)}{dr},$$

and gathering like terms in order to arrive at:

$$\frac{1}{r}\frac{d\phi}{dr} + \frac{d^2\phi}{dr^2} - \frac{\phi}{r^2} = -\frac{\alpha E}{(1-\nu)}\frac{d(\Delta T)}{dr},$$

which can also be written as,

$$\frac{d}{dr}\left[\frac{1}{r}\frac{d}{dr}(r\phi)\right] = -\frac{\alpha E}{(1-\nu)}\frac{d(\Delta T)}{dr}. \tag{5.7}$$

An explicit expression for ϕ can be found by integrating equation (5.7) twice, with respect to r, thus yielding:

$$\phi = -\frac{\alpha E}{(1-\nu)}\frac{1}{r}\int_a^r (\Delta T) r dr + \frac{C_1 r}{2} + \frac{C_2}{r}. \tag{5.8}$$

Therefore,

$$\sigma_{rr} = \frac{\phi}{r} = -\frac{\alpha E}{(1-\nu)}\frac{1}{r^2}\int_a^r (\Delta T) r dr + \frac{C_1}{2} + \frac{C_2}{r^2}, \tag{5.9}$$

according to definition (5.5) and equation (5.8). The limits of integration are from a to r because the cylinder has an inner radius of a. The integration constants C_1 and C_2 can be obtained from the boundary conditions. Since the surface at both the inner and outer radii are free, with no external force acting on them, $\sigma_{rr} = 0$ at $r = a$ and $r = b$ throughout the heating process. As a result,

$$0 = -\frac{\alpha E}{(1-\nu)}\frac{1}{a^2}\int_a^a (\Delta T) r dr + \frac{C_1}{2} + \frac{C_2}{a^2}$$

and

$$0 = -\frac{\alpha E}{(1-\nu)}\frac{1}{b^2}\int_a^b (\Delta T) r dr + \frac{C_1}{2} + \frac{C_2}{b^2}.$$

Consequently,

$$\begin{bmatrix} \frac{1}{2} & \frac{1}{a^2} \\ \frac{1}{2} & \frac{1}{b^2} \end{bmatrix} \begin{bmatrix} C_1 \\ C_2 \end{bmatrix} = \begin{bmatrix} \frac{\alpha E}{(1-\nu)}\frac{1}{a^2}\int_a^a (\Delta T) r dr \\ \frac{\alpha E}{(1-\nu)}\frac{1}{b^2}\int_a^b (\Delta T) r dr \end{bmatrix},$$

and

$$\begin{bmatrix} C_1 \\ C_2 \end{bmatrix} = \left(\frac{2a^2b^2}{a^2 - b^2} \right) \begin{bmatrix} \frac{1}{b^2} & -\frac{1}{a^2} \\ -\frac{1}{2} & \frac{1}{2} \end{bmatrix} \begin{bmatrix} \frac{\alpha E}{(1-\nu)} \frac{1}{a^2} \int_a^a (\Delta T) r dr \\ \frac{\alpha E}{(1-\nu)} \frac{1}{b^2} \int_a^b (\Delta T) r dr \end{bmatrix}.$$

Therefore,

$$C_1 = \frac{2\alpha E}{(1-\nu)} \frac{1}{(b^2 - a^2)} \int_a^b (\Delta T) r dr,$$

$$C_2 = -\frac{\alpha E}{(1-\nu)} \frac{a^2}{(b^2 - a^2)} \int_a^b (\Delta T) r dr,$$

and

$$\sigma_{rr} = -\frac{\alpha E}{(1-\nu)} \left[\frac{1}{r^2} \int_a^r (\Delta T) r dr + \frac{1}{(b^2 - a^2)} \int_a^b (\Delta T) r dr - \frac{a^2}{(b^2 - a^2)} \frac{1}{r^2} \int_a^b (\Delta T) r dr \right].$$

This relation can also be written as:

$$\sigma_{rr} = \frac{\alpha E}{(1-\nu)} \frac{1}{r^2} \left[\left(\frac{r^2 - a^2}{b^2 - a^2} \right) \int_a^b (\Delta T) r dr - \int_a^r (\Delta T) r dr \right]. \qquad (5.10)$$

The hoop stress $\sigma_{\theta\theta}$ is given by,

$$\sigma_{\theta\theta} = \frac{d\phi}{dr} = \frac{\alpha E}{(1-\nu)}\frac{d}{dr}\left[-\frac{1}{r}\int_a^r (\Delta T) r dr + \frac{r}{(b^2-a^2)}\int_a^b (\Delta T) r dr - \frac{a^2}{(b^2-a^2)}\frac{1}{r}\int_a^b (\Delta T) r dr\right]$$

$$= \frac{\alpha E}{(1-\nu)}\left[\frac{1}{r^2}\int_a^r (\Delta T) r dr - \Delta T + \frac{1}{(b^2-a^2)}\int_a^b (\Delta T) r dr + \frac{a^2}{(b^2-a^2)}\frac{1}{r^2}\int_a^b (\Delta T) r dr\right]$$

In a similar manner as before, this equation can be stated as,

$$\sigma_{\theta\theta} = \frac{\alpha E}{(1-\nu)}\frac{1}{r^2}\left[\left(\frac{r^2+a^2}{b^2-a^2}\right)\int_a^b (\Delta T) r dr + \int_a^r (\Delta T) r dr - \Delta T r^2\right]. \qquad (5.11)$$

From equations (5.1), (5.10) and (5.11), it follows that σ_{zz} must be given by,

$$\sigma_{zz} = \frac{\alpha E}{(1-\nu)}\left[\left(\frac{2\nu}{b^2-a^2}\right)\int_a^b (\Delta T) r dr - \Delta T\right], \qquad (5.12)$$

in order for ε_{zz} to be zero.

Equations (5.10) to (5.12) can only be of use once the temperature distribution T is known. An incorporation of an analytical expression for T follows in the ensuing section.

5.3 Incorporation of an Analytical Temperature Distribution

The heat equation (2.2), in the case of radial and time dependence only, is

$$\kappa_r \frac{1}{r}\frac{\partial T}{\partial r} + \kappa_r \frac{\partial^2 T}{\partial r^2} = \frac{\partial T}{\partial t}. \qquad (5.13)$$

The solution of (5.13) is,

$$\Delta T(r,t) = \sum_{k=1}^{\infty} A_k \left[J_0(\alpha_k r) + b_k Y_0(\alpha_k r) \right] \exp(-\alpha_k{}^2 \kappa_r t), \qquad (5.14)$$

as shown in section 2.8. The following integrals have been evaluated, in order to apply (5.14) to (5.10), (5.11) and (5.12) [9]:

$$\int_{\sigma}^{1} (\Delta T) r dr = \int_{\sigma}^{1} \left[J_0(\alpha_k r) + b_k Y_0(\alpha_k r) \right] r dr$$

$$= \frac{1}{\alpha_k} \left[(J_1(\alpha_k) + b_k Y_1(\alpha_k)) - \sigma (J_1(\alpha_k \sigma) + b_k Y_1(\alpha_k \sigma)) \right]$$

and

$$\int_{\sigma}^{r} (\Delta T) r dr = \int_{\sigma}^{r} \left[J_0(\alpha_k r) + b_k Y_0(\alpha_k r) \right] r dr$$

$$= \frac{1}{\alpha_k} \left[(J_1(\alpha_k r) + b_k Y_1(\alpha_k r)) r - \sigma (J_1(\alpha_k \sigma) + b_k Y_1(\alpha_k \sigma)) \right]$$

Thus, equations (5.15), (5.16) and (5.17) are given by

$$\sigma_{rr} = \frac{\alpha E}{(1-\nu)} \frac{1}{r^2} \sum_{k=1}^{\infty} \frac{A_k}{\alpha_k} \left[\begin{array}{l} \left(\dfrac{r^2 - \sigma^2}{1 - \sigma^2} \right) \left\{ (J_1(\alpha_k) + b_k Y_1(\alpha_k)) - \sigma (J_1(\alpha_k \sigma) + b_k Y_1(\alpha_k \sigma)) \right\} \\ - \left\{ (J_1(\alpha_k r) + b_k Y_1(\alpha_k r)) r - \sigma (J_1(\alpha_k \sigma) + b_k Y_1(\alpha_k \sigma)) \right\} \end{array} \right] \exp(-\alpha_k{}^2 \kappa_r t),$$

$$\sigma_{\theta\theta} = \frac{\alpha E}{(1-\nu)} \frac{1}{r^2} \sum_{k=1}^{\infty} \frac{A_k}{\alpha_k} \left[\begin{array}{l} \left(\frac{r^2+\sigma^2}{1-\sigma^2} \right) \{(J_1(\alpha_k) + b_k Y_1(\alpha_k)) - \sigma(J_1(\alpha_k \sigma) + b_k Y_1(\alpha_k \sigma))\} \\ + \{(J_1(\alpha_k r) + b_k Y_1(\alpha_k r))r - \sigma(J_1(\alpha_k \sigma) + b_k Y_1(\alpha_k \sigma))\} \\ - \{(J_0(\alpha_k r) + b_k Y_0(\alpha_k r))\} r^2 \end{array} \right] \exp(-\alpha_k{}^2 \kappa_r t),$$

$$\sigma_{zz} = \frac{\alpha E}{(1-\nu)} \sum_{k=1}^{\infty} \frac{A_k}{\alpha_k} \left[\begin{array}{l} \left(\frac{2\nu}{1-\sigma^2} \right) \{(J_1(\alpha_k) + b_k Y_1(\alpha_k)) - \sigma(J_1(\alpha_k \sigma) + b_k Y_1(\alpha_k \sigma))\} \\ - \{(J_0(\alpha_k r) + b_k Y_0(\alpha_k r))\} r^2 \end{array} \right] \exp(-\alpha_k{}^2 \kappa_r t),$$

respectively, for a long cylinder with a concentric hole, subject to the initial and boundary conditions mentioned in section 2.8 for the radial direction (the results are later scaled to range from 0 to 670°C). These equations will be applied to a cylinder with inner and outer radii of 0.4 and 1m. The steel that comprises this cylinder is taken to have a thermal expansion coefficient of $\alpha = 12 \times 10^{-6}\ ^{\circ}C^{-1}$ and a modulus of elasticity with a value of $E = 20 \times 10^{10}\ N/m^2$ (at room temperature).

5.4 Constant Heating Results

The temperature and stress results, from equations (5.15) to (5.17), for a cylinder that is heated at 670°C on both the inner and outer edges are shown in figures 5.2, 5.3, 5.4 and 5.5. These results were obtained using the MATLAB program *astress.m*, which implements equations (5.15) to (5.17), see appendix E.2. Temperature and stress curves are shown at number of stages during the time evolution, each curve on a particular graph is taken at a different time. The curve numbers and corresponding times are listed in table 5.1. Curves 1 to 5 and 5 to 9 are shown on separate graphs, this type of display will be of particular use when discussing the various stress distributions. In the same manner as before, the interior of the cylinder is initially at 0°C.

Table 5.1: A table showing the time equivalence of each curve number.

Curve Number	Time (hours)
1	0
2	0.2
3	0.4
4	1
5	2
6	20
7	40
8	60
9	80

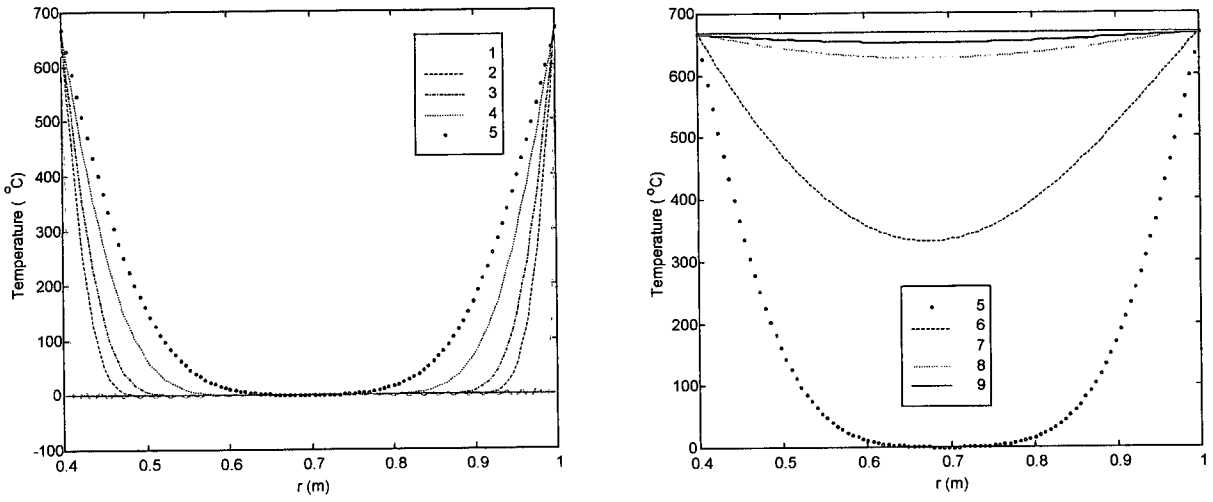

(a) (b)

Figure 5.2: (a) Temperature profiles from 0 to 2 hours. (b) Temperature profiles from 2 to 80 hours.

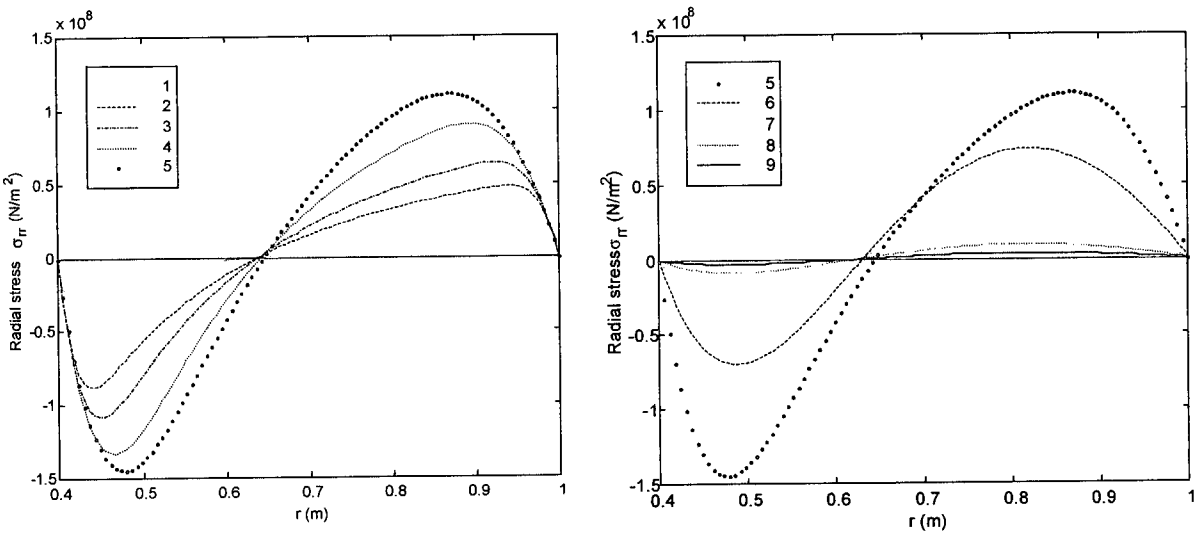

(a) (b)

Figure 5.3: (a) Radial stress profiles from 0 to 2 hours. (b) Radial stress profiles from 2 to 80 hours.

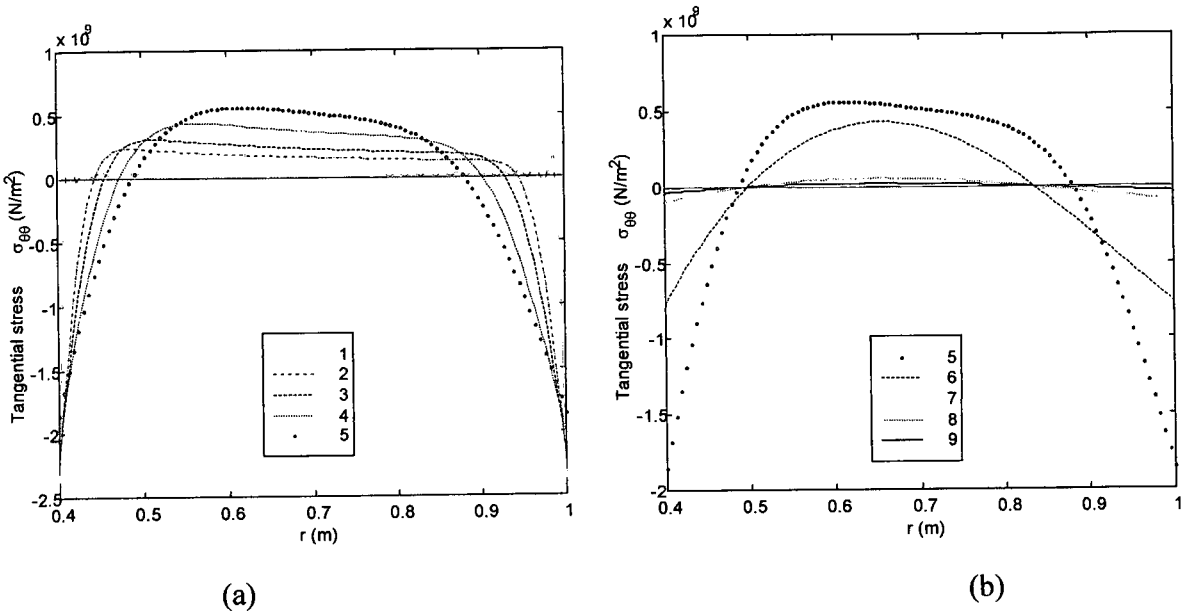

Figure 5.4: (a) Tangential stress profiles from 0 to 2 hours. (b) Tangential stress profiles from 2 to 80 hours.

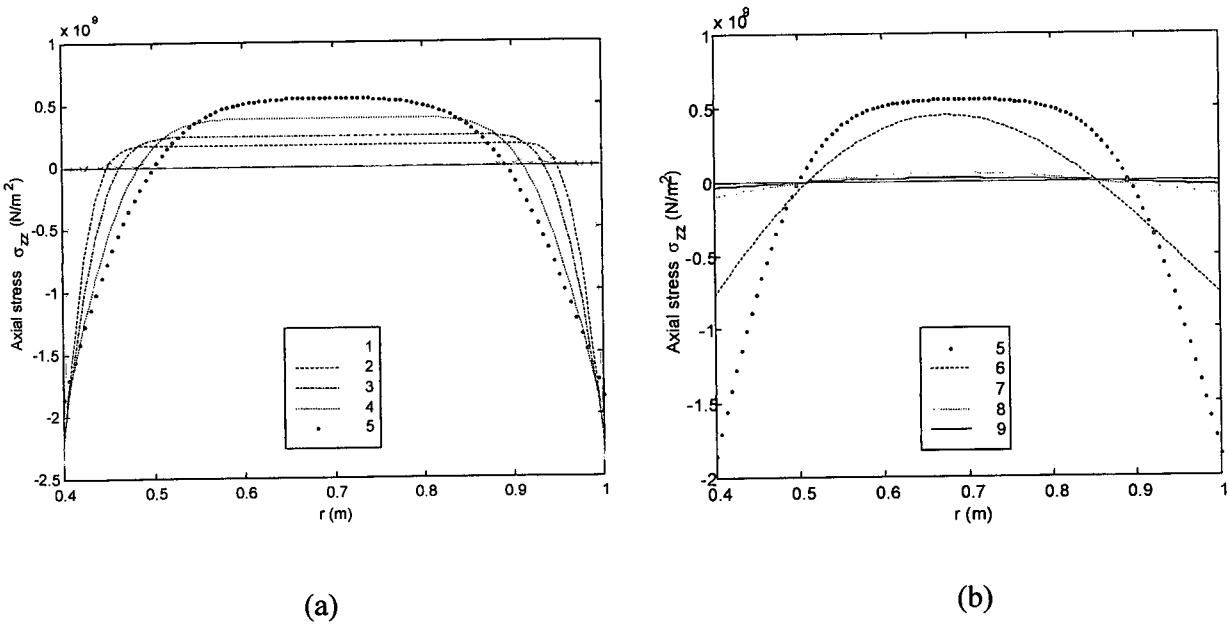

Figure 5.5: (a) Axial stress profiles from 0 to 2 hours. (b) Axial stress profiles from 2 to 80 hours.

In all of the stress diagrams (figures 5.3, 5.4 and 5.5), there is an increase in the magnitude of stress from 0 to approximately 2 hours and a subsequent decrease as time increases beyond 2 hours. Curves 1 to 5 show the increase and curves 5 to 9 show the decrease. When the steady state temperature is reached (which is 670°C throughout the material), the radial, axial and tangential stresses become zero. Since there is no temperature contribution from the z-direction, the cylinder takes much longer to reach steady state.

The radial stress is compressive near the inner edge and tensile towards the outer edge. This suggests that the spirals of a coil, that is subjected to the same conditions, would experience a force that pushes them together in the area of radial compression and one that pulls them apart, in the region of tensile stress. One can also gather from this that the thermal radial stresses would cause the inner and outer edges to moves outwards, towards a larger radius, if expansion were allowed.

There appears to be some similarity between the shape of the tangential and axial stresses, the main difference is in the anti-symmetry of the tangential stress. Both the inner and outer rings are subject to compressive stress during heating. As the heat spreads, some compression also develops in the vicinity of the inner and outer rings, while tensile stresses prevail in the center region. These stress profiles indicate that the inner and outer rings would become larger if expansion were allowed.

Similar arguments can also be used for the axial stress profile in the case where expansion is permitted. There would be a lengthening (in the *z*-direction) of the cylinder near the inner and outer edges, while the center would experience some shrinkage.

5.5 Constant Cooling Results

As a direct opposite of the constant heating case (section 5.4), the case of constant cooling deals with an imposition of 0°C on both the inner and outer edges, with an

interior that starts off at 670°C. Table 5.2 gives the times corresponding to the various curve numbers. The temperature and stress results appear in figures 5.6, 5.7, 5.8, and 5.9.

Table 5.2: A table showing the time equivalence of each curve number.

Curve Number	Time (hours)
10	0
11	0.2
12	0.4
13	1
14	2
15	20
16	40
17	60
18	80

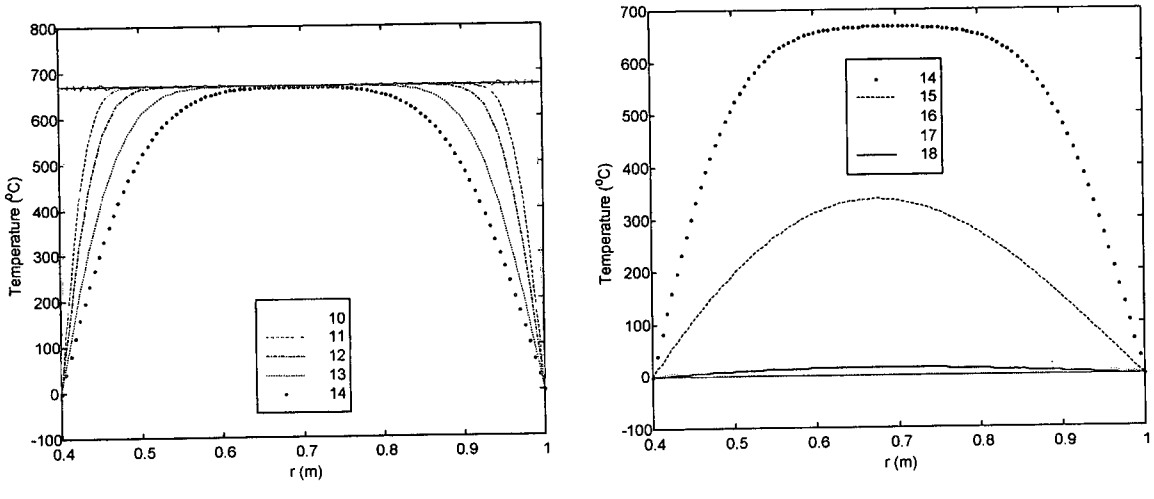

(a) (b)

Figure 5.6: (a) Temperature profiles from 0 to 2 hours. (b) Temperature profiles from 2 to 80 hours.

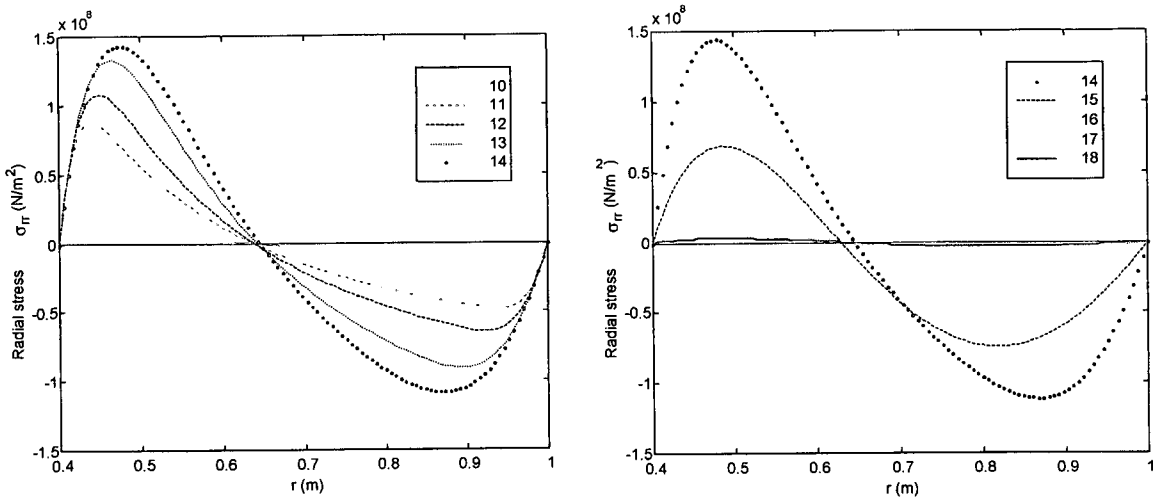

(a) (b)

Figure 5.7: (a) Radial stress profiles from 0 to 2 hours. (b) Radial stress profiles from 2 to 80 hours.

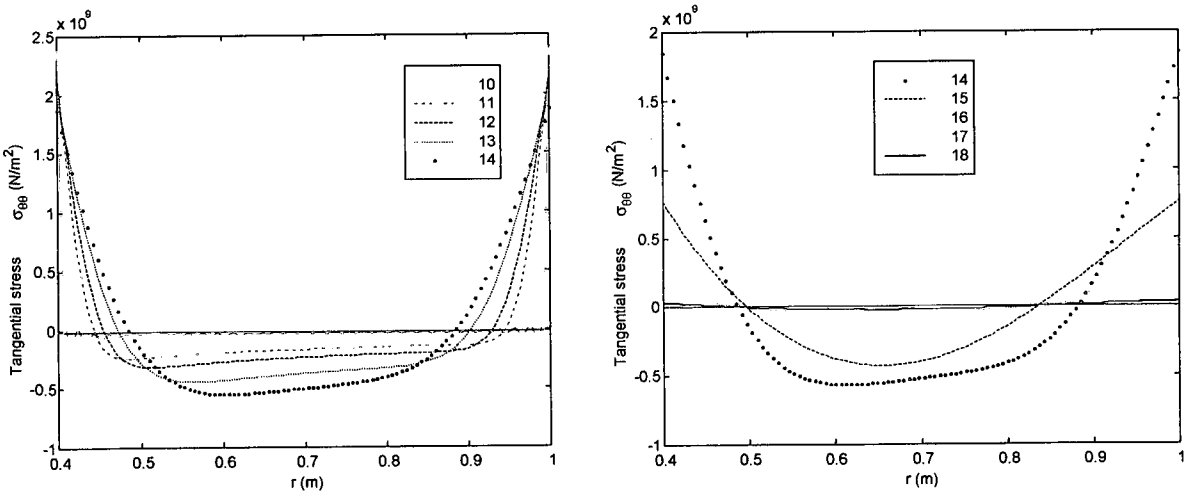

(a) (b)

Figure 5.8: (a) Tangential stress profiles from 0 to 2 hours. (b) Tangential stress profiles from 2 to 80 hours.

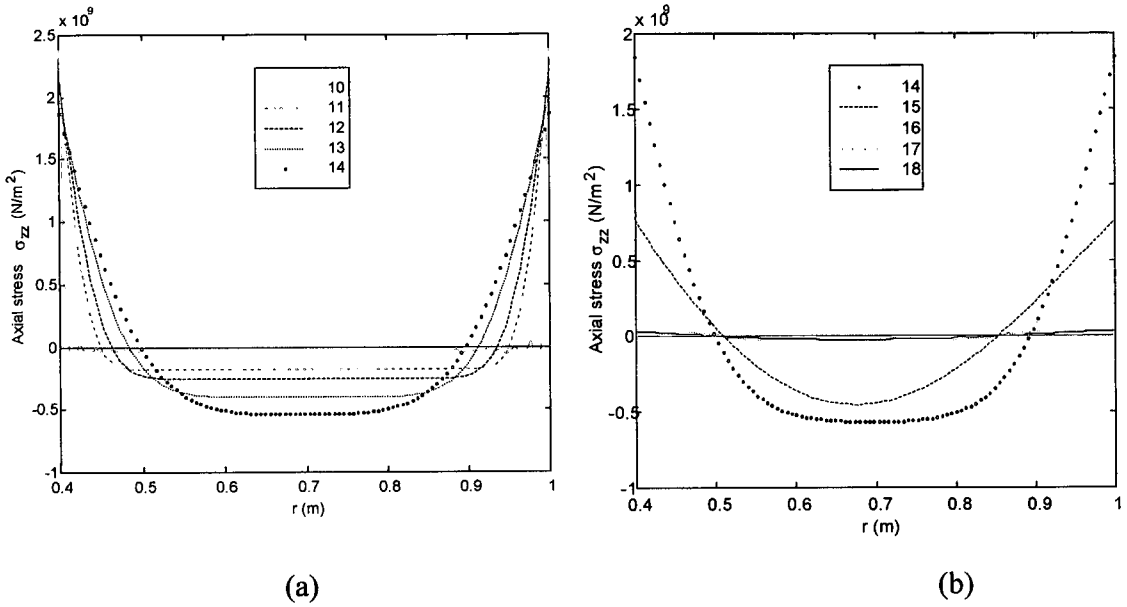

(a) (b)

Figure 5.9: (a) Axial stress profiles from 0 to 2 hours. (b) Axial stress profiles from 2 to 80 hours.

Figures 5.6, 5.7, 5.8, and 5.9 show results that are opposite to the case of constant heating (figures 5.2, 5.3, 5.4, and 5.5). As in the previous case, the radial, axial and tangential stresses increase from 0 to 2 hours and they decay to zero as the temperature distribution reaches steady state. Once again, similar reasoning can be applied, as far as the effect of the various stresses are concerned, when contraction is permitted.

Radial stresses play the most important role in strip adhesion. When there is a compressive radial stress, the gas flow between spirals (during the annealing process) is constricted and firmer contact is established between consecutive spirals. This, combined with high temperatures provide a conducive environment to inter-diffusion of atomic species between successive spirals. The exact temperature at which diffusion occurs depends largely on the properties of the material that comprise the coil. Despite this, it is safe to assume that there will be an increased chance of diffusion at higher temperatures for most materials.

During constant heating, maximum compression occurs at a radius of about 0.47m with a corresponding temperature of 185°C (see figures 5.2*a* and 5.3*b*). Constant cooling yields maximum compression at a radius of about 0.88m, with a corresponding temperature of 560°C (refer to figures 5.6*a* and 5.7*b*). It is therefore more likely that strip adhesion would take place during cooling, particularly during the beginning of the cooling process, near the outer ring of the coil. This finding concurs with the findings of Leroy and Bouquegneau [5].

Since the stress calculations of this model are for a long solid cylinder, the contribution of the coiling tension is neglected. It is expected that coiling tension in a coil would contribute to the compressive radial stress during the heating phase.

5.6 Steady State Solution

Two steady state temperature cases, that are later used to provide more insight to the radial thermal stress distributions during the cooling process, are discussed in this section. All the results are obtained analytically.

The heat equation for steady state and radial dependence is given by:

$$\frac{d^2T}{dr^2}+\frac{1}{r}\frac{dT}{dr}=0. \tag{5.18}$$

Let

$$P=\frac{dT}{dr}, \tag{5.19}$$

then (5.18) becomes,

$$\frac{dP}{dr}+\frac{1}{r}P=0.. \tag{5.20}$$

the solution of (5.20) is

$$P = \frac{D}{r}, \tag{5.21}$$

where D is an integration constant. When equations (5.19) and (5.21) are combined and subsequently solved, the following is obtained:

$$T(r) = D\log(r) + K,$$

where K is an integration constant. If a and b denote the inner and outer radii of the cylinder, respectively, then the boundary conditions are:

$$\begin{aligned} T(a) &= T_i \\ T(b) &= T_o \end{aligned} \tag{5.22}$$

T_i and T_o represent the temperatures of the inner and outer radii. The constants D and K are obtained from these conditions, in the manner shown below:

$$\begin{bmatrix} T_i \\ T_o \end{bmatrix} = \begin{bmatrix} \log(a) & 1 \\ \log(b) & 1 \end{bmatrix} \begin{bmatrix} D \\ K \end{bmatrix},$$

consequently,

$$\begin{bmatrix} D \\ K \end{bmatrix} = \frac{1}{\log\left(\frac{a}{b}\right)} \begin{bmatrix} 1 & -1 \\ -\log(b) & \log(a) \end{bmatrix} \begin{bmatrix} T_i \\ T_o \end{bmatrix}.$$

Therefore,

$$D = \frac{(T_i - T_o)}{\log\left(\frac{a}{b}\right)},$$

$$K = \frac{T_0 \log(a) - T_i \log(b)}{\log\left(\frac{a}{b}\right)},$$

and

$$T = \frac{(T_i - T_0)}{\log\left(\frac{a}{b}\right)}\log(r) + \frac{(T_0 \log(a) - T_i \log(b))}{\log\left(\frac{a}{b}\right)}. \tag{5.23}$$

Let

$$\Psi = \int_a^b Trdr = D\left[\left(\frac{b^2}{2}\log(b) - \frac{b^2}{4}\right) - \left(\frac{a^2}{2}\log(a) - \frac{a^2}{4}\right)\right] + K\left[\frac{b^2}{2} - \frac{a^2}{2}\right]$$

and

$$\Phi = \int_a^r Trdr = D\left[\left(\frac{r^2}{2}\log(b) - \frac{r^2}{4}\right) - \left(\frac{a^2}{2}\log(a) - \frac{a^2}{4}\right)\right] + K\left[\frac{r^2}{2} - \frac{a^2}{2}\right].$$

Then, according to equation (5.10),

$$\sigma_{rr} = \frac{\alpha E}{(1-\nu)}\frac{1}{r^2}\left[\left(\frac{r^2 - a^2}{b^2 - a^2}\right)\Psi - \Phi\right]. \tag{5.24}$$

If $T_i = 670°C$ and $T_0 = 470°C$, the following temperature and stress profiles (figures 10*a* and 10*b*) can be expected, according to equations (5.23) and (5.24). These curves were generated from the MATLAB program *streadystate.m*, in appendix E.3.

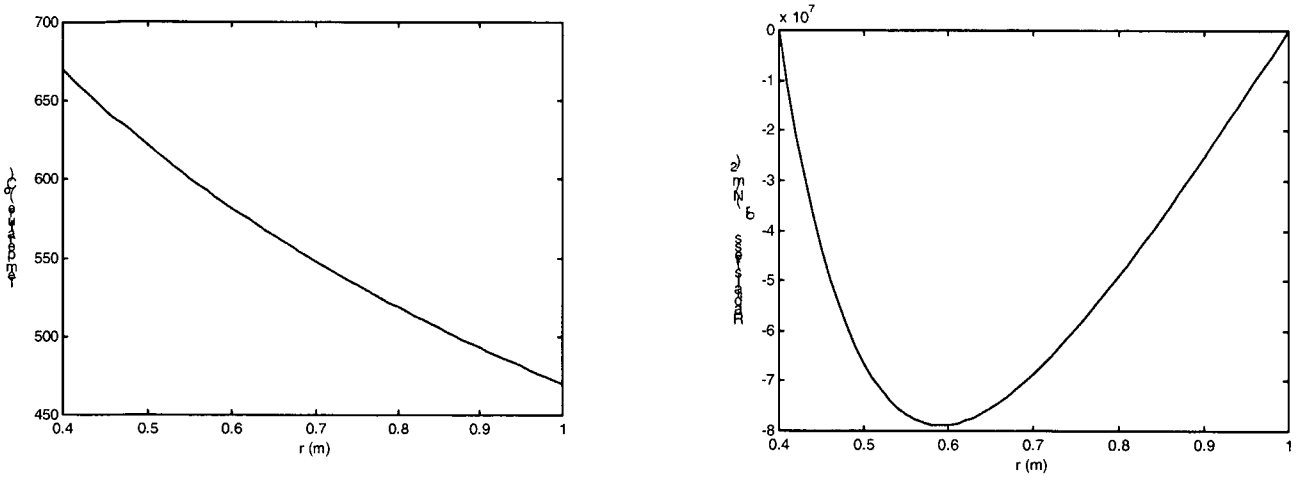

(a) (b)

Figure 5.10: (a) Steady state temperature. (b) A curve of the corresponding radial stress.

Figure 5.10 shows that the radial stress becomes compressive everywhere, when the inner ring is kept at a higher temperature than the outer ring. As discussed, in section 1.3, compressive radial stress aids in the formation of diffusion welds between coil spirals, during the cooling stage. From the graph shown in figure 5.10*b*, it is clear that strip adhesion would most likely occur throughout the interior of the coil, if the outer ring were cooled before the inner ring.

During a typical batch annealing process, the inner edge is at a lower temperature than the outer edge during heating and the opposite is true for cooling. This is because the outer edge experiences radiative heat transfer plus convective heat transfer from the circulating gas, while the inner edge mostly experiences convective heat transfer from the circulating gas (the temperature models of this thesis have not taken this into account).

According to figure 5.10*b*, this is very conducive to the development of compressive radial stress during cooling.

Conversely, if T_i = 470°C and T_o = 670°C (figure 11*a*), the opposite result can be expected. It can be seen, from figure 5.11*b*, that tensile radial stresses develop throughout the interior. This discourages strip adhesion and it consequently is the desired situation for the cooling stage. A suggestion, based on the above-mentioned observation, regarding the cooling stage of the temperature ramp will be raised in the following section.

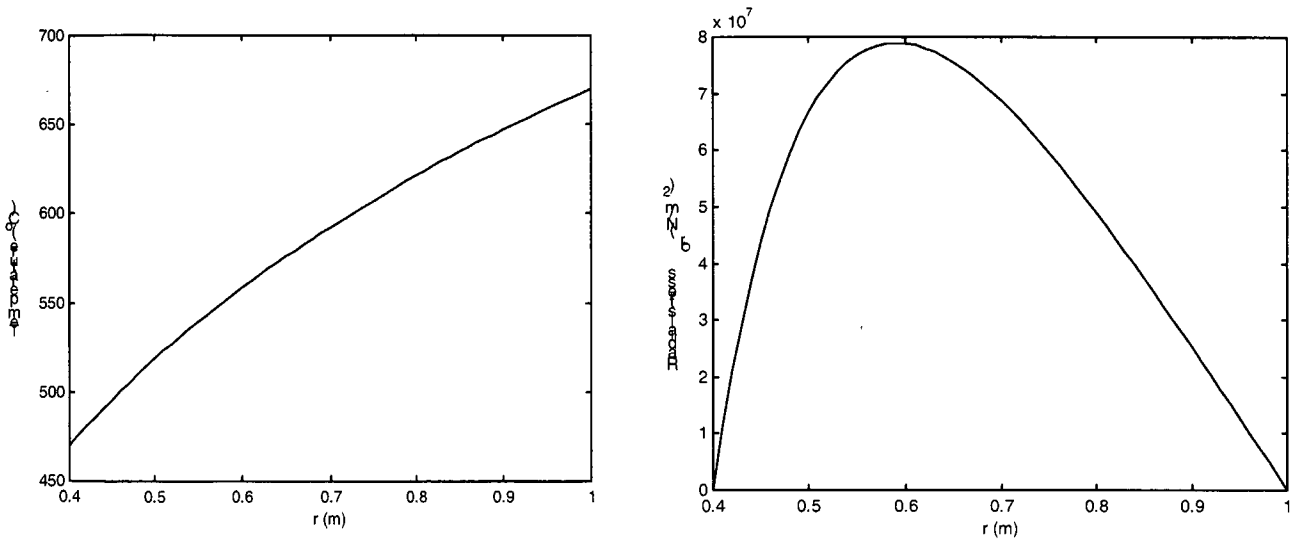

(a) (b)

Figure 5.11: (a) Steady state temperature. (b) A graph of the corresponding radial stress.

5.7 Linear Cooling

At this point, the cooling stage of a temperature ramp will be considered. Assume that cooling takes place according to a linear curve that starts at 670°C and ends at 0°C. The results of the previous section suggest that there may be some merit in initiating cooling on the inner edge several hours before commencing the outer edge temperature decent. Radial stress distributions corresponding to the above-mentioned suggestion will be investigated in this section. The main aim is to compare this with regular cooling, where the temperatures of both inner and outer edges are kept the same during the descent.

Although commencement of cooling for the inner edge will be a few hours sooner than the outer edge, the temperature of both edges will decrease according to the same slope. Recall, once again, that the heat transfer rate is greatly reduced by the absence of a temperature contribution in the z-direction (it takes much longer to reach steady state). Refer to figure 5.12 for an example of a 10 hour time difference between edges.

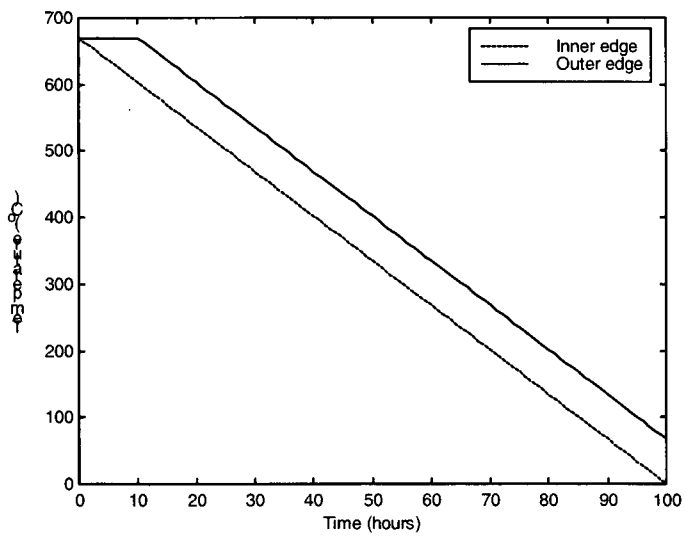

Figure 5.12: A graph of linear cooling in which the outer edge experiences a time lag of 10 hours.

The equation for the cooling ramp in figure 12 is given by

$$T = T_0\left(1+\frac{w}{d}\right)-\frac{T_0}{d}t,$$

where w is the time lag, d is the duration of the cooling ramp and t is the time.

Stress diagrams for a variety of cooling curves are shown in figures 5.13 to 5.20. These curves correspond with a time lag of the outer edge (as shown in table 5.3). This time lag refers to the amount of time that elapses between beginning of cooling, for the inner and outer edges. The stress curves are shown next to the corresponding temperature profiles. All the stress profiles in this section were calculated numerically.

The temperature distributions were obtained by using a one-dimensional finite difference model (similar to section 2.4 of chapter 2, but just one-dimensional). All integration (for equations (5.10)) was performed numerically, using the composite trapezoidal rule (MATLAB has a special function for it). The MATLAB program *D1stressnew.m* for linear cooling can be seen in appendix E.3.

Table 5.3: A table showing the time lag equivalence of each curve.

Curve	Time lag of outer edge (hours)
a	0
b	10
c	20
d	30

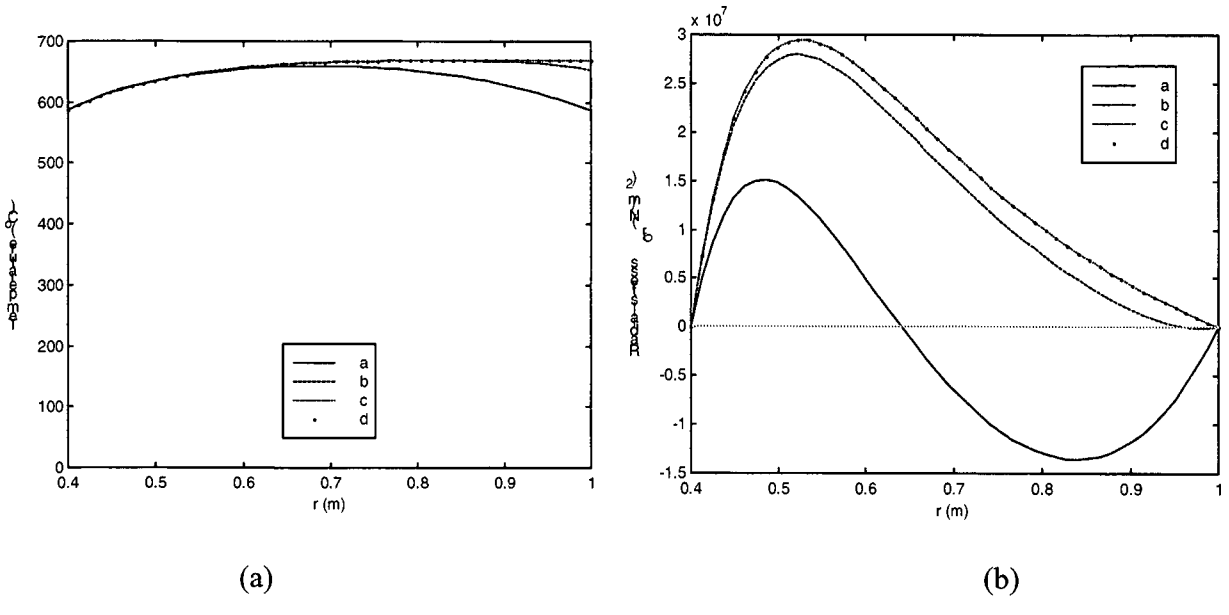

(a) (b)

Figure 5.13: (a) Temperature profiles after 12.5 hours. (b) Radial stress profiles after 12.5 hours. The maximum compressive radial stress for curve a is -1.35×10^7 N/m^2. Curve d experiences a tensile radial stress throughout the cylinder.

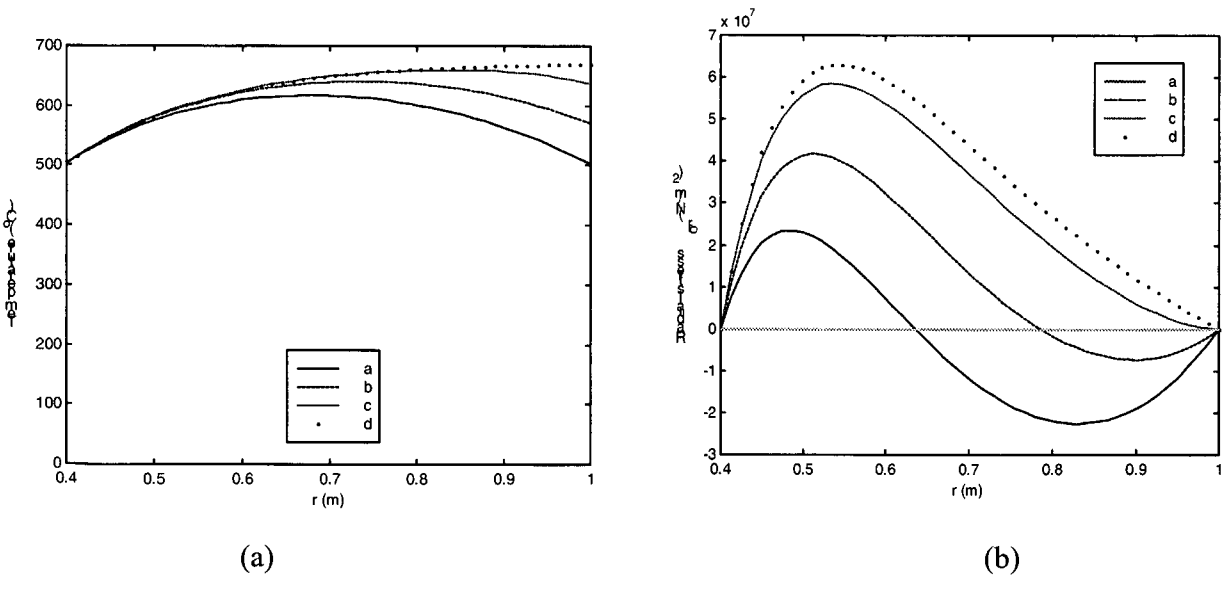

(a) (b)

Figure 5.14: (a) Temperature profiles at 25 hours. (b) Radial stress profiles at 25 hours. The maximum compressive radial stress for curve a is -2.25×10^7 N/m^2. Curve d experiences a tensile radial stress throughout the cylinder.

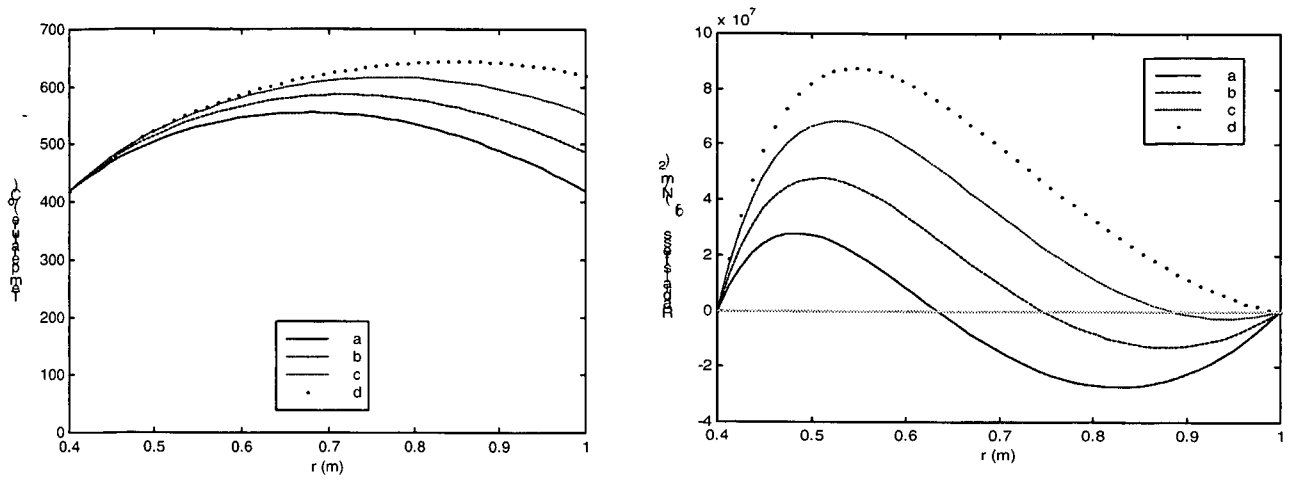

(a) (b)

Figure 5.15: (a) Temperature profiles at 37.5 hours. (b) Radial stress profiles at 37.5 hours. The maximum compressive radial stress for curve a is -2.85×10^7 N/m^2. Curve d experiences a tensile radial stress throughout the cylinder.

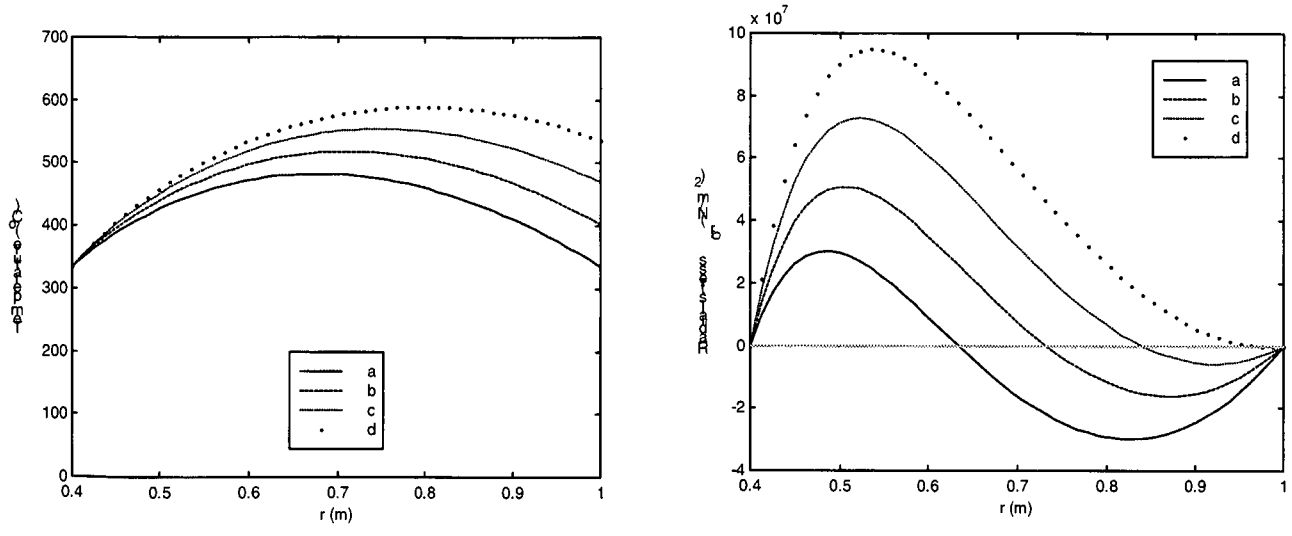

(a) (b)

Figure 5.16: (a) Temperature profiles at 50 hours. (b) Radial stress profiles at 50 hours. The maximum compressive radial stress for curves a and d are -2.98×10^7 N/m^2 and -0.05×10^7 N/m^2, respectively.

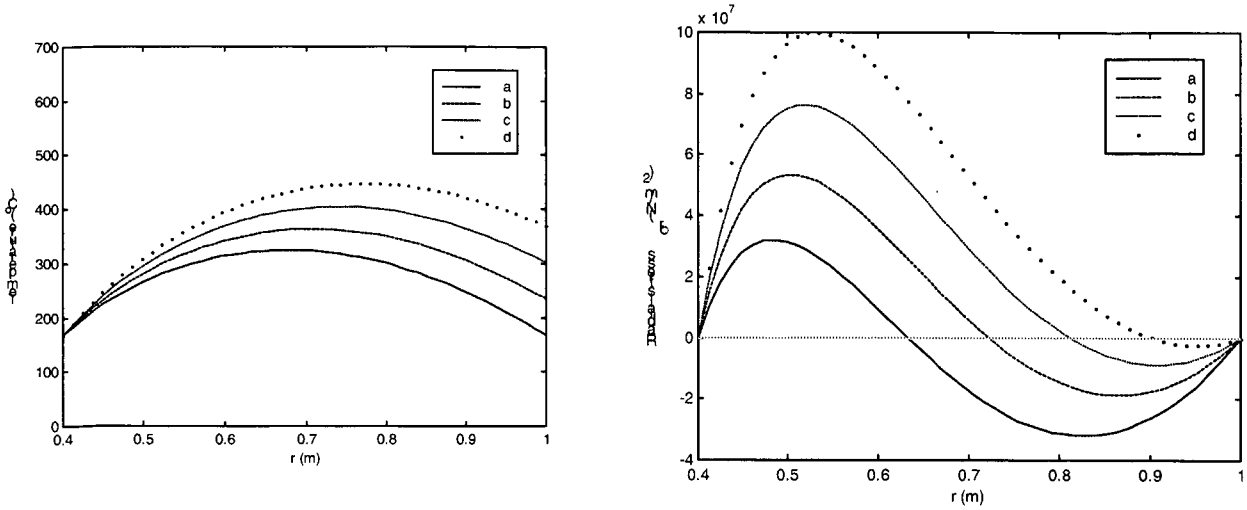

(a) (b)

Figure 5.17: (a) Temperature profiles at 75 hours. (b) Radial stress profiles at 75 hours. The maximum compressive radial stress for curves a and d are -3.105×10^7 N/m2 and –0.235×10^7 N/m^2, respectively.

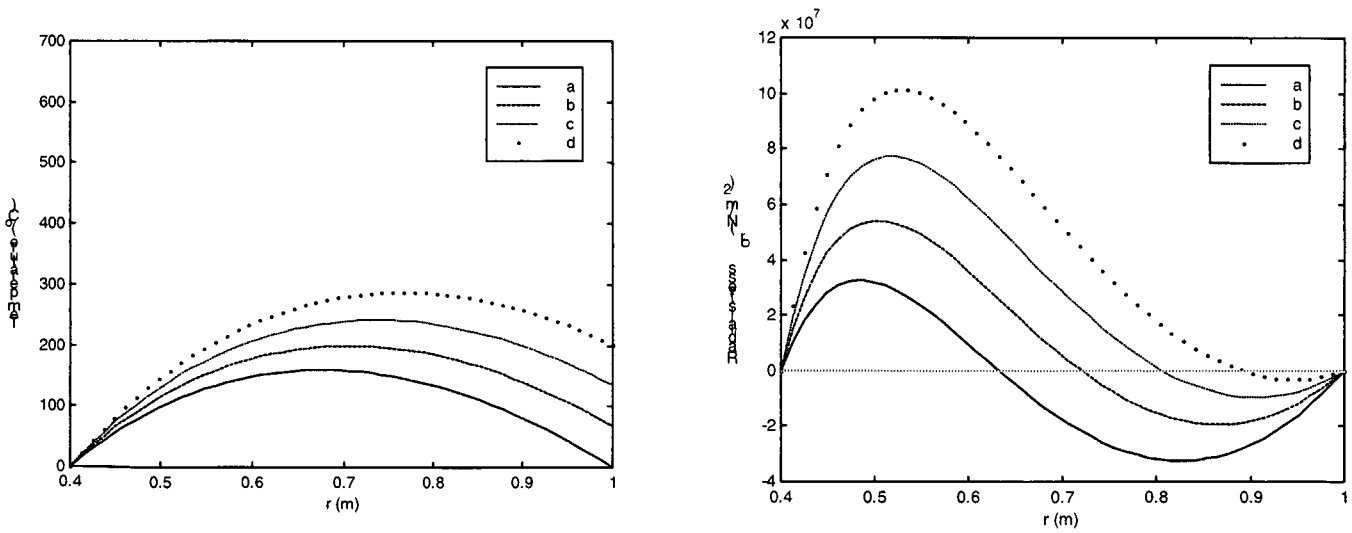

(a) (b)

Figure 5.18: (a) Temperature profiles at 100 hours. (b) Radial stress profiles at 100 hours. The maximum compressive radial stress for curves a and d are -3.2×10^7 N/m^2 and –0.3×10^7 N/m^2, respectively.

Figures 5.13 to 5.18 show a significant difference in compressive stress between curves *a* and *d*. The likelihood of diffusion welds developing between spirals is particularly high in figures 5.13 to 5.16 because of the high temperatures. According to these figures, curve *d* remains tensile throughout the cylinder for figures 5.13 to 5.15 and some marginal compression begins to develop near the outer edge in figure 5.16.

When cooling begins on the inner edge, there is a substantial decrease in radial compressive stress. The conditions for curves *b*, *c*, and particularly *d* reduce the likelihood of strip adhesion. With curve *d*, the coil spirals would tend to separate in most regions of the coil, except for a comparatively small compression (compared with curve a) near the outer edge. This is a satisfactory result, since the radially compressive stress cannot disappear completely during cooling (whenever any interior region of the cylinder has a higher temperature than the outer edge, compressive radial stresses develop).

The linear cooling results also raise the issue practical implementation. A decent treatment of this issue would require a significant amount of additional investigation that falls outside the scope of this thesis.

Chapter 6

Conclusion

In this study, models of temperature and stress were presented. The results of the two-dimensional finite difference model were confirmed by an analytical solution of the same problem. Analysis of the three-dimensional temperature model in chapter 3 showed that, as far as heat transfer is concerned, a cylindrical coil can be approximated by a solid cylinder with a concentric hole.

This is a very important result because it allows one to model a three-dimensional problem two-dimensionally, thus reducing the computation time while maintaining acceptable accuracy. Furthermore, since thermal stress arises from a temperature distribution, it also shows that the thermal stress distribution of a cylindrical coil would be similar to that of a solid cylinder. There would virtually be no θ-dependence of temperature and thermal stress, for a coil of realistic dimensions. It is expected that the greatest θ-dependence would occur at the first and last few spirals of the coil (this would probably cause some movement in those regions). The results of chapter 3 suggest that the bulk of the coil behaves as a solid cylinder.

All the temperature modeling was done for the interior of a coil. In the case where there is more than one coil in a batch-annealing furnace, the boundary conditions of each coil would have to be calculated at each desired time. This can be done by considering radiative heat transfer from the coils and inner cover (figure 1.1), and also by considering

the convective heat transfer from the circulating gas. The finite difference model of chapter 2 can handle the boundary conditions for such a case (if they are given) and provide the resulting temperature distributions for the various coils under investigation. Further study of the position of the cold region, during annealing, could also be performed using the finite difference model.

The long cylinder stress model of chapter 5 provides some useful insight, as far as strip adhesion is concerned, even though it is a one-dimensional model that does not consider the effect of axial heat transfer. The radial compressive stress during the cooling stage of the batch annealing process was identified as an ingredient to strip adhesion.

It is expected that the radial stress profiles of chapter 5 would retain the same shape, but have smaller absolute values, for a two-dimensional model of a solid cylinder. In fact, the radial stress would be largest in the middle of the coil (height-wise) and it would taper off to zero at the top and bottom edges. This is because the temperature distribution becomes more uniform in the radial and axial directions, as the top and bottom edges are approached. Or, in other words, there is very little radial and axial dependence of temperature near the top and bottom edges and no radial and axial dependence at the top and bottom edges. As discussed in section 3.10, thermal stress arises because of non-uniform heating. The axial heat transfer in a solid cylinder model would reduce the radial dependence, thus causing the radial thermal stress to be less that the long cylinder model.

Although not part of the scope of this thesis, it would be possible to adapt the current MATLAB program so that the various operational parameters (coil dimensions, thickness of oil layers, etc.) can be fed to the program, resulting in an (in some sense) optimal temperature profile as output. This optimal temperature profile can be directed to a temperature control unit, with the purpose of producing the required heating and cooling ramps. In terms of software, such a program can be developed in MATLAB and compiled to yield an executable file. If in addition automatic temperature control is required, a temperature control unit with interfacing to the computer via an interfacing board must be obtained.

The results of the linear cooling temperature ramp (section 5.7) are arguably the most important findings of this study. When the cooling of the outer edge lags behind the cooling of the inner edge, by a few hours, the compressive radial stress is significantly reduced. There is still plenty of room for further study in this area, particularly with a two-dimensional model. The results of this study raise the question of whether strip adhesion can be avoided, purely by cooling the coil appropriately. This can only be determined through further study and experimentation.

Appendix A

A.1 Finite Difference Method

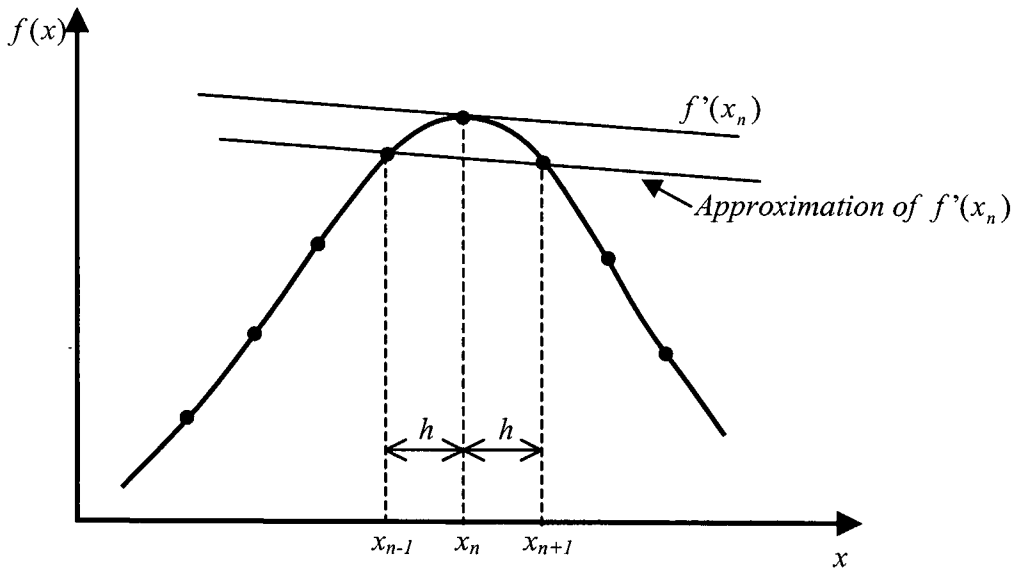

Figure A.1: An illustration of a finite difference approximation.

Consider some function *f(x)*, as shown above in figure A.1. Note that n is used as an index for the x-values. One can estimate the derivative of *f(x)* with respect to x at x_n, $f'(x_n)$, with the slope of the line that joins the points $f(x_{n-1})$ and $f(x_{n+1})$. This approximation can be written as:

$$f'(x_n) = \frac{df(x_n)}{dx} \approx \frac{f(x_{n+1}) - f(x_{n-1})}{x_{n+1} - x_{n-1}} = \frac{f(x_{n+1}) - f(x_{n-1})}{2h} \qquad (2.4)$$

Note that h is the step-length, so $h = x_n - x_{n-1}$.

Equation (2.4) is known as the central difference approximation for the first derivative. The function $f'(x)$ can also be approximated by one-sided differences. There are two types:

(1) The forward difference:

$$f'(x_n) \approx \frac{f(x_{n+1}) - f(x_n)}{h} \quad \text{(A.1)}$$

(2) The backward difference:

$$f'(x_n) \approx \frac{f(x_n) - f(x_{n-1})}{h} \quad \text{(A.2)}$$

To approximate a second derivative $f''(x_n)$, one has to find the two one-sided first derivatives (forward and backward differences) for x_n and divide their difference by the step length h:

$$f''(x_n) \approx \frac{f'(x_{n+1}) - f'(x_{n-1})}{h} = \frac{\frac{(f(x_{n+1}) - f(x_n))}{h} - \frac{(f(x_n) - f(x_{n-1}))}{h}}{h}$$

and thus

$$f''(x_n) \approx \frac{f(x_{n+1}) - 2f(x_n) + f(x_{n-1})}{h^2}. \quad \text{(A.3)}$$

Appendix B

B.1 starter.m

% this program must be executed before running any program in appendices B, C and E.

```
global Tc cpx krx kthx kzx


Tf=100:100:1400; % Fahrenheit temp

  Tc=ones(1,15); % Initialization of variable Tc
  Tc(1,2:15)=(5*(Tf+40)./9)-40; % Celcius temp
  Tc(1)=0;


% Specific heat capacity at constant pressure

cpx=ones(15,1); % Initialization of variable cpx

% Data
cpx(2:15,1)=[.114;
    .116;
    .120;
    .124;
    .128;
    .133;
    .138;
    .144;
    .152;
    .161;
    .174;
    .188;
    .210;
    .236];


cpx(2:15,1)=cpx(2:15,1)*(1054)/((0.4536)*(0.5555));% cp in units of
% J/(kg.C)

% Extrapolation point
cpx(1)=472;

%kr (thermal conductivity in radial direction)
%the formula for kr was obtained from the reference quoted in section
%2.6.

krx=1.15+ .7*(Tf-70)/1200;
krx=krx.*(1054)/((0.3048)*(0.5555)); %Transformation to correct units :
% J/(hr.K.m) or J/(hr.C.m)


%kth (thermal conductivity in tangential direction)

kthx=ones(15,1); % Initialization of variable krth
```

```
% Data

kthx(2:15,1)=[32.4;
   31.4;
   30.2;
   29.4;
   28.2;
   27.2;
   26.2;
   25.1;
   24;
   23;
   22;
   21;
   20.1;
   18.8];
kthx(2:15,1)=kthx(2:15,1)*(1054)/((0.3048)*(0.5555)); %Transformation
%to correct units : J/(hr.K.m) or J/(hr.C.m)

kthx(1)=2.06e+005; % Extrapolation point

%kzx (thermal conductivity in the axial direction)
kzx=kthx;
```

B.2 bessolro.m

```
% This program must be executed before any program in these appendices
% that finds an analytical solution for temperature. This function uses
% an initial guess to calculate the α's and b's.

XX=[];
sig=0.4; % r(inner)/r(outer)
PP=[1.00 -0.38 -4.0]; % guess for b's
X=0; % guess for al's (note X=0+5.236, below)
KK=63;
k=0;
for j=1:KK
k=k+1;
X=fmins('bessolf',[X(1)+5.236 PP(rem(k,3)+1)],[],[],sig);
if bessolf(X,sig)>1e-6, disp('ERROR TOO LARGE'); end
XX=[XX;X];
end

% the XX is a matrix with two columns
% column1 are the al's and column2 are the b's (final result after
%fmins)
```

B.3 function bessolf.m

```
function er=bessolf(X,sig)
al=X(1); B=X(2);
```

```
er=(besselj(0,al*sig)+B*bessely(0,al*sig))^2;
er=er+(besselj(0,al)+B*bessely(0,al))^2;
```

B.5 fine2d.m

```
% finite differences
% Type starter first before running this program

finaltime=3;

% Initializing the temperature matrix HH

Ni=10;
Nj=10;
HH=zeros(Ni,Nj);

roomtemp=0;
for i=2:Ni-1
   for j=2:Nj-1
      H(j,i)=roomtemp;
   end
end

T0=670;
H(:,1)=T0*ones(size(H(:,1)));
H(1,:)=T0*ones(size(H(1,:)));
H(Ni,:)=T0*ones(size(H(1,:)));
H(:,Nj)=T0*ones(size(H(:,1)));
HH=H;
mesh(r,z,H)
axis([0 RO  0 1  0 700])

%pause

rho=7860;

% Dimensions
RI=0.4; RO=1; % Inner and outer radii
LL=1; % coil height
h=(RO-RI)/(Ni-1); k=LL/(Nj-1); % step length in r and z directions
r=RI:h:RO; z=0:k:LL;

tim=0;
Tmax=670;

% Thermal diffusivity
t=25;
krr=kr(t);
kzz=kz(t);
cpp=cp(t);
kapr=krr/(rho*cpp);
kapz=kzz/(rho*cpp);

% Stability conditions
A=( kapr/h^2 + kapz/k^2 );
```

```
B=( kapr/(h*r(1)) );
Tol=8*A/(B^2 + 16*A^2); % tolerance

dt=0.9*Tol % time step
m=[];
n=0;


for tim=0:dt:finaltime;
   n=n+1;
%Outside temperature (boundary conditions)
%T0=ramp1(tim,Tmax);
T0=670;
H(:,1)=T0*ones(size(H(:,1)));
H(1,:)=T0*ones(size(H(1,:)));
H(:,Ni)=T0*ones(size(H(:,1)));
H(Nj,:)=T0*ones(size(H(1,:)));
HH=H;

   for i=2:Ni-1
      for j=2:Nj-1
      HH(j,i)=H(j,i)+dt*( kapr*(1/r(i))*(H(j,i+1)-H(j,i-1))/(2*h) +
      kapr*(H(j,i+1)-2*H(j,i)+H(j,i-1))/(h^2) +
      kapz*(H(j+1,i)-2*H(j,i)+H(j-1,i))/(k^2) );
      end
   end
   H=HH;
end
mesh(r,z,H)
xlabel('r')
ylabel('z')
zlabel('Temperature ({^o}C)')

rotate3d on

axis([0 1 0 1 0 700])
```

B.6 function ramp1.m

```
function T=ramp1(t,T0)
t1=7;
t2=25;
t3=55;
ga1=log(6)/t1;
ga2=log(6)/(t3-t2);
if t<=t1, T=1.2*T0*(1-exp(-ga1*t)); end
if (t>t1) & (t<t2), T=T0; end
if (t>=t2) & (t<t3), T=T0*(-0.2 + 1.2*exp(-ga2*(t-t2))); end
if t>=t3, T=0; end
```

B.7 finramp.m

```
% finite differences
% Type starter first before running this program
```

```
% this program is very similar to B.5

finaltime=50;

Ni=20;
Nj=20;
HH=zeros(Ni,Nj);

roomtemp=0;
for i=2:Ni-1
   for j=2:Nj-1
      H(j,i)=roomtemp;
   end
end
rho=7860;
%Dimensions
RI=0.4; RO=1;
LL=1;
h=(RO-RI)/(Ni-1); k=LL/(Nj-1);
r=RI:h:RO; z=0:k:LL;
tim=0;
Tmax=670;

% thermal diffusivity
t=25;
krr=kr(t);
kzz=kz(t);
cpp=cp(t);
kapr=krr/(rho*cpp);
kapz=kzz/(rho*cpp);

% Stability conditions
A=( kapr/h^2 + kapz/k^2 );
B=( kapr/(h*r(1)) );
Tol=8*A/(B^2 + 16*A^2);
dt=0.9*Tol
m=[];
n=0;
for tim=0:dt:finaltime;
   n=n+1;
%Outside temperature (boundary conditions)
T0=ramp1(tim,Tmax); % temperature ramp
%T0=670;
H(:,1)=T0*ones(size(H(:,1)));
H(1,:)=T0*ones(size(H(1,:)));
H(:,Ni)=T0*ones(size(H(:,1)));
H(Nj,:)=T0*ones(size(H(1,:)));
HH=H;

   for i=2:Ni-1
      for j=2:Nj-1

      HH(j,i)=H(j,i)+dt*( kapr*(1/r(i))*(H(j,i+1)-H(j,i-1))/(2*h) +
      kapr*(H(j,i+1)-2*H(j,i)+H(j,i-1))/(h^2) + kapz*(H(j+1,i)-
      2*H(j,i)+H(j-1,i))/(k^2));
      end
   end
```

```
   H=HH;
% this part collects the data of the cold region at various points in
% the temperature ramp
  if max(H(1,:)) > max(max(H(2:Nj-1,2:Ni-1)))
     m(n)=min(min(H));
  end

  if max(H(1,:)) < max(max(H(2:Nj-1,2:Ni-1)))
     m(n)=max(max(H));
  end


end
m;
l=length(m);
t=0:(50/(l-1)):50;
tempramp %this shows the temperature ramp (see B.7)
hold
plot(t,m)
hold
```

B.8 Tempramp.m

```
T0=0;
tim=0;
dt=0.25;
Tmax=680;
N=200; %(numb of iterations)
TTT=zeros(1,N);
for n=1:N
   tim=tim+dt;
   %Outside temperature
   T0=ramp1(tim,Tmax);
   T0=round(T0);
   TTT(1,n)=T0;
end

x=1:N;
x=dt.*x;
clf
plot(x,TTT)
title('Temperature Ramp')
xlabel('Time (Hours)')
ylabel('Temperature ({^0}C)')
```

B.9 bessol321.m

```
topview=0;  % set to 1 for top view, set to 0 for normal view

finaltime=2;

% Number of grid points
```

```
Ni=21;
Nj=21;

% Thermal diffusivity
c=25;
krr=kr(c);
kzz=kz(c);
cpp=cp(c);
rho=7860;
kar=krr/(rho*cpp);
kaz=kzz/(rho*cpp);

KK=33;  % Number of terms in both Fourier and Bessel series

%bessolro  % for sig=0.4; this routine must be run at least once
AL=XX(:,1);
b=XX(:,2);


% dimensions
h=0.01;
z0=1;

% finding BESSEL coefficients
% ============================

r=sig:h:1;
f=-ones(size(r));
f(1)=0; f(length(f))=0;

A=[];
for k=1:KK
  p=besselj(0,AL(k)*r) + b(k)*bessely(0,AL(k)*r);
  A(k)=sum(f.*p.*r)/sum(p.^2.*r);
end


rr=[r(1)-h r r(length(r))+h];
RR=0;
for k=1:KK
  p=besselj(0,AL(k)*rr) + b(k)*bessely(0,AL(k)*rr);
  RR=RR+A(k)*p;
end

% finding FOURIER coefficients
% =============================


B=[1:KK]*0;
for j=1:2:KK+1
   B(j)=-4/j/pi;
   OM(j)=pi*j;
end


% setting up the grid
% ======================
```

```
hr=(1-sig)/(Ni-1);
hz=z0/(Nj-1);
[r,z]=meshgrid(sig:hr:1,0:hz:z0);

% Calculation of dt
AA=( kar/hr^2 + kaz/hz^2 );
BB=( kar/(hr*sig) );
Tol=8*AA/(BB^2 + 16*AA^2);
dt=0.9*Tol


% solutions at various times
% ==============================
rotate3d on
for t=0:dt:finaltime

RR=0*r; % RR is the R solution
for k=1:KK
    p=besselj(0,AL(k)*r) + b(k)*bessely(0,AL(k)*r);
    RR=RR+A(k)*p.*exp(-kar*AL(k)^2*t);
end

ZZ=0*z; % ZZ is the Z solution
for j=1:KK
   ZZ=ZZ+B(j)*sin(OM(j)*z)*exp(-kaz*OM(j)^2*t);
end


TT=-RR.*ZZ; % Temperature (final solution)

TT=670.*(TT+1); % scaling of TT

   % averaging for correct colormap
   l=size(TT);
   ra1=1:l(1)-1;
   ra2=1:l(2)-1;

TTT(ra1,ra2)=(TT(ra1,ra2)+TT(1+ra1,ra2)+TT(ra1,1+ra2)+TT(1+ra1,1+ra2))/
4;

mesh(r,z,TT)
axis([0 1 0 1 0 670])
xlabel('r');
ylabel('z');
zlabel('Temperature ({^o}C)');
caxis([-1 0]);
if topview==1, view(0,90); end
%pause
end
```

B.10 bessolcomp.m

```
% finite differences
% Type starter first before running this program
%N=10; % Number of iterations
finaltime=2;

% number of grid points
Ni=50;
Nj=50;

Time step
%dt=0.4;
%dt=0.08;
%dt=0.0363636;
%dt=0.02;
%dt=0.0125;
%dt=0.0088888;
%dt=0.005;
dt=0.0030769;

% Initialization of temperature matrix
HH=zeros(Ni,Nj);

roomtemp=0;
for i=2:Ni-1
   for j=2:Nj-1
      H(j,i)=roomtemp;
   end
end
rho=7860;

h=.6/(Ni-1); k=1/(Nj-1);
r=.4:h:1; z=0:k:1;

tim=0;
Tmax=670;

T0=670;
H(:,1)=T0*ones(size(H(:,1)));
H(1,:)=T0*ones(size(H(1,:)));
H(Ni,:)=T0*ones(size(H(1,:)));
H(:,Nj)=T0*ones(size(H(:,1)));
HH=H;
%mesh(H)
%view(0,0)
%axis([0 Ni  0 Nj  0 700])

%pause
t=25;
krr=kr(t);
kzz=kz(t);
cpp=cp(t);
kapr=krr/(rho*cpp);
kapz=kzz/(rho*cpp);
```

```
% Stability condition
A=( kapr/h^2 + kapz/k^2 );
B=( kapr/(h*r(1)) );
Tol=8*A/(B^2 + 16*A^2);

for tim=0:dt:finaltime

   for i=2:Ni-1
      for j=2:Nj-1
          HH(j,i)=H(j,i)+dt*( kapr*(1/r(i))*(H(j,i+1)-H(j,i-1))/(2*h) +
         kapr*(H(j,i+1)-2*H(j,i)+H(j,i-1))/(h^2) + kapz*(H(j+1,i)-
         2*H(j,i)+H(j-1,i))/(k^2) );
      end
   end
   H=HH;
  end
  mesh(H)
  %view(90,0)
   title(['OUTSIDE TEMP= ' num2str(T0)]);
   rotate3d on


topview=0;  % set to 1 for top view, set to 0 for normal view


% Analytical Solution
c=25;
krr=kr(c);
kzz=kz(c);
cpp=cp(c);
rho=7860;
kar=krr/(rho*cpp);
kaz=kzz/(rho*cpp);

KK=33;  % Number of terms in both series

%bessolro  % for sig=0.4; this routine must be run at least once
AL=XX(:,1);
b=XX(:,2);


% dimensions
h=0.01;
z0=1;

% finding BESSEL coefficients
% ============================

r=sig:h:1;
f=-ones(size(r));
f(1)=0; f(length(f))=0;

A=[];
for k=1:KK
  p=besselj(0,AL(k)*r) + b(k)*bessely(0,AL(k)*r);
  A(k)=sum(f.*p.*r)/sum(p.^2.*r);
end
```

```
rr=[r(1)-h r r(length(r))+h];
RR=0;
for k=1:KK
  p=besselj(0,AL(k)*rr) + b(k)*bessely(0,AL(k)*rr);
  RR=RR+A(k)*p;
end

% finding FOURIER coefficients
% ============================


B=[1:KK]*0;
for j=1:2:KK+1
   B(j)=-4/j/pi;
   OM(j)=pi*j;
end


% setting up the grid
% =======================

hr=(1-sig)/(Ni-1);
hz=z0/(Nj-1);
[r,z]=meshgrid(sig:hr:1,0:hz:z0);

% Calculation of dt
AA=( kar/hr^2 + kaz/hz^2 );
BB=( kar/(hr*sig) );
Tol=8*AA/(BB^2 + 16*AA^2);
%dt=0.9*Tol



%colormap(hot)

% solutions at various times
% ==============================
rotate3d on
for t=0:dt:finaltime%N*dt

RR=0*r; % RR is the R solution
for k=1:KK
    p=besselj(0,AL(k)*r) + b(k)*bessely(0,AL(k)*r);
    RR=RR+A(k)*p.*exp(-kar*AL(k)^2*t);
end

ZZ=0*z; % ZZ is the Z solution
for j=1:KK
   ZZ=ZZ+B(j)*sin(OM(j)*z)*exp(-kaz*OM(j)^2*t);
end


TT=-RR.*ZZ; % Temperature (final solution)
% scaling of TT
TT=670.*(TT+1);
```

```
   % averaging for correct colormap
   l=size(TT);
   ra1=1:l(1)-1;
   ra2=1:l(2)-1;

TTT(ra1,ra2)=(TT(ra1,ra2)+TT(1+ra1,ra2)+TT(ra1,1+ra2)+TT(1+ra1,1+ra2))/
4;

%surf(r,z,TT,TTT)
%axis([0 1 0 1 -1 0])
axis([0 1 0 1 0 670])
xlabel('r');
ylabel('z');
zlabel('T');
caxis([-1 0]);
if topview==1, view(0,90); end
%pause
end

%pause

% Temperature difference
d=abs(H-TT);
mesh(r,z,d)
%axis([0 1 0 1 0 670])
xlabel('r')
ylabel('z')
zlabel('Temperature difference (^{o}C)')
title('After 10 iterations')
rotate3d on


maxdiff=max(max(d))
maxper=max(max((d./670)*100))
```

Appendix C

C.1 thermd.m

```
P=[];
show=2;
colormap(hot);

% element numbers
N=10;
%N=5;
Mz=10; % number of elements in z direction
slice=(Mz)/2;

Mth=16; section=16; % number of elements in tangential direction

finaltime=3;

rho=7860;

Tmax=670;

% parameters
RI=0.4;
w=0.1;
LL=1.00;
T0=0;
tim=0;

% setting up the grid
th=0:2*pi/Mth:2*(N+1)*pi;
r=RI + w/2/pi*th;
x=cos(th(1:Mth+1));
y=sin(th(1:Mth+1));
RR=[]; X=[]; Y=[];
for i=0:N
   s=Mth*i+1;
   RR=[RR; r(s:s+Mth)];
   X=[X; x];
   Y=[Y; y];
end
XX=X.*RR;
YY=Y.*RR;
ZZ=0*XX;


% gridsizes
hr=w;
hth=2*pi/Mth;
hz=LL/Mz;

t=25;
krr=kr(t);
ktht=kth(t);
kzz=kz(t);
```

```
cpp=cp(t);

% Stability conditions
t=25;
kapr=kr(t)/(rho*cp(t)); kapz=kz(t)/(rho*cp(t)); kapth=kapz;
A= kapr/hr^2 + kapth/(hth^2*RI^2) + kapz/hz^2;
Tol=8*A/(16*A^2+kapr^2/(hr^2*RI^2));

dt=0.9*Tol; % time step


FZ=[];
fz=[0:hz:LL]';
for i=1:N+1
   FZ=[FZ fz];
end

FR=[];
fr=RI + w*[0:N];
for k=1:Mz+1
   FR=[FR; fr];
end

T0=0;
% set up matrices
T=T0*ones(N+1,Mth,Mz+1);
T(1,:,:)=T0*ones(Mth,Mz+1);
T(N+1,:,:)=T0*ones(Mth,Mz+1);
T(:,:,1)=T0*ones(N+1,Mth);
T(:,:,Mz+1)=T0*ones(N+1,Mth);
TT=T;
SS=(T(1:N,[1:Mth 1],slice) + T(2:N+1,[1:Mth 1],slice))/2;
subplot(121); surf(XX,YY,ZZ,SS); axis('image'); view(0,90);
caxis([0 Tmax/2])

QQ=squeeze((T(1:N,section,:) + T(2:N+1,section,:))/2);
QQ=(QQ(:,1:Mz)+QQ(:,2:Mz+1))/2;
subplot(122); surf(FR,FZ,0*FZ,QQ'); axis('image'); view(0,90);
caxis([0 Tmax/2]);
%pause
clf
n=0;

for tim=0:dt:finaltime;
   n=n+1;
   %Outside temperature
   %T0=ramp1(tim,Tmax); % this part is used when monitoring the cold
   %region according  to a temperature ramp
   T0=Tmax;
   T(1,:,:)=T0*ones(Mth,Mz+1);
   T(N+1,:,:)=T0*ones(Mth,Mz+1);
   T(:,:,1)=T0*ones(N+1,Mth);
   T(:,:,Mz+1)=T0*ones(N+1,Mth);
   TT=T;
   f=squeeze(T(:,1,:));
   f=f';
   z=0:1/10:1;rr=RI:(1.5-RI)/10:1.5;
```

```
   mesh(rr,z,f)
   axis([0 1.5 0 1 0 700])
   xlabel('r')
   zlabel('Temperature ({^o}C)')
   ylabel('z')
   %pause

for i=2:N
   % theta first edge
   j=1;
   R=r(Mth*(i-1)+j-1);
   for k=2:Mz
      TT(i,j,k)=T(i,j,k)  + dt*(krr/(rho*cpp))*(T(i+1,j,k)-
      2*T(i,j,k)+T(i-1,j,k))/hr^2 ;
      TT(i,j,k)=TT(i,j,k) + dt*(krr/(rho*cpp))*(T(i+1,j,k)-T(i-
      1,j,k))/2/hr/R;
      TT(i,j,k)=TT(i,j,k) + dt*(ktht/(rho*cpp))*(T(i,j+1,k)-
      2*T(i,j,k)+T(i-1,Mth,k))/hth/R^2;
      TT(i,j,k)=TT(i,j,k) + dt*(kzz/(rho*cpp))*(T(i,j,k+1)-
      2*T(i,j,k)+T(i,j,k-1))/hz^2;
   End

    % interior
   for j=2:Mth-1
      R=r(Mth*(i-1)+j-1);
      for k=2:Mz
         TT(i,j,k)=T(i,j,k)  + dt*(krr/(rho*cpp))*(T(i+1,j,k)-
         2*T(i,j,k)+T(i-1,j,k))/hr^2 ;
         TT(i,j,k)=TT(i,j,k) + dt*(krr/(rho*cpp))*(T(i+1,j,k)-T(i-
         1,j,k))/2/hr/R;
         TT(i,j,k)=TT(i,j,k) + dt*(ktht/(rho*cpp))*(T(i,j+1,k)-
         2*T(i,j,k)+T(i,j-1,k))/hth/R^2;
         TT(i,j,k)=TT(i,j,k) + dt*(kzz/(rho*cpp))*(T(i,j,k+1)-
         2*T(i,j,k)+T(i,j,k-1))/hz^2;
      end
    end

   % theta last edge
   j=Mth;
   R=r(Mth*(i-1)+j-1);
   for k=2:Mz
      TT(i,j,k)=T(i,j,k)  + dt*(krr/(rho*cpp))*(T(i+1,j,k)-
      2*T(i,j,k)+T(i-1,j,k))/hr^2 ;
      TT(i,j,k)=TT(i,j,k) + dt*(krr/(rho*cpp))*(T(i+1,j,k)-T(i-
      1,j,k))/2/hr/R;
      TT(i,j,k)=TT(i,j,k) + dt*(ktht/(rho*cpp))*(T(i+1,1,k)-
      2*T(i,j,k)+T(i,j-1,k))/hth/R^2;
      TT(i,j,k)=TT(i,j,k) + dt*(kzz/(rho*cpp))*(T(i,j,k+1)-
      2*T(i,j,k)+T(i,j,k-1))/hz^2;
    end
 end

if rem(n,show)==0,
SS=(T(1:N,[1:Mth 1],slice) + T(2:N+1,[1:Mth 1],slice))/2;
subplot(121); surf(XX,YY,ZZ,SS); axis('image'); view(0,90);
caxis([0 Tmax])
title(['Time= ' num2str(tim),' hours'])
```

```
QQ=squeeze((T(1:N,section,:) + T(2:N+1,section,:))/2);
QQ=(QQ(:,1:Mz)+QQ(:,2:Mz+1))/2;
subplot(122); surf(FR,FZ,0*FZ,QQ'); axis('image'); view(0,90);
caxis([0 Tmax]);
colorbar
title(['Outside temperature= ' num2str(T0),'{^o}C']);
%pause
P=[P QQ(:,slice)];
end
hours=n*dt;
T=TT;

% this part collects the data for the cold region during a temperature
% ramp

if max(max(T(1,:,:)))> max(max(max(T(2:N,2:Mth,2:Mz))))
   m(n)=min(min(min(T(2:N,2:Mth,2:Mz))));
end

if max(max(T(1,:,:)))< max(max(max(T(2:N,2:Mth,2:Mz))))
   m(n)=max(max(max(T(2:N,2:Mth,2:Mz))));
end


end

clf
f=squeeze(T(:,1,:));
f=f';
z=0:1/10:1;rr=RI:(1.5-RI)/10:1.5;
mesh(rr,z,f)
axis([0 1.5 0 1 0 700])
xlabel('r')
zlabel('Temperature ({^o}C)')
ylabel('z')
title('Time = 3 hours')
```

Appendix D

D.1 Partial Derivatives

The partial derivative of a variable, with respect to x_k, will be denoted by adding a subscript comma and a subscript k to the variable. For an example:

$$\frac{\partial \sigma_{ij}}{\partial x_k} = \sigma_{ij,k}. \quad \text{(D.1)}$$

For the three-dimensional case, all the indices i, j and k run from 1 to 3. There are therefore nine possible components for σ_{ij}, of which six are independent (by virtue of (4.2)), and there are three possible values for x_k (i.e. x_1, x_2, x_3). This means that (D.1) gives 27 equations, with only 18 independent ones.

The summation convention, which is often used with tensor calculations, will be used. According to this convention, summation is implied whenever an index appears twice on any side of an equation. Some examples follow below:

$$\sigma_{ij,i} = \sum_i \frac{\partial \sigma_{ij}}{\partial x_i} \quad \text{(D.2)}$$

and

$$\sigma_{ij,j} = \frac{\partial}{\partial x_j}\left(\sum_i \sigma_{ii}\right) \quad \text{(D.3)}$$

Higher order derivatives can also be expressed in this manner. For instance,

$$\frac{\partial^2 \sigma_{ij}}{\partial x_k \partial x_m} = \sigma_{ij,km}\ , \quad \text{(D.4)}$$

$$\sigma_{ij,kk} = \sum_k \frac{\partial^2}{\partial x_k^{\,2}} (\sigma_{ij}) \tag{D.5}$$

and

$$\sigma_{ii,km} = \frac{\partial^2}{\partial x_k \partial x_m} \left(\sum_i \sigma_{ii} \right). \tag{D.6}$$

D.2 The Kronecker delta

The Kronecker δ_{ik} delta is defined as follows:

$$\delta_{ik} = \begin{cases} 1, & if\ i = k \\ \\ 0, & if\ i \neq k \end{cases} \tag{D.7}$$

therefore

$$\delta_{ik} = \begin{bmatrix} 1 & 0 & 0 \\ 0 & 1 & 0 \\ 0 & 0 & 1 \end{bmatrix}. \tag{D.8}$$

Appendix E

E.1 function rampcool.m

```
function T=rampcool(t,T0,wait,duration)
T=T0*(duration+wait-t)/duration;
T=min(T,T0);
T=max(T,0);
```

E.2 astress.m

```
% Thermal diffusivity
c=25;
krr=kr(c);
kzz=kz(c);
cpp=cp(c);
rho=7860;
kar=krr/(rho*cpp);
rotate3d on

Ni=100; Nj=Ni; % number of grid points

N=50;
KK=63;  % Number of terms in both series

%bessolro  % for sig=0.4; this routine must be run at least once
AL=XX(:,1);
b=XX(:,2);

al=12e-6; E=20e+10; nu=(1/3);

% dimensions
h=0.01;
z0=1;

% finding BESSEL coefficients
% ============================

r=sig:h:1;
f=-ones(size(r));
f(1)=0; f(length(f))=0;

A=[];
for k=1:KK
  p=besselj(0,AL(k)*r) + b(k)*bessely(0,AL(k)*r);
  A(k)=sum(f.*p.*r)/sum(p.^2.*r);
end


rr=[r(1)-h r r(length(r))+h];
RR=0;
for k=1:KK
  p=besselj(0,AL(k)*rr) + b(k)*bessely(0,AL(k)*rr);
```

```
  RR=RR+A(k)*p;
end


% setting up the grid
% ======================

hr=(1-sig)/(Ni-1);
hz=z0/(Nj-1);
r=sig:hr:1;


v=0;
j=0;
SR=[];
TTT=[];
%for t=0:0.2:2
for t=0:2:120
   v=v+1;

RR=0*r; % RR is the R solution
for k=1:KK
    p=besselj(0,AL(k)*r) + b(k)*bessely(0,AL(k)*r);
    RR=RR+670*A(k)*p.*exp(-kar*AL(k)^2*t)+670*(1/KK);
end

TT=RR;
% SR
%====
sr=0*r;
sth=sr;
sz=sr;
D=al*E./((1-nu)*r.^2);
for k=1:KK
      pp=((besselj(1,AL(k))+b(k)*bessely(1,AL(k))) -
         sig*(besselj(1,AL(k)*sig)+b(k)*bessely(1,AL(k)*sig)));
      pd=((besselj(1,AL(k).*r)+b(k)*bessely(1,AL(k).*r)).*r-
         sig*(besselj(1,AL(k)*sig)+b(k)*bessely(1,AL(k)*sig)));
      p=(besselj(0,AL(k)*r) + b(k)*bessely(0,AL(k)*r));

      sr=sr+(A(k)/AL(k))*( ((r.^2-sig^2)./(1-sig^2))*pp - pd )*exp(-
         AL(k)^2*kar*t);
      sth=sth+(A(k)/AL(k))*( ((r.^2+sig^2)./(1-sig^2))*pp + pd -
         AL(k)*p.*r.^2 )*exp(-AL(k)^2*kar*t);
      sz=sz+(A(k)/AL(k))*( (2/(1-sig^2))*pp - AL(k)*p )*exp(-
         AL(k)^2*kar*t);
end

sr=670*sr.*D;
sth=670*sth.*D;
sz=670*(al*E/(1-nu))*sz;

SR(v,:)=sr;
STH(v,:)=sth;
SZ(v,:)=sz;
TTT(v,:)=TT;
```

```
%SR
%plot(r,sr)
xlabel('r (m)')
ylabel('{\sigma_{rr}} (N/m^2)')

%plot(r,TT)
%pause
end

save TTT
save SR
save SZ
save STH
```

E.3 steadystate.m

```
al=12e-6;
E=20e+10;
nu=1/3;

a=0.4;
b=1;
r=a:.01:b;
Ti=470;To=670;


% Temperature
TT=((Ti-To)/log(a/b))*log(r) + ((To*log(a)-Ti*log(b))/log(a/b));

plot(r,TT,'b')
xlabel('r (m)')
ylabel('Temperature (^oC)')
%title('T_i = 670^oC and T_0 = 470^oC')
pause

A=(Ti-To)/log(a/b); B=(To*log(a)-Ti*log(b))/log(a/b);
psi=A*( (0.5*b^2*log(b)-0.25*b^2)-(0.5*a^2*log(a)-
    0.25*a^2))+0.5*B*(b^2-a^2);
phi=A*( (0.5*r.^2.*log(r)-0.25*r.^2)-(0.5*a^2*log(a)-
    0.25*a^2))+0.5*B*(r.^2-a^2);
sr=(al*E./(r.^2*(1-nu))).*( psi*((r.^2-a^2)./(b^2-a^2)) - phi );

plot(r,sr)
xlabel('r (m)')
ylabel('Radial stress {\sigma}_{rr} (N/m^2)')
%title('T_i = 670^oC and T_0 = 470^oC')
```

E.4 D1stressnew.m

```
% finite differences
% Type starter first before running this program

finaltime=100;

Ni=50;
Nj=Ni;
HH=670*ones(1,Ni);

al=12e-6; E=20e+10; nu=(1/3);
sig=0.4;
rho=7860;

hr=(1-sig)/(Ni-1); k=1/(Nj-1);
r=sig:hr:1; z=0:k:1;

tim=0;
Tmax=670;

H=HH;

t=25;
krr=kr(t);
kzz=kz(t);
cpp=cp(t);
kapr=krr/(rho*cpp);
kapz=kzz/(rho*cpp);

% Stability conditions
A=(kapr/hr^2);
B=( kapr/(hr*r(1)) );
Tol=8*A/(B^2 + 16*A^2);
dt=0.9*Tol;

%Tlin2=[];
%SRlin2=[];
Tlin=[];
SRlin=[];

v=0;
vv=0;

clf;
CPUTIME=[];
plot(r,H)
axis([0.4 1 0 680])
hold on
earlier=now;
for tim=0:dt:finaltime
   %calculation of computation time
  if floor(2*(tim-dt))-floor(2*tim)<0,
  CPUTIME=[CPUTIME; (now-earlier)*3600*24];
  plot(r,H)
  title(num2str(tim));
```

```
  %pause
  end
 v=v+1;
%Ti=rampcool(tim,Tmax,0,100);
%To=rampcool(tim,Tmax,10,100);

To=rampcool(tim,Tmax,0,100);
%H(1)=Ti; H(Ni)=To;
H(1)=To; H(Ni)=To;

HH=H;
dtkap=dt*kapr/hr;
   for i=2:Ni-1
      for j=2:Nj-1
         HH(i)=H(i)+dtkap*((H(i+1)-H(i-1))/(2*r(i)) + (H(i+1)-
         2*H(i)+H(i-1))/hr);
      end
   end
   H=HH;


% this part collects a select amount of temperature and radial stress
% data
if rem(v,178)==0
    vv=vv+1;
    integralT=hr*trapz(H.*r);
    integralTr=hr*cumtrapz(H.*r);
    srr=(al*E./(r.^2*(1-nu))).*( ((r.^2-sig^2)./(1-sig^2))*integralT -
    integralTr );

    %Tlin2(vv,:)=H;
    %SRlin2(vv,:)=srr;
    Tlin(vv,:)=H;
    SRlin(vv,:)=srr;

end

%pause
end
save Tlin
save SRlin
%save Tlin2
%save SRlin2
```

References

[1] A.R. Perrin, B.F. Johnston, *Iron and Steel Engineer*, June (1983) 39.

[2] A.A Lisogor, V.I. Mitkalinnyi, *Heat Technology*, December (1970) 1132.

[3] T.R.S. Rao, G.J. Barth, J.R. Miller, *Iron and Steel Engineer*, September (1983) 22.

[4] A.J. Ravito, *Iron and Steel Engineer*, July (1989) 35.

[5] V. Leroy, D. Bouquegneau, *Industry News*, May (1999).

[6] P. Zylla, *United States Patent-Patent Number: 5 344 509*, September 6, (1994).

[7] R.K. Nagle, E.B. Saff, *Fundamentals of Differential Equations*, Third Edition, Addison-Wesley, 1993.

[8] W.F. Ames, *Numerical Methods for Partial Differential Equations*, Nelson, 1969.

[9] M.R.SPIEGEL, *Schaum's Outline Series – Mathematical Handbook*, McGraw-Hill Inc. 1968.

[10] W.E. Boyce, R.C. DiPrima, *Elementary Differential Equations and Boundary Value Problems*, Sixth Edition, John Wiley and Sons, 1997.

[11] M.A. Pinsky, *Partial Differential Equations and Boundary-Value Problems with Applications*, McGraw-Hill Inc., 1991.

[12] Mase, G. E., *Schaum's Outline Series - Theory and Problems of Continuum Mechanics*, McGraw-Hill Inc., 1970.

[13] S. Timoshenko, *Theory of Elasticity*, First Edition, Eighth Impression, McGraw-Hill Inc., 1934.

[14] A.S. Saada, *Elasticity Theory and Applications*, Pergamon Press Inc., 1974.

[15] H. Ford, J.M. Alexander, *Advanced Mechanics of Materials*, Second Edition, John Wiley and Sons Inc.,1977.